Title
Compton clock and recoil frequency measurements using a large momentum transfer atom interferometer

Author
Kuan, Pei-Chen

Publication Date
2013

Peer reviewed|Thesis/dissertation

Compton clock and recoil frequency measurements using a large momentum transfer atom interferometer

by

Pei-Chen Kuan

A dissertation submitted in partial satisfaction of the
requirements for the degree of
Doctor of Philosophy

in

Physics

in the

Graduate Division

of the

University of California, Berkeley

Committee in charge:

Professor Holger Müller, Chair
Professor Dmitry Budker
Professor Naomi Ginsberg

Fall 2013

Compton clock and recoil frequency measurements using a large momentum transfer atom interferometer

Abstract

Compton clock and recoil frequency measurements using a large momentum transfer atom interferometer

by

Pei-Chen Kuan

Doctor of Philosophy in Physics

University of California, Berkeley

Professor Holger Müller, Chair

Light-pulse atom interferometers have been used as quantum inertial sensors and for precision tests of fundamental laws of physics. For higher contrast, we apply conjugate Ramsey-Bordé interferometers to cancel out vibrational noise and top mirror tilting to compensate the Coriolis force. For higher sensitivity, we implement Bragg diffraction and Bloch oscillations for large momentum transfer to increase the enclosed area of our atom interferometer. We also utilize Raman sideband cooling in our experimental setup, which increases the overall signal about twentyfold, and increases the contrast by suppressing the thermal expansion of the atom cloud.

By combining measurements of recoil frequency and a frequency comb, we present the first clock referenced to the mass of a single particle. The rest mass of a particle defines its Compton frequency, $mc^2/\hbar$ through relativity and quantum mechanics, and thereby sets a fundamental timescale. Our clock stabilizes a 10 MHz radio frequency signal to a certain fraction of the cesium Compton frequency. Future work could result in an elementary particle (electron) or even antimatter (antihydrogen) clock, opening up new ways to test CPT symmetry and the equivalence principle.

We also present our progress towards a new determination of the fine structure constant. The fine structure constant value obtained by our cesium Compton clock measurement is about three times better compared with the earlier cesium recoil frequency result. After combining Bragg diffraction and Bloch oscillations, we achieved 0.33 ppb sensitivity (0.66 ppb uncertainty of the recoil frequency measurement) in 6 hours, which is about two times better than the previous best recoil frequency measurement. The leading systematic effect is also reduced by a factor of 2.75.

To my parents

Acknowledgments

First, I would like to thank my advisor Holger Müller, for his guidance during my graduate career. His encouragement helped me significantly and his physical intuition and profound knowledge of electronics have resulted in the project steadily progressing. I would also like to thank professor Dmitry Budker and professor Naomi Ginsberg for their patience and comments during the preparation of this dissertation.

My life as a graduate student researcher in Berkeley has benefited from my research colleagues. It is my great pleasure to have a chance to work with Shau-Yu Lan. Without his great patience and assiduity we could not overcome issues which happened in the experiment.

I would like to thank Michael Hohensee for his thoughtful advice on the mechanisms beyond the experimental data, Paul Hamilton for his suggestions about computer programming, and Justin M. Brown for his hearty help.

I would also like to thank Brian Estey. His energetic attitude towards solving problems encourages me a lot. I would also like to thank Chenghui Yu, who is highly responsible.

I would also like to thank Philipp Haslinger for his contribution to the Coriolis force compensation, Markus Krutzik for his hard work in the implementation of Raman sideband cooling, Damon English and Pauli Kehayias for their assistance with the frequency comb.

I would also appreciate the helpful discussions with Michelle Xu, Geena Kim, and Erin Sohr.

Finally, I would like to thank my parents and other family members. It is your support that made me get through the hard years.

Contents

List of Tables

List of Figures

Chapter 1

Introduction

1.1 Introduction to atom interferometry

1.1.1 The analog between optical interferometry and matter wave interferometry

Compared with atom interferometers, people may be more familiar with optical interferometers, as shown in figure 1.1. In optical interferometers, light is divided into different paths by the help of beam splitters, and change directions later by being reflected by mirrors. When light passing through different paths meet at the final beam splitter, the interference will transform accumulated phases into the modulation of intensity. After reading out the signal, the phase difference can be retrieved and related information can be obtained.

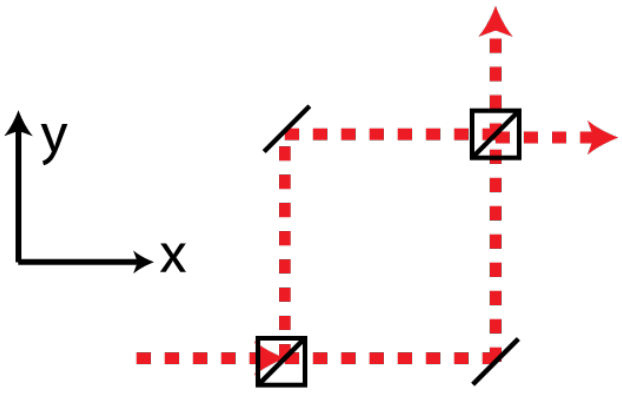

Figure 1.1: Optical interferometer. Red dashed lines represent light. Light passes through the first beam splitter, reflected by individual mirrors, and recombined together at the end by the second beam splitter.

For matter wave interferometers, as demonstrated in figure 1.2, the roles played by light

and matter are exchanged. In optical interferometers, light carries the phases being measured, and beam splitters and mirrors change the paths of light. In atom interferometers, however, matter waves carry the phase. Light directs matter waves into their new paths by atom light interactions. In the optical interferometer, momentum of the light changes when it is absorbed and re-emitted by materials. Similarly, in the atom interferometer atoms will have different momentum by absorbing momentum carried by photons. By changing the conditions of the momentum transfer, atoms can have between 0 and 100 % probability to change into a new momentum state. For the 100 % case, this corresponds to the mirror case in optical interferometry. For the 50 % case, atoms are in a superposition of both states which corresponds to the beam splitter. We use the Bloch sphere concept [1] and call the 100 % case as π pulse and the 50 % case as $\pi/2$ pulse.

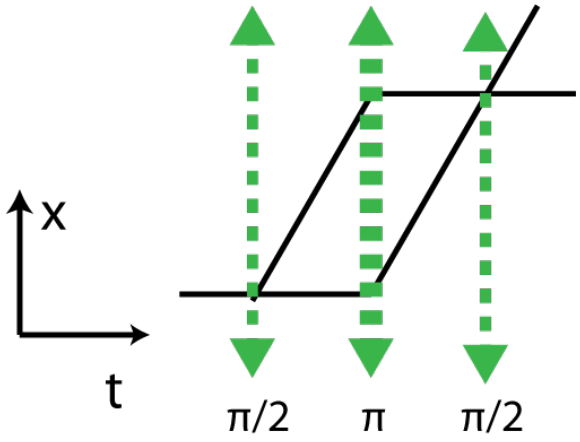

Figure 1.2: Atom interferometer. The horizontal coordinate is time, and the vertical shows different height. Matter waves are shown in black lines, and laser pulses are shown in green dotted lines.

1.1.2 Applications of atom interferometry

In optical interferometry, the phase of photons in vacuum is $kx - \omega t$, where k is the wave vector, x is the space position, ω is the angular frequency, and t is the time coordinate. Therefore preliminary applications of optical interferometry can be measurements of the length difference between paths or the frequency components of laser beams with known path lengths. In atom interferometry, the free evolution phases of matter waves will be

$$\frac{1}{\hbar}\int_{\text{classical}}\left(\frac{m\dot{x}^2}{2} - V(x)\right)dt, \tag{1.1}$$

where $\hbar$ is the reduced Planck constant, $V(x)$ is the potential related to position x, m is the mass, and the dot indicates the time derivative .

The potential energy part naturally relates to the gravitational potential, because of the atom mass. Therefore, atom interferometers can measure local gravity by the change of potential-related phase. From the measurement of local gravity [2], or local acceleration, it is possible to build an inertial sensor for navigation. In addition, it can be used to test general relativity [3], measure the Newton's constant G [4], and verify the gravitational Aharonov-Bohm effect [5]. Instead of the gravitational potential, we can add a local voltage to generate an electrical potential; therefore atom interferometers can also be used to verify the charge neutrality of atoms [6].

The kinetic part of the phase relates to the inertial masses of atoms. The momentum change of atoms can come from photon absorptions and photon emissions. The photon momentum is defined as $\hbar k$. The kinetic energy difference between initial and final states after absorbing or emitting one photon defines the recoil frequency, which is the energy difference divided by $\hbar$,

$$\omega_{\mathrm{r}} = \frac{\hbar k^2}{2m}, \tag{1.2}$$

where m is the inertial mass. We can obtain information about $\hbar/m$ from the recoil frequency value (which in ^{133}Cs, with 852 nm laser wavelength is about 2066 Hz) combined with the laser frequency. From $\hbar/m$ we can measure the fine structure constant, which will be discussed later in section 1.2.3. Some of other applications of atom interferometers are measurements of gravitational wave [7] and Sagnac effect [8].

1.1.3 Some atom interferometry configurations

Different combinations of beam splitters will result in different atom interferometers, including Mach-Zehnder atom interferometer [2] (figure 1.3a), Ramsey-Bordé interferometers [9] (figure 1.3b), double-loop atom interferometers [10], contrast atom interferometer [11], and so on [5, 12]. Different atom interferometer configurations are sensitive to different physical properties, and people can specify corresponded atom interferometers to measure the desired quantity. Mach-Zehnder atom interferometer can be used to measure local gravity [2], and Ramsey-Bordé interferometer can be used to measure $\hbar/m$ [9].

1.2 The fine structure constant

1.2.1 What is the fine structure constant

The fine structure constant α characterizes the strength of the electromagnetic interaction. It is related to other physical quantity as

$$\alpha = \frac{1}{4\pi\varepsilon_0}\frac{e^2}{\hbar c}, \tag{1.3}$$

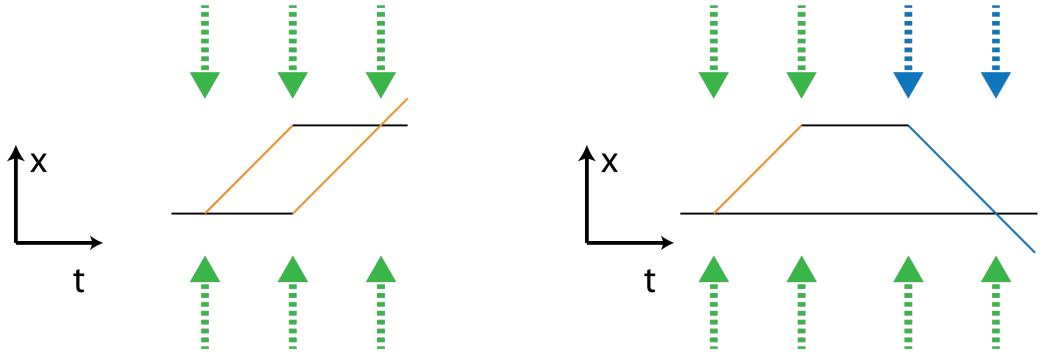

(a) Mach-Zehnder scheme. (b) Ramsey-Bordé scheme

Figure 1.3: Different atom interferometer schemes. The vertical axis indicates the height, and the horizontal axis indicates the time. Dashed lines show the laser light and solid lines represent the matter waves' trajectories. Different color in dashed lines represents different frequency, and different color in solid line indicates atoms with different velocity.

Descripton	$(\alpha^{-1} - 137.03) \times 10^3$	Uncertainty (ppb)
Electron $g_e - 2$	5.999173(35) [14, 15]	0.25
Photon Recoil $\hbar/m_{\mathrm{Rb}}$	5.999045 (90) [16]	0.66
Photon Recoil $\hbar/m_{\mathrm{Cs}}$	6.0000 (11) [9]	7.7
Quantum Hall effect R_K	6.0037 (33) [17]	24
AC Josephson effect $\Gamma'_{p-90}(lo)$	5.9879 (51) [18]	37
Muonium Hyperfine structure	6.0017(80) [19]	58
CODATA 2010 adjusted value	5.999074(44)	0.32

Table 1.1: Precision measurements of the fine structure constant.

where e here is the electrical charge, ε_0 is the dielectric constant and c is the speed of light. The value, according to CODATA 2010, is 1/137.035999074(44) [13].

1.2.2 Measurements of the fine structure constant

There are many ways of measuring the fine structure constant, including the quantum Hall effect, helium fine structure splitting, recoil frequency, and $g-2$ measurement [13]. The measured values and uncertainties are shown in table 1.1, and the relative scale is shown in figure 1.4.

The most accurate value of the fine structure constant comes from the measurement of $g-2$ with 0.25 ppb uncertainty [14, 15]. The calculation of Feynman diagrams limits its accuracy. The relation between $g-2$ and α is

$$\frac{g}{2} = 1 + C_2\left(\frac{\alpha}{\pi}\right) + C_4\left(\frac{\alpha}{\pi}\right)^2 + C_6\left(\frac{\alpha}{\pi}\right)^3 + C_8\left(\frac{\alpha}{\pi}\right)^4 + C_{10}\left(\frac{\alpha}{\pi}\right)^5 + \cdots + a_{\mu,\tau} + a_{\mathrm{had}} + a_{\mathrm{weak}}, \quad (1.4)$$

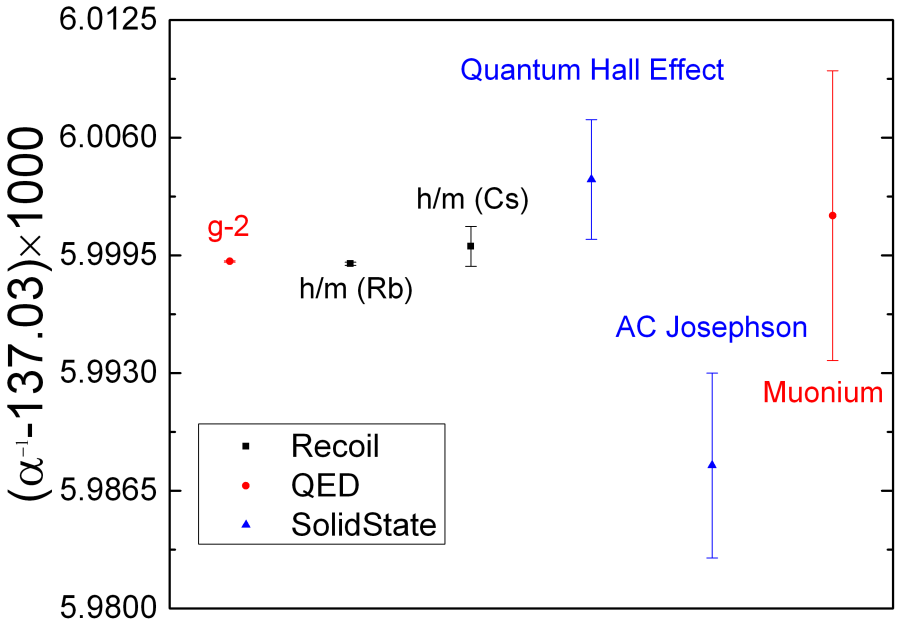

Figure 1.4: Measurements of the fine structure constant. The results are shown in three different groups, corresponding to different methods.

where C_2 is the second order correction and C_4 is the fourth order correction, and so on. The correction from hardronic interaction and electroweak interaction are a_{had} and a_{weak}, respectively. The term $a_{\mu,\tau}$ corresponds to the vacuum polarization loop and relates to m_e/m_μ, and m_e/m_μ, where m_e stands for the electron mass, m_μ stands for the muon mass, and m_τ stands for the tau mass. The number of Feynman diagrams for the C_2 correction is 1, 7 for the C_4 correction, 72 for C_6, 891 for C_8, and 12672 for C_{10} [15]. Analytical calculations only work to the third order correction, and the fourth and fifth order corrections are calculated by computers. The values are shown in figure 1.5, we can see the uncertainty is much larger than the $g-2$ measurement itself, which is 0.28 ppt [14].

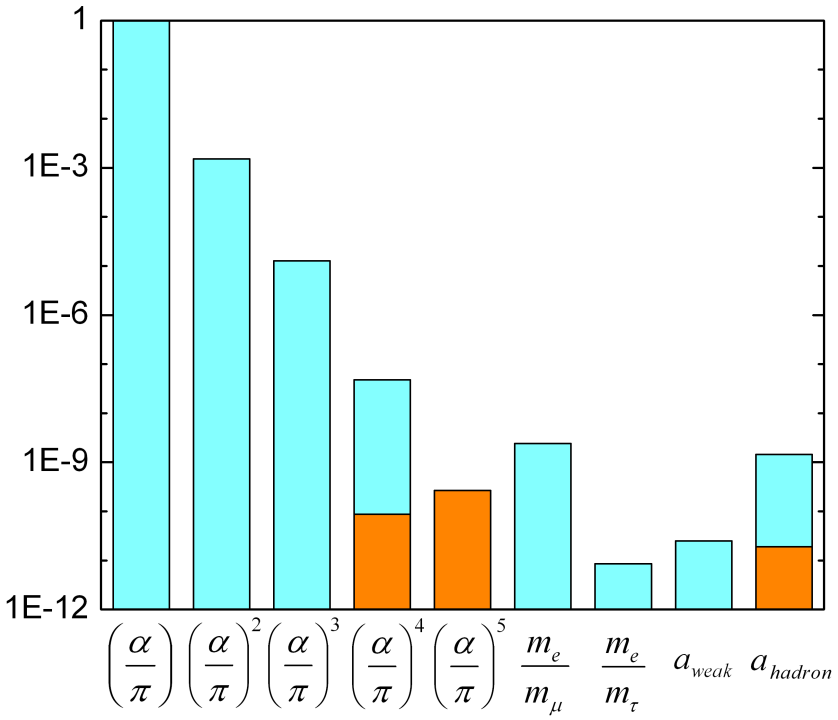

Figure 1.5: Different parts of the fine structure constant value from the $g-2$ measurement. The blue part shows how large the value is, and the orange part shows the relative uncertainty.

1.2.3 Obtaining the fine structure constant value from the recoil frequency measurement

Instead of using $g-2$ to get α, another possible way is to relate the Ryderberg constant R_∞ to the fine structure constant. We can connect the Ryderberg constant to α by

$$hcR_\infty = \frac{1}{2} m_\mathrm{e} c^2 \alpha^2, \tag{1.5}$$

where h is the Planck constant. The electron mass m_e is different than the atom mass in atom interferometers. Therefore, we rewrite the equation as

$$\alpha = \left(2 \frac{R_\infty}{c} \frac{\mathrm{u}}{m_\mathrm{e}} \frac{m}{\mathrm{u}} \frac{h}{m} \right)^{1/2}, \tag{1.6}$$

where u is the atomic mass unit, m is the atom mass used in our atom interferometer (in this case, it is ^{133}Cs). The uncertainty of determining α is shown in table 1.2. We can see

Measurements	Uncertainty (ppb)
Rydberg constant R_∞	0.005 [13]
Electron mass in amu m_e	0.40 [13]
Cesium mass in amu m	0.18 [20]

Table 1.2: Uncertainty in determining the fine structure constant from the recoil frequency.

that the overall result is limited by the uncertainty of $\hbar/m$, which is what we can improve by using our atom interferometer.

1.3 Compton clock

1.3.1 The most fundamental time scale

All timekeeping so far has been based on the internal dynamics of bound systems [21]. For example, the motion of the solar system underlies the calendar. Or the pendulum sways due to the interaction between itself and Earth. Energy levels of atoms and ions that determine the ticking rate of today's most accurate clocks [22, 23, 24, 25], while clocks based on transitions in nuclei [26, 27] are already being developed. The simplest and most fundamental reference, however, does not require any interacting particles; it is provided by a single massive particle with its Compton frequency $\omega_0 = mc^2/\hbar$. Relativity and quantum mechanics relate the particle's mass m and its energy $E = mc^2$ with frequency $E = \hbar\omega$.

The Compton frequency ω_0 is extremely high ($\sim 10^{20}$ Hz for an electron) and not directly observed. The metrological implications of the Compton frequency, however, are huge: Compared even to transitions in nuclei [26, 27], the Compton frequency of a stable particle can have a practically unlimited quality factor $Q = \omega_0\Gamma^{-1}$, where Γ^{-1} is the 1/e lifetime of the system, is virtually immune against external influences, and is thus a virtually ideal timing reference.

Its use would also allow for new precision tests of fundamental laws of physics or to define the unit of time if hypothetically coupling constants were found to vary, as its dependence on, e.g., the electromagnetic or strong interaction strengths or particle mass ratios is substantially different from conventional clocks. Maybe the most fundamental aspect is that it allows defining the second via a particle's mass and from fundamental constants and dimensionless ratios, based on first principles only. Building a Compton clock seems extremely attractive from this point of view. However, no practical method of harnessing the Compton frequency to make a clock, even with modest accuracy, has been developed until now.

1.3.2 From microwave clock to Compton clock

In 1950, Norman Ramsey demonstrated a microwave clock which is the origin of Ramsey-Bordé atom interferometers [28]. It was initially used to improve molecular beam magnetic

resonance spectroscopy. It then found applications in the construction of atomic clocks. In a microwave frequency Ramsey interferometer, atoms pass through a microwave frequency cavity, which puts the atoms into a superposition state, as shown in figure 1.6. The atoms in different energy levels will accumulate different phases. Another cavity then place the atoms back to the original state to interfere. The interference signal depends on the phase match between the matter wave and microwave, which reveals information about the atomic transition.

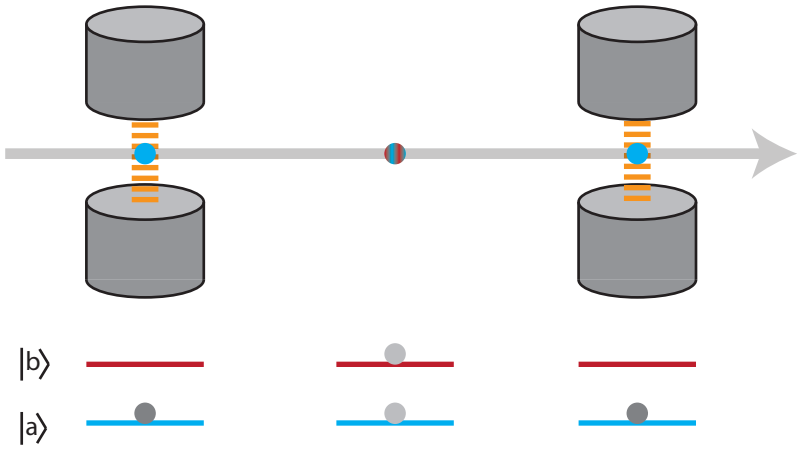

Figure 1.6: Microwave frequency Ramsey interferometer. The blue circle represents initial atoms coming out from an atomic beam with a velocity along the gray arrow and initially are in the $|a\rangle$ state. After passing through the first cavity and interacting with the microwave frequency as shown in orange dashed line, atoms are in a superposition state between $|a\rangle$ and $|b\rangle$. After a while atoms pass through the second cavity and can get returned into their original state to interfere.

This method has been further used in optical domain [29]. Instead of using a microwave to place atoms into a superposition state, an optical traveling wave is used to generate the superposition. This is called optical Ramsey method, as shown in figure 1.7. Because its frequency is higher, the overall momentum being transferred is larger. Therefore, these two states will have non-negligible space separation. This separation will decrease the overlap of matter waves, and reduce available signals. Therefore extra optical pulses are necessary to recombine these two states in space.

In these two experiments, the goal is to measure the transition frequency. When people scan the microwave frequency or optical frequency, final populations will oscillate as a function of detuning and time of flight between atom-light interactions. By fitting the fringes with theoretical calculations, the transition peak signal can be determined. The development of Ramsey-Bordé atom interferometer shifts the experiment goal from measuring transition peak to ω_r. In other words, the experiment is no longer a clock. As mentioned in the section

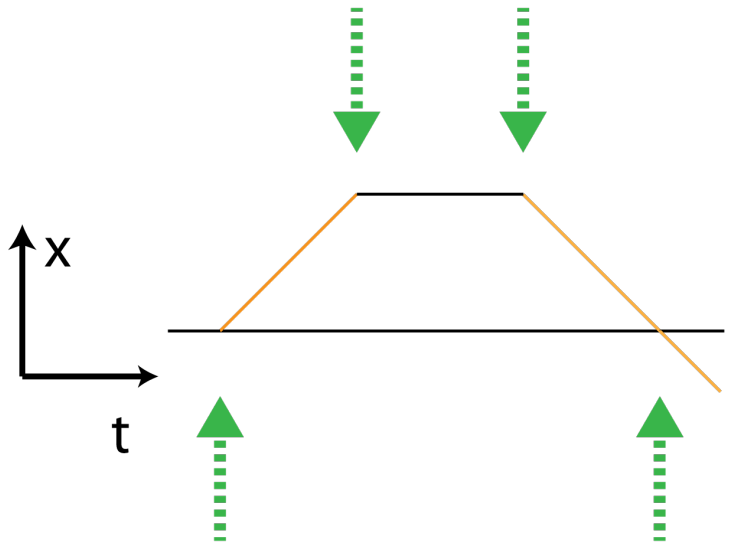

Figure 1.7: Optical frequency Ramsey interferometer. The vertical axis represents the height, and the horizontal axis indicates the time. Dashed lines show the laser light and solid lines represent the matter waves' trajectories. Black and orange solid lines represent atoms in the ground state and excited state, respectively.

1.2.3, the recoil frequency is what being measured, which includes two physical fixed properties: the atom mass and the Planck constant and also one external controllable property: the laser frequency. If we want to measure a Compton frequency, then we can just place $\hbar/m$ into the $mc^2/\hbar$ equation and obtain the value. However, for the Compton clock itself, we could like to find a way to relate laser frequency to $\hbar/m$. In other words, we would like to eliminate the dependence of laser frequency. Once we achieve it, the only physical quantity is Compton frequency, and the overall system can work as a Compton clock in a transparent way. This Compton clock is referenced to the phase accumulated between different quantum states of a particle's motion. It differs from conventional atomic clocks, which are referenced to the relative phase accumulation rate (or angular frequency) between the internal energy levels of a bound system, as shown in figure 1.8.

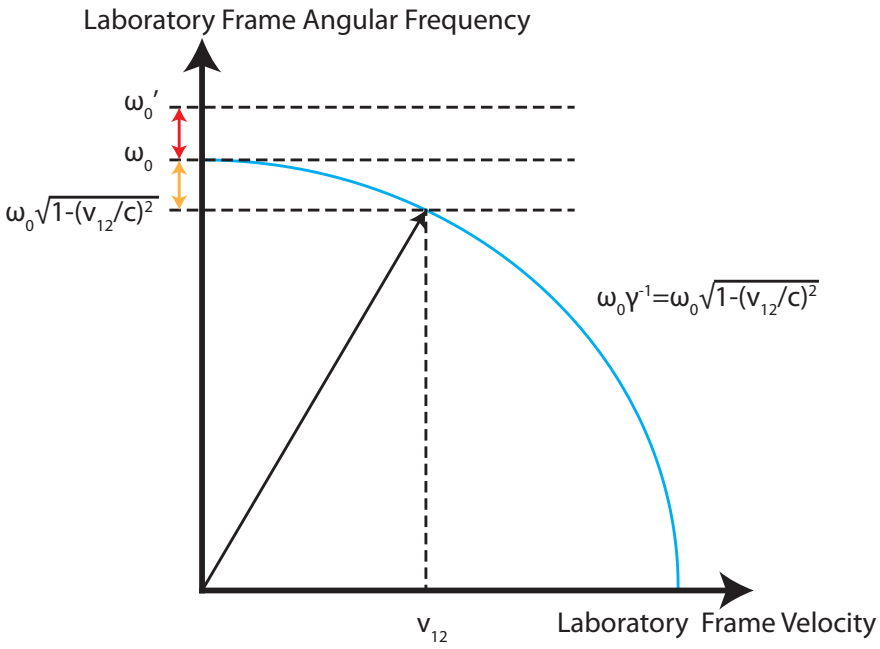

Figure 1.8: Comparison between ordinary atomic clocks and Compton clocks. Conventional atomic clocks are based on the phase accumulation rate $\Delta\omega = \omega_0' - \omega_0$ between states of different rest mass-energies (red). The rest-mass clock (Compton clock) here is based on the phase accumulation (orange) between states moving relative to each other with velocity v_{12}. The Lorentz factor γ which determines the phase accumulation rate is a function of v_{12}.

Chapter 2

Theoretical Background

2.1 Introduction

As discussed in section 1.3, we can use a Ramsey-Bordé atom interferometer to measure the recoil frequency. In Ramsey-Bordé interferometers, some atoms move relative to the others. The asymmetric movement contributes to the non-cancellation of kinetic energy-related phases, thus the recoil frequency. However, for a quantitative measurement, we need to know the relation between phases we measure and physical quantities we are concerned with.

In this chapter we will first focus on calculations that relate the phase measured by Ramsey-Bordé interferometers to the recoil frequency. The phase being calculated can be divided into two parts, free evolution phase and atom light interaction phase. The free evolution phase calculation is straightforward, but the atom light interaction phase calculation is related to experimental choices. Details in the atom light interaction will change the overall result, and we will discuss some aspects of this idea. The connection between the recoil frequency measurement and the Compton clock will also be described.

For better sensitivity, we utilize conjugate Ramsey-Boré interferometers and ellipse fitting to cancel vibrational noise, whose principles will be discussed here. With higher sensitivity, the Coriolis force and gravity gradient should also be considered. We therefore try to build models to estimate their effects on our atom interferometer.

2.2 Free evolution phase calculation

The Ramsey-Bordé atom interferometer is shown in figure 2.1. In figure 2.1, there are four beam splitters that separate atoms into different momentum states. The first two pulses make atoms transfer between 0 and $n\hbar(\vec{k_1} - \vec{k_2})$ momentum states, and the third and fourth pulses drive the atoms originally from 0 momentum to $-n\hbar(\vec{k_1} + \vec{k_2})$ momentum, where $\vec{k_1}$ and $\vec{k_2}$ are the wave vectors of counter-propagating photons in our matter wave beam splitter and n is the Bragg order. If two photons are being transferred, $n = 1$. For four photons,

$n = 2$, and so on. The value of momentum being transferred can be written as $n\hbar(k_1 + k_2)$ and $-n\hbar(k_1 + k_2)$. The phase of atoms in certain trajectories can be calculated from two parts: the free evolution phase and the atom-light interaction phase. We will discuss the free evolution phase here and leave the atom-light interaction phase for section 2.3.

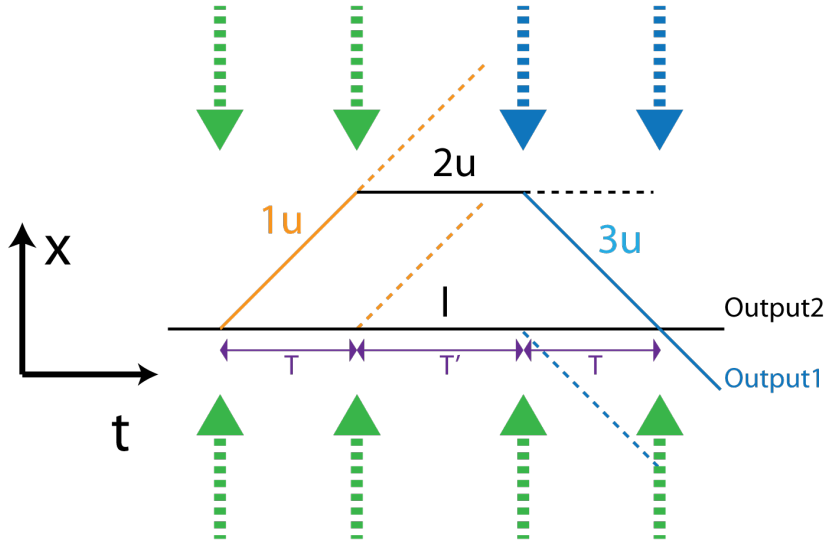

Figure 2.1: Ramsey-Bordé interferometer sketch. The vertical axis relates to the space coordinate x, and the horizontal axis relates to the time coordinate t. Atoms' trajectories here are not affected by gravity. Atoms at rest are shown with black lines. Atoms with $n\hbar(k_1+k_2)$ and $-n\hbar(k_1+k_2)$ momentum are shown with orange and blue lines, respectively. The labels (1u, 2u, 3u, l) represent different segment of atoms' trajectories. Light is shown with dashed arrows. For each beam splitter, there will be a pair of counter-propagating beams. Because of different averaged velocities, different frequencies are required for the beam splitter of matter waves. Therefore there are blue dashed arrows which represent different laser frequency. After each beam splitter atoms will have two possible velocities, but not all of them contribute to the final atom interferometer. Atoms do not contribute are drawn in dotted lines. The time separation between first two pairs of beam splitters and the last two pairs of beam splitters is T and the time separation between these two pairs is T'. Output 1 and output 2 indicate two atom clouds with different averaged velocity and can be detected to calculate the phase information in atom interferometers.

The free evolution phase $\Delta\Phi_{\text{free}}$ can be calculated from the classical action, as shown in equation (1.1). The atoms' trajectories are necessary to determine the phase, which can be obtained by solving the differential equation, in the semiclassical limit,

$$\ddot{x}(t) = f(x(t)), \tag{2.1}$$

where x is the coordinate of trajectories, and $f(x(t))$ is a function of x. We can calculate the trajectories of atoms by combining equation (2.1) and initial conditions. At first we consider a case when there is no gravity (i.e., $f(x(t)) = 0$). The trajectories of a Ramsey-Bordé interferometer under this assumption will be

$$x_{\mathrm{l}}(t) = x_0 \equiv 0, \tag{2.2}$$

$$x_{1\mathrm{u}}(t) = v_0 t, \tag{2.3}$$

$$x_{2\mathrm{u}}(t) = v_0 T, \tag{2.4}$$

$$x_{3\mathrm{u}}(t) = v_0 T - v_0 t, \tag{2.5}$$

where l, 1u, 2u, 3u are paths shown in figure 2.1. Here x_0 is the initial position, v_0 is the initial velocity, and T is the time separation. Once we know the trajectories, the phase difference between two trajectories can be calculated by equation (1.1) as

$$\begin{aligned} &\Delta\Phi_{\mathrm{free,1u}} + \Delta\Phi_{\mathrm{free,2u}} + \Delta\Phi_{\mathrm{free,3u}} - \Delta\Phi_{\mathrm{free,l}} \\ =&\frac{2n^2 m v_{\mathrm{r}}^2}{\hbar} T + 0 + \frac{2n^2 m v_{\mathrm{r}}^2}{\hbar} T - 0 \\ =&\frac{4n^2 m v_{\mathrm{r}}^2}{\hbar} T, \end{aligned} \tag{2.6}$$

where we set $v_0 = 2nv_{\mathrm{r}}$. The recoil velocity v_{r} is defined as $\hbar(k_1 + k_2)/2m$. For simplicity, we now consider the gravitational potential as a perturbation, and we integrate the phase along the original trajectory, which yields

$$\Delta\Phi_{\mathrm{free,l}} = 0, \tag{2.7}$$

$$\Delta\Phi_{\mathrm{free,1u}} = -\frac{1}{2\hbar} m g^2 T^3 + \frac{2n^2}{\hbar} m v_{\mathrm{r}}^2 T, \tag{2.8}$$

$$\Delta\Phi_{\mathrm{free,2u}} = -2n\frac{m g v_{\mathrm{r}}}{\hbar} T T', \tag{2.9}$$

$$\Delta\Phi_{\mathrm{free,3u}} = -\frac{1}{2\hbar} m g^2 T^3 + \frac{2n^2}{\hbar} m v_{\mathrm{r}}^2 T. \tag{2.10}$$

Taking the difference between two trajectories results in

$$\Delta\Phi_{\mathrm{free}} = \frac{4n^2 m v_{\mathrm{r}}^2}{\hbar} T - \frac{2nmgv_{\mathrm{r}}}{\hbar}(T + T')T. \tag{2.11}$$

There are two terms in the phase difference, the first term depends only on the recoil velocity v_{r} and the last term also depends on the gravity g. In the experiment, vibrations of apparatus are indistinguishable from the local gravity. Therefore, in order to measure the recoil frequency by this scheme, we need to stabilize the acceleration term. We can achieve this goal by installing a vibration cancellation system. Or we can cancel the vibration effect

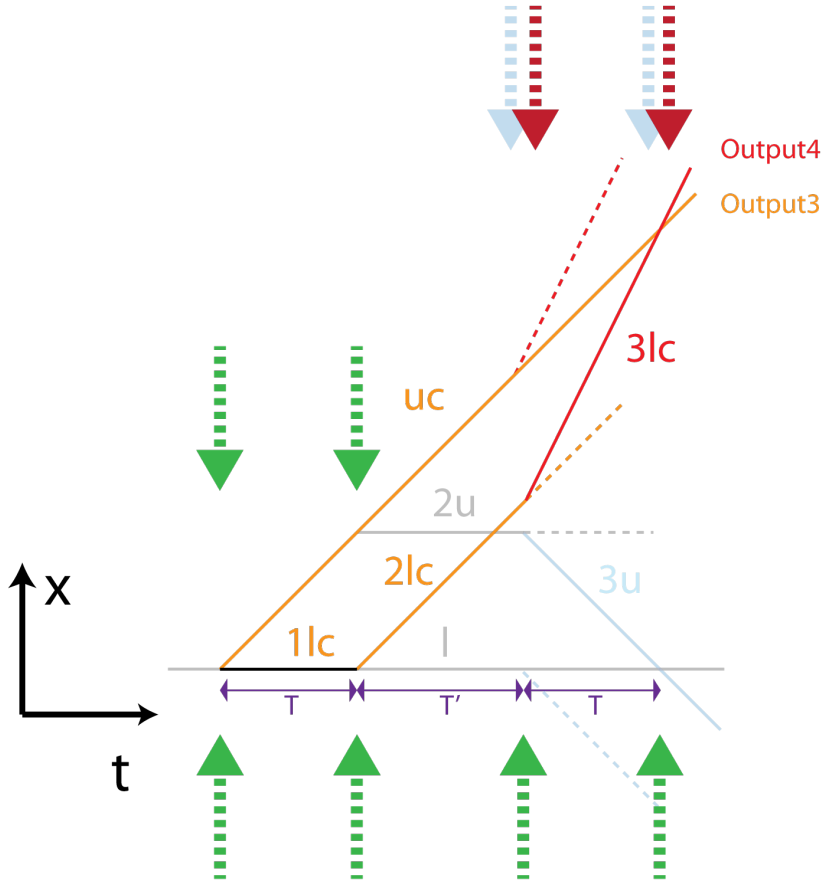

Figure 2.2: A pair of conjugate Ramsey-Bordé interferometers. Symbols are similar as in figure 2.1. The original Ramsey-Bordé atom interferometer is shown in half-transparency. Atoms with $2n\hbar(k_1 + k_2)$ momentum are shown in red line. The beam splitters that drive the third and fourth pulses in the conjugate atom interferometer include laser beams with different frequency than the original ones. They are represented by red dashed arrows.

out by running another conjugate Ramsey-Bordé interferometer, as shown in figure 2.2, at the same time. Its free evolution phase is

$$\Delta\Phi_{\text{free,uc}} = \frac{1}{\hbar} nmv_{\text{r}}(2T + T')\left[2nv_{\text{r}} - g(2T + T')\right], \tag{2.12}$$

$$\Delta\Phi_{\text{free,1lc}} = 0, \tag{2.13}$$

$$\Delta\Phi_{\text{free, 2lc}} = \frac{1}{\hbar} nmv_{\text{r}}T'(2nv_{\text{r}} - gT'), \tag{2.14}$$

$$\Delta\Phi_{\text{free, 3lc}} = -\frac{2nmv_{\text{r}}}{\hbar} T\left[g(T + T') - 4nv_{\text{r}}\right], \tag{2.15}$$

where the c subscript stands for conjugate. Taking the difference between two trajectories results in

$$\Delta\Phi_{\text{free,c}} = -\frac{4n^2 m v_{\text{r}}^2}{\hbar} T - \frac{2mngv_{\text{r}}}{\hbar}(T + T')T. \tag{2.16}$$

The phase difference of this conjugate Ramsey-Bordé atom interferometer includes the same term as the original one but with different sign. However, we only consider the free evolution phase in this calculation. We are going to show the relation holds even in the complete phase calculation.

2.3 Atom-light interaction phase calculation

For atom-light interaction related phase, we can acknowledge something useful from the basic properties of beam splitters. From the requirement of atom-number conservation, the relative phase between different ports of the beam splitter can be partially determined [30], as shown in figure 2.3.

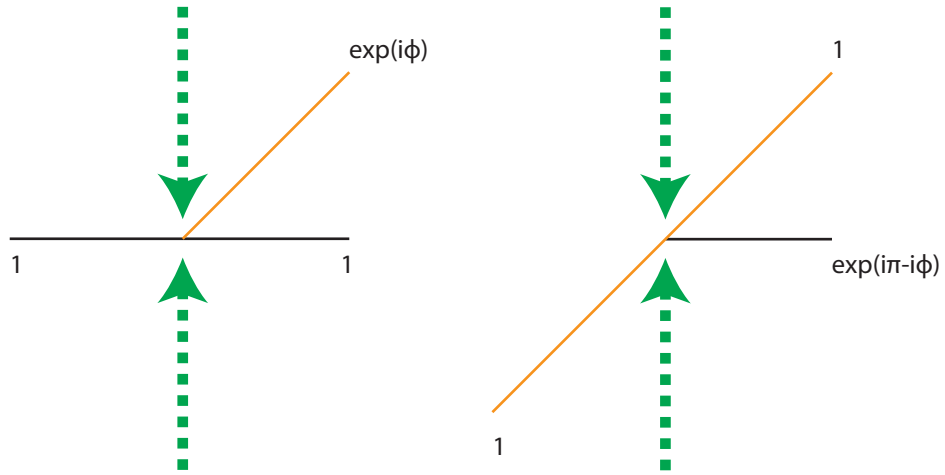

Figure 2.3: Relationship between two ports of an ideal beam splitter under two possible inputs. On the left hand side, we choose the input phase as reference and the pass-through output will not be affected. The beam splitter may introduce some extra phase ϕ for the reflected one. Under the same condition of the beam splitter, when atoms enter into another port (right hand side), the reflected one will bring extra phase as $\pi - \phi$.

Here we assume first that each beam splitter in our Ramsey-Bordé interferometer will introduce relative phase $-\pi/2$ for atoms being reflected, which will be verified in section 2.6.1.

From the relation addressed in figure 2.3, the value is equal to $\pi - (-\pi/2) = 3\pi/2 = -\pi/2 \pmod{2\pi}$, therefore the reflected outputs of the beam splitters in both cases have the same phase shift. For the atom-light interaction phase, instead of this $-\pi/2$ phase which comes from the state change of atoms, extra phase will be obtained from absorption or emission of photons. Combining these information, we can try to calculate the population. For example, the population of output 1 in figure 2.1 is a result of interference between the upper and lower paths. The upper path results from the path 1u+2u+3u and gets non-reflected by the final beam splitter, therefore the overall phase is

$$\Delta\Phi_{\text{u,output 1}} = \frac{4mn^2v_{\text{r}}^2T}{\hbar} - \frac{2mngv_{\text{r}}(T^2+TT')}{\hbar} - \pi/2 + \phi_1 - \pi/2 - \phi_2 - \pi/2 - \phi_3 + 0, \quad (2.17)$$

where ϕ_i is the phase laser being imprinted onto the atoms. The index i runs from 1 to 4 and corresponds to each single beam splitter in sequence. The plus or minus sign before ϕ_i corresponds to the increase or decrease of atoms' momentum after this beam splitter, respectively. The other path that contributes to output 1 comes from the lower path l and gets reflected by the final beam splitter, which yields

$$\Delta\Phi_{\text{l,output 1}} = 0 + 0 + 0 - \pi/2 - \phi_4. \quad (2.18)$$

The probability that we measure atoms at output 1 is therefore

$$\begin{aligned}
&P_{\text{output 1}} \\
=&\frac{1}{4}\left|e^{i\Delta\Phi_{\text{u,output 1}}} + e^{i\Delta\Phi_{\text{l,output 1}}}\right|^2 \\
=&\frac{1}{4}\left|e^{i\Delta\Phi_{\text{u,free}}}e^{-i3\pi/2}e^{i(\phi_1-\phi_2-\phi_3)} + e^{i\Delta\Phi_{\text{l,free}}}e^{i(-\phi_4)}e^{-i\pi/2}\right|^2 \\
=&\frac{1}{4}\left|-e^{i\Delta\Phi_{\text{u,free}}}e^{i(\phi_1-\phi_2-\phi_3)} + e^{i\Delta\Phi_{\text{l,free}}}e^{-i\phi_4}\right|^2 \\
=&\frac{1}{2}\left[1-\cos\left(\Delta\Phi_{\text{u,free}} + \phi_1 - \phi_2 - \phi_3 + \phi_4 - \Delta\Phi_{\text{l,free}}\right)\right] \\
=&\frac{1}{2}\left\{1-\cos\left[4\frac{n^2mv_{\text{r}}^2T}{\hbar} - 2\frac{nmgv_{\text{r}}(T^2+TT')}{\hbar} + \phi_1 - \phi_2 - \phi_3 + \phi_4\right]\right\},
\end{aligned} \quad (2.19)$$

where we assume the amplitudes of different paths are the same. Different amplitudes will just decrease the visibility of interference fringes. We can have similar arguments for the output 2, and the two possible paths have phases

$$\Delta\Phi_{\text{u,output 2}} = \frac{4n^2mv_{\text{r}}^2T}{\hbar} - \frac{2nmgv_{\text{r}}(T^2+TT')}{\hbar} - \pi/2 + \phi_1 - \pi/2 - \phi_2 - \pi/2 - \phi_3 - \pi/2 + \phi_4, \quad (2.20)$$

$$\Delta\Phi_{\text{l,output 2}} = 0 + 0 + 0 + 0. \quad (2.21)$$

The probability of measuring signals from output 2 will be

$$\begin{aligned}
&P_{\text{output 2}}\\
=&\frac{1}{4}\left|e^{i\Delta\Phi_{\text{u,output 2}}}+e^{i\Delta\Phi_{\text{l,output 2}}}\right|^2\\
=&\frac{1}{4}\left|e^{i\Delta\Phi_{\text{u,free}}}e^{-2i\pi}e^{i(\phi_1-\phi_2-\phi_3+\phi_4)}+e^{i\Delta\Phi_{\text{l,free}}}\right|^2\\
=&\frac{1}{4}\left|e^{i\Delta\Phi_{\text{u,free}}}e^{i(\phi_1-\phi_2-\phi_3+\phi_4)}+e^{i\Delta\Phi_{\text{l,free}}}\right|^2\\
=&\frac{1}{2}\left[1+\cos\left(\Delta\Phi_{\text{u,free}}+\phi_1-\phi_2-\phi_3+\phi_4-\Delta\Phi_{\text{l,free}}\right)\right]\\
=&\frac{1}{2}\left\{1+\cos\left[4\frac{n^2mv_{\text{r}}^2T}{\hbar}-2\frac{nmgv_{\text{r}}(T^2+TT')}{\hbar}+\phi_1-\phi_2-\phi_3+\phi_4\right]\right\}.
\end{aligned}\tag{2.22}$$

We can define the contrast as the difference of outputs divided by the sum of outputs, which yields

$$\frac{P_{\text{output 2}}-P_{\text{output 1}}}{P_{\text{output 2}}+P_{\text{output 1}}}=\cos\left[\frac{4n^2mv_{\text{r}}^2T}{\hbar}-\frac{2nmgv_{\text{r}}(T^2+TT')}{\hbar}+\phi_1-\phi_2-\phi_3+\phi_4\right].\tag{2.23}$$

For the other conjugate Ramsey-Bordé atom interferometer, the probability that we measure atoms at output 3 is therefore

$$\begin{aligned}
&P_{\text{output 3}}\\
=&\frac{1}{4}\left|e^{i\Delta\Phi_{\text{cu,free}}}e^{i\phi_1}e^{-i\pi/2}+e^{i\Delta\Phi_{\text{cl,free}}}e^{-i3\pi/2}e^{i(\phi_{2c}+\phi_{3c}-\phi_{4c})}\right|^2\\
=&\frac{1}{4}\left|e^{i\Delta\Phi_{\text{cu,free}}}e^{i\phi_1}-e^{i\Delta\Phi_{\text{cl,free}}}e^{i(\phi_{2c}+\phi_{3c}-\phi_{4c})}\right|^2\\
=&\frac{1}{2}\left[1-\cos\left(\Delta\Phi_{\text{cu,free}}+\phi_1-\phi_{2c}-\phi_{3c}+\phi_{4c}-\Delta\Phi_{\text{cl,free}}\right)\right]\\
=&\frac{1}{2}\left\{1-\cos\left[-4\frac{n^2mv_{\text{r}}^2T}{\hbar}-2\frac{nmgv_{\text{r}}(T^2+TT')}{\hbar}+\phi_1-\phi_{2c}-\phi_{3c}+\phi_{4c}\right]\right\},
\end{aligned}\tag{2.24}$$

where ϕ_{ic} is similar to ϕ_i, but now for the conjugate atom interferometer. Similarly, the result for output 4 is

$$\begin{aligned}
&P_{\text{output 4}}\\
=&\frac{1}{4}\left|e^{i\Delta\Phi_{\text{cu,free}}}e^{i(\phi_1+\phi_{4c})}e^{-i\pi}+e^{i\Delta\Phi_{\text{cl,free}}}e^{-i\pi}e^{i(\phi_{2c}+\phi_{3c})}\right|^2\\
=&\frac{1}{4}\left|e^{i\Delta\Phi_{\text{cu,free}}}e^{i\phi_1+\phi_{4c}}+e^{i\Delta\Phi_{\text{cl,free}}}e^{i(\phi_{2c}+\phi_{3c})}\right|^2\\
=&\frac{1}{2}\left[1+\cos\left(\Delta\Phi_{\text{cu,free}}+\phi_1-\phi_{2c}-\phi_{3c}+\phi_{4c}-\Delta\Phi_{\text{cl,free}}\right)\right]\\
=&\frac{1}{2}\left\{1+\cos\left[-4\frac{n^2mv_{\text{r}}^2T}{\hbar}-2\frac{nmgv_{\text{r}}(T^2+TT')}{\hbar}+\phi_1-\phi_{2c}-\phi_{3c}+\phi_{4c}\right]\right\}.
\end{aligned}\tag{2.25}$$

If we take the contrast definition similar as before, then

$$\frac{P_{\text{output 4}} - P_{\text{output 3}}}{P_{\text{output 4}} + P_{\text{output 3}}} = \cos\left[-\frac{4n^2 m v_{\text{r}}^2 T}{\hbar} - \frac{2nmgv_{\text{r}}(T^2 + TT')}{\hbar} + \phi_1 - \phi_{2c} - \phi_{3c} + \phi_{4c}\right]. \tag{2.26}$$

We can complete the equation once we know the values of ϕ_i and ϕ_{ic}, which originate from the laser phase.

2.3.1 Laser phase

For calculating ϕ_{i} in the previous section, we will consider one pair of counter-propagating beams, in which atoms absorb light from upward-going beam, emit light downwards and change $\hbar(k_1 + k_2)$ momentum. The phase of laser light depends on its spatial position and timing. The laser phases in the four beam splitters will contribute differently to the atoms. Here we adopt the same assumption of the first order perturbation as in the free evolution phase calculation. The laser phase of the first beam splitter, under the plane wave approximation, can be assigned as

$$\phi_1 = -2k_2 L, \tag{2.27}$$

where L is the length between the first beam splitter and the retro-reflected mirror, and k_2 is the wave number of the retro-reflected light. Here we define the initial timing $t \equiv 0$ and initial position $x \equiv 0$, therefore at this beam splitter the phase from the upward-going laser beam equals to zero, and the phase from the downward-going beam equals to $2k_2 L$. For the second beam splitter, the phase will be

$$\phi_2 = \omega_1 T + k_1 z_1 - \omega_2 T - k_2(2L - z_1), \tag{2.28}$$

where z_1 is the position of this beam splitter, and ω_1 and ω_2 are the angular frequency of laser with k_1 and k_2 wave vector, respectively. For the third pulse, the phase will be

$$\phi_3 = \omega_1(T + T') + k_1 z_1 - (\omega_2 - \omega_{\text{m}})(T + T') - (k_2 - \delta k)(2L - z_1), \tag{2.29}$$

where ω_{m} is the frequency shift for the third and fourth pulses. In addition, here δk is the wave vector difference between the first two pulses and the last two pulses. The phase of the fourth one will be

$$\phi_4 = \omega_1(2T + T') - (\omega_2 - \omega_{\text{m}})(2T + T') - (k_2 - \delta k)(2L). \tag{2.30}$$

We can put these into $(\phi_1 - \phi_2 - \phi_3 + \phi_4)$, as shown in equation (2.23), and multiply it by n if we want to consider $2n$-photon transitions. It brings the phase $\Delta\Phi_{\text{laser}}$ to be

$$n\left[\omega_{\text{m}} T + z_1(\delta k - 2k_1 - 2k_2)\right]. \tag{2.31}$$

The value of z_1 can be substituted as $n\hbar(k_1 + k_2)T/m$, which yields

$$\Delta\Phi_{\text{laser}} = n\left[\omega_{\text{m}} T + n\hbar\frac{(k_1 + k_2)(\delta k - 2k_1 - 2k_2)}{m}T\right]. \tag{2.32}$$

For simplicity, we can regard $\delta k \to 0$, because the value is usually small compared with k_1 or k_2. The frequency $\omega_{\rm m}$ cannot be neglected because it is comparable to the recoil frequency. Combining this with the free evolution phase $\Delta\Phi_{\rm free}$ from equation (2.11) yields

$$\begin{aligned}
&\Delta\Phi_{\rm laser} + \Delta\Phi_{\rm free} \\
=&\Delta\Phi_{\rm laser} + 4n^2\frac{mv_{\rm r}^2T}{\hbar} - \frac{2nmgv_{\rm r}}{\hbar}(T+T')T \\
=&n\left[\omega_{\rm m}T - 2n\hbar\frac{(k_1+k_2)^2}{m}T\right] + \frac{4n^2mv_{\rm r}^2T}{\hbar} - \frac{2nmgv_{\rm r}}{\hbar}(T+T')T \\
=&n\left[\omega_{\rm m}T - n\hbar\frac{(k_1+k_2)^2}{m}T\right] - \frac{2nmgv_{\rm r}}{\hbar}(T+T')T. \qquad (2.33)
\end{aligned}$$

This shows the overall phase we can retrieve from the population of the original Ramsey-Bordé atom interferometer, as shown in equation (2.23). We can do the same thing for the other conjugate Ramsey-Bordé interferometer. The phases are

$$\phi_{2\rm c} = \omega_1 T - \omega_2 T - 2k_2 L, \qquad (2.34)$$

$$\phi_{3\rm c} = \omega_1(T+T') + k_1 z_1 - (\omega_2+\omega_{\rm m})(T+T') - (k_2+\delta k)(2L - z_1), \qquad (2.35)$$

$$\phi_{4\rm c} = \omega_1(2T+T') + k_1 z_2 - (\omega_2+\omega_{\rm m})(2T+T') - (k_2+\delta k)(2L - z_2). \qquad (2.36)$$

Placing these into the equation $n(\phi_1 - \phi_{2c} - \phi_{3c} + \phi_{4c})$ will result in

$$\Delta\Phi_{\rm laser,c} = -n\left[\omega_{\rm m}T + (z_1 - z_2)(\delta k + k_1 + k_2)\right]. \qquad (2.37)$$

The value of z_1 can be substituted as $n\hbar(k_1+k_2)T'/m$, z_2 can be substituted as $n\hbar(k_1+k_2)T'/m + 2n\hbar(k_1+k_2)T/m$. After the replacement,

$$\Delta\Phi_{\rm laser,c} = -n\left[\omega_{\rm m}T - 2n\hbar\frac{(k_1+k_2)(\delta k + k_1 + k_2)}{m}T\right]. \qquad (2.38)$$

Under similar assumptions, the sum up of the phases in the other conjugate Ramsey-Bordé interferometer will be

$$\begin{aligned}
&\Delta\Phi_{\rm laser,c} + \Delta\Phi_{\rm free,c} \\
=&\Delta\Phi_{\rm laser,c} - 4n^2\frac{mv_{\rm r}^2T}{\hbar} - 2n\frac{mgv_{\rm r}}{\hbar}(T+T')T \\
=&-n\left[\omega_{\rm m}T - 2n\hbar\frac{(k_1+k_2)^2}{m}T\right] - 4n^2\frac{mv_{\rm r}^2T}{\hbar} - 2n\frac{mgv_{\rm r}}{\hbar}(T+T')T \\
=&-n\left[\omega_{\rm m}T - n\hbar\frac{(k_1+k_2)^2}{m}T\right] - 2n\frac{mgv_{\rm r}}{\hbar}(T+T')T. \qquad (2.39)
\end{aligned}$$

If we insert the value of $\Delta\Phi_{\rm laser}$ and $\Delta\Phi_{\rm laser,c}$ into equation (2.23) and (2.26), respectively, then in the two fringes the relative signs between gravitational potential terms and kinetic energy terms are different, as expected. It suggests that if we can reject the gravitational term between these two plots, than we can acquire the property which is linked to the recoil frequency and immune to vibrational noise. This is what can be done in ellipse fitting.

2.4 Phase calculation for trajectories with gravity

Before entering the ellipse fitting section, we want to justify the selection of the perturbation calculation. In the previous sections we treat the gravitational potential as a perturbation when calculating the phase. We can also consider the effect of gravity to the atoms' trajectories and calculate the phase. For considering the gravity, the trajectories for the original Ramsey-Bordé interferometer will now become

$$x_{\mathrm{l}}(t) = -\frac{gt^2}{2}, \tag{2.40}$$

$$x_{1\mathrm{u}}(t) = -\frac{gt^2}{2} + 2nv_{\mathrm{r}}t, \tag{2.41}$$

$$x_{2\mathrm{u}}(t) = -\frac{gt^2}{2} - gtT + x_{1\mathrm{u}}(T), \tag{2.42}$$

$$x_{3\mathrm{u}}(t) = -\frac{gt^2}{2} - \left[g(T+T') + 2nv_{\mathrm{r}}\right]t + x_{2\mathrm{u}}(T'). \tag{2.43}$$

The phase for the original Ramsey-Bordé interferometer will be

$$\Delta\Phi_{\mathrm{free}} = 4n^2\frac{mv_{\mathrm{r}}^2T}{\hbar}, \tag{2.44}$$

$$\Delta\Phi_{\mathrm{laser}} = nT\left[\omega_{\mathrm{m}} + n\hbar\frac{(k_1+k_2)(\delta k - 2k_1 - 2k_2)}{m} - \frac{2mgv_{\mathrm{r}}}{\hbar}(T+T')\right]. \tag{2.45}$$

We can see these two parts of the phase are different than in equation (2.11) and (2.32). However, the summation of these two gives us the same result as in equation (2.33). Calculations in the other conjugate Ramsey-Bordé interferometer case will yield the same conclusion. Therefore, the perturbation method results in the same outcome as the complete phase calculation in the case of a constant gravitational field [31].

2.5 Ellipse fitting

In the experiment we need to extract the relative phase between two signals to get the recoil frequency. We can do ellipse fitting to achieve this. By drawing the lower fringe along the x axis and the upper one along the y axis, these two plots will produce an ellipse even through each of them does not seem to have observable patterns, which is demonstrated by figure 2.4.

For the plots of fringes, we can define coordinates as

$$x = O_{\mathrm{x}} + A_{\mathrm{x}}\cos\left(\phi_{\mathrm{c}} + \phi_{\mathrm{d}}\right), \tag{2.46}$$

$$y = O_{\mathrm{y}} + A_{\mathrm{y}}\cos\left(\phi_{\mathrm{c}} - \phi_{\mathrm{d}}\right), \tag{2.47}$$

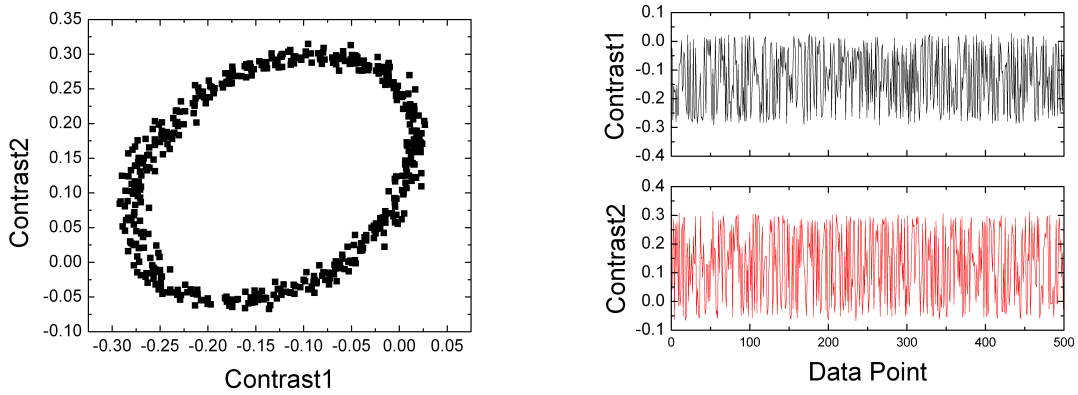

(a) Data taken as a whole ellipse from two fringes.

(b) Individual data points in a time sequence.

Figure 2.4: Demonstration of ellipse fitting. The red line and black line show the contrast in each atom interferometer branch. We can see the full fluctuation of signals. However, when drawn together, the hidden structure can be shown and useful information can be extracted.

where O_{x} , O_{y} are offsets of the fringe and A_{x} , A_{y} are the amplitudes. The offsets come from the atoms which do not participate into the interference. The common phase is ϕ_{c} and the differential phase is ϕ_{d}. In our case, ϕ_{d} corresponds to the phase related to the recoil frequency, and ϕ_{c} relates to the phase from the gravity and vibrations. Expressing them as equations yields

$$\phi_{\mathrm{d}} = n\left[\omega_{\mathrm{m}}T - n\hbar\frac{(k_1+k_2)^2}{m}T\right], \tag{2.48}$$

$$\phi_{\mathrm{c}} = -2n\frac{mgv_{\mathrm{r}}}{\hbar}(T+T')T. \tag{2.49}$$

We can adjust ω_{m} to make $\phi_{\mathrm{d}} = 0$, which results in

$$\omega_{\mathrm{m}} = \frac{n\hbar(k_1+k_2)^2}{m} \approx 8n\omega_{\mathrm{r}}. \tag{2.50}$$

For the final part of the above equation we assume that $k_1 \approx k_2 = k$. We can then obtain the value of $\hbar/m$ from the frequency ω_{m} and the laser frequency we choose.

For ellipse fitting and acquiring the value of ϕ_{d}, we define new parameters as

$$X \equiv \frac{(x-O_{\mathrm{x}})}{2A_{\mathrm{x}}} = \frac{\cos(\phi_{\mathrm{c}}+\phi_{\mathrm{d}})}{2} = \frac{\cos\phi_{\mathrm{c}}\cos\phi_{\mathrm{d}} - \sin\phi_{\mathrm{c}}\sin\phi_{\mathrm{d}}}{2}, \tag{2.51}$$

$$Y \equiv \frac{(y-O_{\mathrm{y}})}{2A_{\mathrm{y}}} = \frac{\cos(\phi_{\mathrm{c}}-\phi_{\mathrm{d}})}{2} = \frac{\cos\phi_{\mathrm{c}}\cos\phi_{\mathrm{d}} + \sin\phi_{\mathrm{c}}\sin\phi_{\mathrm{d}}}{2}. \tag{2.52}$$

Then we have

$$\frac{X+Y}{\cos\phi_{\mathrm{d}}} = \cos\phi_{\mathrm{c}}, \tag{2.53}$$

$$\frac{Y-X}{\sin\phi_{\mathrm{d}}}=\sin\phi_{\mathrm{c}}. \tag{2.54}$$

Therefore

$$\left(\frac{X+Y}{\cos\phi_{\mathrm{d}}}\right)^2+\left(\frac{Y-X}{\sin\phi_{\mathrm{d}}}\right)^2=1, \tag{2.55}$$

which is the equation of an ellipse. In our case, the common mode phase ϕ_{c} changes in each shot due to the vibration (so we do not need to change ϕ_{c} artificially) and the differential mode phase ϕ_{d} should remain the same value. The modified coordinate X and Y will not be constant, but they all satisfy equation (2.55), which can also be written as

$$X^2-2XY\cos 2\phi_{\mathrm{d}}+Y^2=\cos^2\phi_{\mathrm{d}}\sin^2\phi_{\mathrm{d}}. \tag{2.56}$$

If we substitute X and Y back into x and y, then

$$\left[\frac{(x-O_{\mathrm{x}})}{2A_{\mathrm{x}}}\right]^2-2\frac{(x-O_{\mathrm{x}})}{2A_{\mathrm{x}}}\frac{(y-O_{\mathrm{y}})}{2A_{\mathrm{y}}}\cos 2\phi_{\mathrm{d}}+\left[\frac{(y-O_{\mathrm{y}})}{2A_{\mathrm{y}}}\right]^2=\cos^2\phi_{\mathrm{d}}\sin^2\phi_{\mathrm{d}}, \tag{2.57}$$

which can also be written as

$$\begin{aligned}&\frac{1}{4A_{\mathrm{x}}^2}x^2-2\cos 2\phi_{\mathrm{d}}\frac{1}{4A_{\mathrm{x}}A_{\mathrm{y}}}xy+\frac{1}{4A_{\mathrm{y}}^2}y^2\\&+\left(\frac{-2O_{\mathrm{x}}}{4A_{\mathrm{x}}^2}-\frac{-2O_{\mathrm{y}}}{4A_{\mathrm{x}}A_{\mathrm{y}}}\cos 2\phi_{\mathrm{d}}\right)x+\left(\frac{-2O_{\mathrm{y}}}{4A_{\mathrm{y}}^2}-\frac{-2O_{\mathrm{x}}}{4A_{\mathrm{x}}A_{\mathrm{y}}}\cos 2\phi_{\mathrm{d}}\right)y\\&+\left(\frac{O_{\mathrm{x}}^2}{4A_{\mathrm{x}}^2}+\frac{O_{\mathrm{y}}^2}{4A_{\mathrm{y}}^2}-\frac{-2O_{\mathrm{x}}O_{\mathrm{y}}}{4A_{\mathrm{x}}A_{\mathrm{y}}}\cos 2\phi_{\mathrm{d}}-\cos^2\phi_{\mathrm{d}}\sin^2\phi_{\mathrm{d}}\right)=0.\end{aligned} \tag{2.58}$$

If we can fit the data with the ellipse function $a_1x^2+a_2xy+a_3y^2+a_4x+a_5y+a_6=0$, then from the equation above the differential phase ϕ_{d} can be calculated as

$$\phi_{\mathrm{d}}=\frac{1}{2}\cos^{-1}\left(\frac{-a_2}{2\sqrt{a_1a_3}}\right). \tag{2.59}$$

There are five unknown properties $(\phi_{\mathrm{d}}, O_{\mathrm{x}}, O_{\mathrm{y}}, A_{\mathrm{x}}, A_{\mathrm{y}})$, which just match the six parameters and one condition for the ellipse equation.

Now we know how to obtain the phase from a fitted ellipse. The next question will be how to get it from experimental data. There are several different data fitting methods, and we use two of them: algebraic fitting and geometric fitting.

2.5.1 Algebraic fitting

We can write the ellipse equation as the matrix form

$$\begin{pmatrix} a_1 & a_2 & a_3 & a_4 & a_5 & a_6 \end{pmatrix} \begin{pmatrix} x^2 \\ xy \\ y^2 \\ x \\ y \\ 1 \end{pmatrix} \equiv \mathbf{a}^T \cdot \mathbf{x} = 0. \tag{2.60}$$

If the coordinates (x, y) can not be perfectly fitted into the ellipse, then $\mathbf{a}^T \cdot \mathbf{x} \neq 0$. Therefore with the total n data $\mathbf{x}_i$, we would like to seek $\mathbf{a}^T$ such that it minimizes

$$G = \sum_{i=1}^{n} (\mathbf{a}^T \cdot \mathbf{x}_i)^2. \tag{2.61}$$

In order to avoid the trivial solution $\mathbf{a}^T = 0$, some constrains must be added. We can choose the constraint such that the result is for sure an ellipse. The constraint can be $4a_1a_3 - a_2^2 = 1$ [32], which means

$$\mathbf{a}^T \cdot \begin{pmatrix} 0 & 0 & 2 & 0 & 0 & 0 \\ 0 & -1 & 0 & 0 & 0 & 0 \\ 2 & 0 & 0 & 0 & 0 & 0 \\ 0 & 0 & 0 & 0 & 0 & 0 \\ 0 & 0 & 0 & 0 & 0 & 0 \\ 0 & 0 & 0 & 0 & 0 & 0 \end{pmatrix} \cdot \mathbf{a} \equiv \mathbf{a}^T \cdot \mathbf{C} \cdot \mathbf{a} = 1. \tag{2.62}$$

We can also write G as

$$G = \sum_{i=1}^{n} (\mathbf{a}^T \cdot \mathbf{x}_i)^2 \equiv \mathbf{a}^T \cdot \mathbf{D}^T \cdot \mathbf{D} \cdot \mathbf{a}, \tag{2.63}$$

where

$$\mathbf{D} = \begin{pmatrix} \mathbf{x}_1^T \\ \mathbf{x}_2^T \\ \mathbf{x}_3^T \\ \mathbf{x}_4^T \\ \mathbf{x}_5^T \\ \mathbf{x}_6^T \\ \vdots \\ \mathbf{x}_n^T \end{pmatrix} = \begin{pmatrix} x_1^2 & x_1y_1 & y_1^2 & x_1 & y_1 & 1 \\ x_2^2 & x_2y_2 & y_2^2 & x_2 & y_2 & 1 \\ x_3^2 & x_3y_3 & y_3^2 & x_3 & y_3 & 1 \\ x_4^2 & x_4y_4 & y_4^2 & x_4 & y_4 & 1 \\ x_5^2 & x_5y_5 & y_5^2 & x_5 & y_5 & 1 \\ x_6^2 & x_6y_6 & y_6^2 & x_6 & y_6 & 1 \\ \vdots & \vdots & \vdots & \vdots & \vdots & \vdots \\ x_n^2 & x_ny_n & y_n^2 & x_n & y_n & 1 \end{pmatrix}. \tag{2.64}$$

We want minimize $\mathbf{a}^T \cdot \mathbf{D}^T \cdot \mathbf{D} \cdot \mathbf{a}$ under the condition $\mathbf{a}^T \cdot \mathbf{C} \cdot \mathbf{a} = 1$. We can use Lagrange multipliers, which combined with differentiating the equation (2.62) and (2.63) with $\mathbf{a}^T$ yields

$$\mathbf{D}^T \cdot \mathbf{D} \cdot \mathbf{a} - \lambda \mathbf{C} \cdot \mathbf{a} = 0. \tag{2.65}$$

This eigensystem can be solved to get the corresponding eigenvalues λ_i and also eigenvectors $\mathbf{u}_i$. The eigenvector $\mathbf{u}_i$, with the scalar parameter μ_i can be put back to the requirement $\mu_i \mathbf{u}_i^T \cdot \mathbf{C} \cdot \mu_i \mathbf{u}_i = 1$ to obtain the right value of μ_i. There will be at most six different eigenvalues. However, under the constraint $4a_1a_3 - a_2^2 = 1$, there exist only one positive eigenvalue and therefore corresponds to the single solution of this fitting [32].

2.5.2 Geometric fitting

Algebraic fitting above is under the assumption which requires to minimize the deviation $\sum_{i=1}^{n}(a_1x_i^2 + a_2x_iy_i + a_3y_i^2 + a_4x_i + a_5y_i + a_6)^2$, since the value should be zero for a perfect fitted ellipse. We can also try to minimize the geometric distance between the data points and the supposed fitting curve. This fitting method is called geometric fitting [33].

For geometric fitting, we would like to minimize the total distance from data points to the guessed ellipse. We can write the distance function as $f(u)$, and minimize $\sum_{i=1}^{n} f_i(u)^2$, where u identifies the parameters of ellipse fitting. The Gauss-Newton method can be used to approximate the real solution. Assuming u as the optimized parameters, we can approximate it by $\bar{u} + h$, where $\bar{u}$ is the initial guess, then

$$f(\bar{u} + h) \approx f(\bar{u}) + J(\bar{u})h \approx 0, \tag{2.66}$$

where J is the Jacobian. We can estimate h by solving it from the equation

$$J(\bar{u})h \approx -f(\bar{u}), \tag{2.67}$$

$$h \approx -J(\bar{u})^{-1} f(\bar{u}). \tag{2.68}$$

Once the h is solved, we can add this term back and get the new estimation of $\bar{u}$. This process is then iterated several times until the uncertainty criterion is satisfied.

To obtain the function $f_i(u)$, we will first run the algebra fitting and get the initial parameter value (e.g., a_1, a_2, a_3, and so on). From these values we can calculate the initial guess of parameters, such as $\bar{O}_\mathrm{x}$, $\bar{O}_\mathrm{y}$, $\bar{A}_\mathrm{x}$, $\bar{A}_\mathrm{y}$, and $\bar{\phi}_\mathrm{d}$. In order to get the correct geometric distance, each data point should correspond to an similar ellipse compared to the initial fitting one. In order to achieve this, we first remove the offset by subtracting $\bar{O}_\mathrm{x}$, $\bar{O}_\mathrm{y}$. The resulting ellipse can be written as having semi-major axis $\bar{a}$ and semi-minor axis $\bar{b}$ and being rotated by angle $\bar{\Theta}$, like

$$x = \bar{a}\cos\Phi\cos\bar{\Theta} - \bar{b}\sin\Phi\sin\bar{\Theta}, \tag{2.69}$$

$$y = \bar{a}\cos\Phi\sin\bar{\Theta} + \bar{b}\sin\Phi\cos\bar{\Theta}, \tag{2.70}$$

where Φ plays a role like ϕ_c. We can assign another matrix to rotate axes back, which yields

$$x\cos\bar{\Theta} + y\sin\bar{\Theta} = \bar{a}\cos\Phi, \tag{2.71}$$

$$-x\sin\bar{\Theta} + y\cos\bar{\Theta} = \bar{b}\sin\Phi, \tag{2.72}$$

$$\left(\frac{x\cos\bar{\Theta}+y\sin\bar{\Theta}}{\bar{a}}\right)^2+\left(\frac{-x\sin\bar{\Theta}+y\cos\bar{\Theta}}{\bar{b}}\right)^2=1. \tag{2.73}$$

We can expand this into

$$\left(\bar{a}^2\sin^2\bar{\Theta}+\bar{b}^2\cos^2\bar{\Theta}\right)x^2+2\cos\bar{\Theta}\sin\bar{\Theta}\left(\bar{b}^2-\bar{a}^2\right)xy+\left(\bar{b}^2\sin^2\bar{\Theta}+\bar{a}^2\cos^2\bar{\Theta}\right)y^2-\bar{a}^2\bar{b}^2=0. \tag{2.74}$$

Comparing this to $a_1x^2+a_2xy+a_3y^2+a_4x+a_5y+a_6=0$, we can obtain

$$a_1-a_3=\left(\bar{b}^2-\bar{a}^2\right)\cos 2\bar{\Theta}, \tag{2.75}$$

$$\frac{a_2}{a_1-a_3}=\tan 2\bar{\Theta}. \tag{2.76}$$

Once $\bar{\Theta}$ is known, $\bar{a}$ and $\bar{b}$ are easy to acquire from the values of a_1 and a_3. From this result we can write each data point (x_i, y_i) with removed offsets as

$$x_i=R_i\left(\bar{a}\cos\Phi_i\cos\bar{\Theta}-\bar{b}\sin\Phi_i\sin\bar{\Theta}\right), \tag{2.77}$$

$$y_i=R_i\left(\bar{a}\cos\Phi_i\sin\bar{\Theta}+\bar{b}\sin\Phi_i\cos\bar{\Theta}\right). \tag{2.78}$$

Each pair of data points can fix down the values of the parameter pair R_i and Φ_i. The value of R_i gives us the geometric distance between the guess and this data point, i.e., $f_i(u)=R_i-1$. Therefore we can use the sum of $f_i(\bar{u})^2$ and equation (2.68) to calculate further corrections until the result converges.

The covariance matrix can be calculated once the Jacobian is obtained,

$$\sigma=(J^TJ)^{-1}. \tag{2.79}$$

Its diagonal term shows the uncertainty of each parameters, including ϕ_{d}. The advantage of geometric fitting is that it can relate each ellipse fitting result with individual error bar, therefore outliers of data will make a larger error bar. With geometric fitting, it will be easier to suppress the effect of outliers than algebraic fitting.

On the other side, this method does not guarantee the convergence of the minimum finding process, because the requirement of invertible Jacobian. Therefore it is not suitable to make the fitting work *in situ*. In our case, we implement the algebra fitting process to get an estimation about the fitting parameters, and then analyze it with the geometric fitting method afterwards.

From equation (2.50), we can see the correct frequency ω_{m} will totally cancel out the relative phase, leaving us zero differential phase. However, zero differential phase is not very adequate in ellipse fitting. Any small error in position will cause a large deviation. In addition, 90° of differential phase is also no good, since an ellipse of 90° will become a circle, which will easily cause the divergence of an inverse Jacobian. To make the compromise, we choose 72° as the ellipse angle we want to fit.

Instead of these two frequentist inference methods, people also use Bayesian inference method to fit the ellipse [34], which requires knowledge about the noise model of the experiment in advance.

2.6 Beam Splitters

In the previous sections we demonstrate how to calculate the phases in our atom interferometer and how to extract them from experimental data. What have not discussed yet is the details of beam splitters. Ideal beam splitter should just be at one point in space time. They should also treat atoms as a perfect two-level system. However, this is not always the case. Beam splitters take time and may include interactions between more than two states of atoms. We are going to discuss more about beam splitters here.

There are many kinds of beam splitters. Raman transitions, for example, transfer atoms between different hyperfine state and let atoms gain $\hbar(k_1 + k_2)$ momentum. In a Raman transition, atoms absorb one photon whose frequency is far detuned by Δ from the single photon transition, and excite to a so called 'virtual' excited state. At the same time, atoms in the virtual excited state get stimulated emission by another photon and make a two-photon transition into the other hyperfine state.

Unlike the Raman transitions, atoms can keep their internal electronic state using beam splitters like Bragg diffraction. In Bragg diffraction, one pair of counter-propagating beams generates a moving grating. By changing the relative frequency δ of laser beams to satisfy the energy-momentum conservation, atoms after the laser pulse will be in the same electronic internal state, but different momentum state. The advantage of the same electronic internal state will be a better immunity of environmental perturbations.

There are other ways of transferring momentum to atoms. Instead of steady frequency components in Bragg diffraction, Bloch oscillations accelerate the laser-generating optical lattice and can bring atoms into a different velocity state. The summary pictures are shown in figure 2.5.

For a Raman transition obeying the two-photon resonance condition, the effective two-photon Rabi frequency Ω_{eff} is [30]

$$\Omega_{\text{eff}} = \sum_i \frac{\Omega_{1i}\Omega_{2i}^*}{2\Delta_i}, \tag{2.80}$$

where the sum is over all the intermediate states i, Δ_i is the single photon detuning, Ω_{1i} and Ω_{2i} are the Rabi frequency of the first and second Raman transition beam, respectively.

Similarly, the effective Rabi frequency Ω_n in Bragg diffraction with Bragg order n is [35]

$$\Omega_n = \frac{\Omega_{\text{eff}}^n}{8^{n-1}(n-1)!^2\omega_{\text{r}}^{n-1}}. \tag{2.81}$$

This is under the adiabatic condition and also on multi-photon resonance. As shown in equation (2.33) and (2.39), the phase is proportional to n^2. The larger the momentum being transfered, the better the sensitivity can be. For achieving larger momentum transfer, equation (2.81) shows the main constraint in Bragg diffraction comes from the laser intensity.

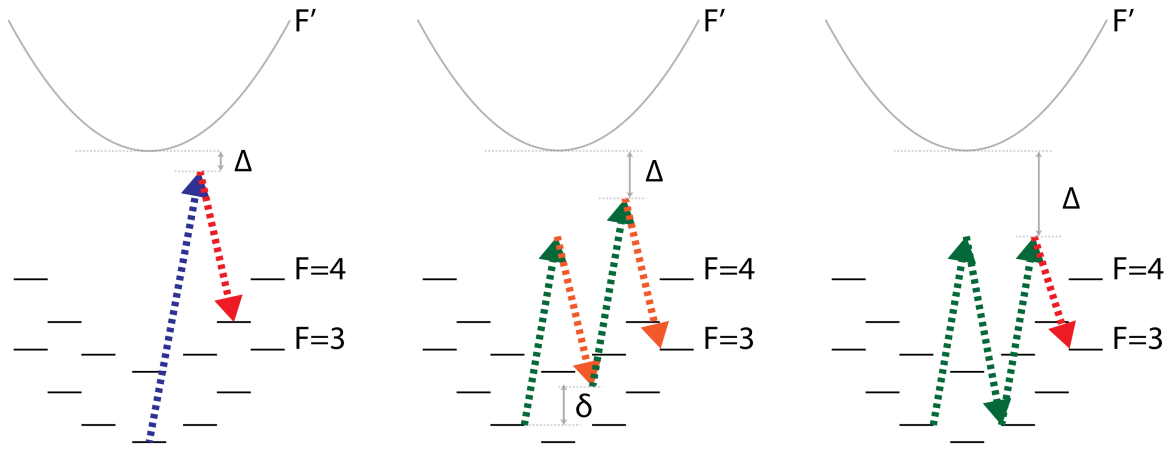

(a) Raman transition sketch. (b) Bragg diffraction sketch. (c) Bloch oscillations sketch.

Figure 2.5: Sketches of different beam splitters. Black solid line indicates different hyperfine states and momentum states of atoms. Horizontal direction represents atoms' momentum, and vertical direction represents atoms' energy. Dashed lines with different color represent different laser frequency. The frequency difference between the direct transition $F \to F'$ and the photon itself is Δ, and δ shows the frequency difference between two beams to satisfy the requirement of energy-momentum conservation for the transition. In a Raman transition, atoms in $F = 3$ state get transfer to a different hyperfine and momentum state. In Bragg diffraction, atoms in $F = 3$ state get transferred to the same hyperfine state $F = 3$ but different momentum state. In Bloch oscillations, atoms in this picture are transferred into the same final state as in Bragg diffraction case, but here the relative frequency δ is a function of time.

2.6.1 Bragg diffraction simulation

Here we will discuss the situation when there are two Bragg diffraction pulses happening together, as in our atom interferometer case. First of all, equations governing atoms in a single Bragg diffraction pulse are [35]

$$i\hbar\dot{g}(z,t) = \frac{\hat{p}^2}{2m}g(z,t) + \hbar\Omega_0\frac{e^{ikz}+e^{-ikz}}{2}e(z,t), \tag{2.82}$$

$$i\hbar\dot{e}(z,t) = \frac{\hat{p}^2}{2m}e(z,t) + \hbar\Omega_0\frac{e^{ikz}+e^{-ikz}}{2}g(z,t) - \hbar\Delta e(z,t), \tag{2.83}$$

where $g(z,t)$ is the ground state wave function of the atom, $e(z,t)$ is the excited state wave function, Ω_0 is the Rabi frequency of the laser, Δ is the single photon detuning, and $\hat{p}$ is the momentum operator. We assume the laser is far detuned from the single photon transition,

$\Delta \gg \omega_{\rm r}$, Ω_0. Working in the adiabatic approximation yields

$$0 \approx \hbar\Omega_0 \frac{e^{ikz}+e^{-ikz}}{2} g(z,t) - \hbar\Delta e(z,t), \tag{2.84}$$

$$e(z,t) \approx \frac{\Omega_0}{\Delta} \frac{e^{ikz}+e^{-ikz}}{2} g(z,t), \tag{2.85}$$

$$\begin{aligned} i\hbar\dot{g}(z,t) &\approx \frac{\hat{p}^2}{2m} g(z,t) + \hbar \frac{\Omega_0^2}{\Delta} \frac{e^{ikz}+e^{-ikz}}{2} \frac{e^{ikz}+e^{-ikz}}{2} g(z,t) \\ &= \frac{\hat{p}^2}{2m} g(z,t) + \hbar \frac{\Omega_0^2}{\Delta} \cos(kz)^2 g(z,t). \end{aligned} \tag{2.86}$$

Now we consider that there is a frequency difference δ between two counter-propagating beams as in the first two Bragg diffraction pulses. For the third and the fourth Bragg pulses, we replace the single frequency downwards-going beam with one pair of beams whose frequency differs from the original one as $\pm\delta_{\rm c}$. The equations for the third or fourth Bragg diffraction pulses then turn out to be

$$i\hbar\dot{g}(z,t) = \frac{\hat{p}^2}{2m} g(z,t) + \hbar\Omega_0 \frac{e^{ikz} + e^{-ikz-i(\delta+\delta_{\rm c})t} + e^{-ikz-i(\delta-\delta_{\rm c})t}}{2} e(z,t), \tag{2.87}$$

$$i\hbar\dot{e}(z,t) = \frac{\hat{p}^2}{2m} e(z,t) + \hbar\Omega_0 \frac{e^{-ikz} + e^{ikz+i(\delta+\delta_{\rm c})t} + e^{ikz+i(\delta-\delta_{\rm c})t}}{2} g(z,t) - \hbar\Delta e(z,t). \tag{2.88}$$

The laser frequency is about 3.52×10^{14} Hz here, and the wave number difference between different beams $\leq 10^5/10^{14}$, which is about 1 ppb. Therefore we assume that the three wave numbers are the same. However, the frequency differences δ and $\delta_{\rm c}$ are comparable to the recoil frequency and cannot be neglected. After the adiabatic assumption, the equation will be:

$$\begin{aligned} &i\hbar\dot{g}(z,t) \\ &= \left[\frac{\hat{p}^2}{2m} + \hbar \frac{\Omega_0^2}{\Delta} \frac{e^{-ikz} + e^{ikz+i(\delta+\delta_{\rm c})t} + e^{ikz+i(\delta-\delta_{\rm c})t}}{2} \frac{e^{ikz} + e^{-ikz-i(\delta+\delta_{\rm c})t} + e^{-ikz-i(\delta-\delta_{\rm c})t}}{2} \right] g(z,t). \end{aligned} \tag{2.89}$$

Using the Fourier transform of the space,

$$g(z,t) = \sum_{n=-\infty}^{\infty} g_n(t) e^{i2nkz}, \tag{2.90}$$

we can get

$$i\dot{g}_n = 4n^2\omega_{\rm r} g_n + \frac{\Omega_0^2}{4\Delta} \left[3g_n + 2\cos(2\delta_{\rm c}t) g_n + e^{-i\delta t} 2\cos(\delta_{\rm c}t) g_{n+1} + e^{i\delta t} 2\cos(\delta_{\rm c}t) g_{n-1} \right], \tag{2.91}$$

where the first two terms in the square brackets have the same effect for all momentum states: they shift the overall energy level but keep the relative energy difference the same. We can neglect them, which yields

$$i\dot{g}_n = 4n^2\omega_{\mathrm{r}}g_n + \frac{\Omega_0^2}{4\Delta}\left[2e^{-i\delta t}\cos(\delta_{\mathrm{c}}t)g_{n+1} + 2e^{i\delta t}\cos(\delta_{\mathrm{c}}t)g_{n-1}\right]. \tag{2.92}$$

For the first and the second Bragg diffraction pulses, we can just replace $2\cos(\delta_{\mathrm{c}}t)$ by 1, because this pulse contains only one frequency component in each laser beam. We then obtain

$$i\dot{g}_n = 4n^2\omega_{\mathrm{r}}g_n + \frac{\Omega_0^2}{4\Delta}(e^{-i\delta t}g_{n+1} + e^{i\delta t}g_{n-1}). \tag{2.93}$$

We can compare the calculation results between these two cases, as drawn in figure 2.6, here we assume that we are doing a n=4 (with 43μs half width) $\pi/2$ pulse.

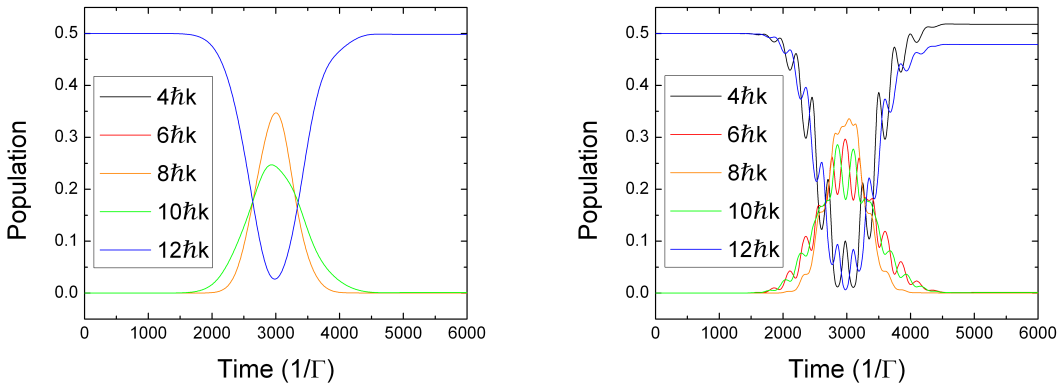

(a) Simulation of Bragg diffraciton with two frequency components (equation (2.93)).

(b) Simulation of Bragg diffraciton with three frequency components (equation (2.92)).

Figure 2.6: Simulations of Bragg diffraction with different frequency components. Here the x axis indicates the time coordinate with unit $1/\Gamma$, where Γ is the spontaneous decay rate of the excited state. The y axis indicates the population of different momentum state. The initial state is prepared as half of $4\hbar k$ and half of $12\hbar k$, in black and blue, respectively. These two states are in phase. Other color lines show the intermediate states, such as $6\hbar k$, $8\hbar k$, and $10\hbar k$, in the color of red, orange, and green, respectively. The laser pulse is not shown, but it is centered at 3000 in x axis, and its width is about 1000 $1/\Gamma$. The amplitude of the laser pulse is chosen as to make a $\pi/2$ pulse in figure 2.6a.

From the result of figure 2.6b, we notice that with an extra frequency δ_{c}, there are wiggles in the population versus time. The laser pulse conditions, like amplitude and pulse shape are the same for both cases, but the Bragg diffraction pulse with three frequency components has a different result compared with the two frequency components one. The asymmetry in

the population can be explained by combinations of two beam splitters in the third or the fourth pulses.

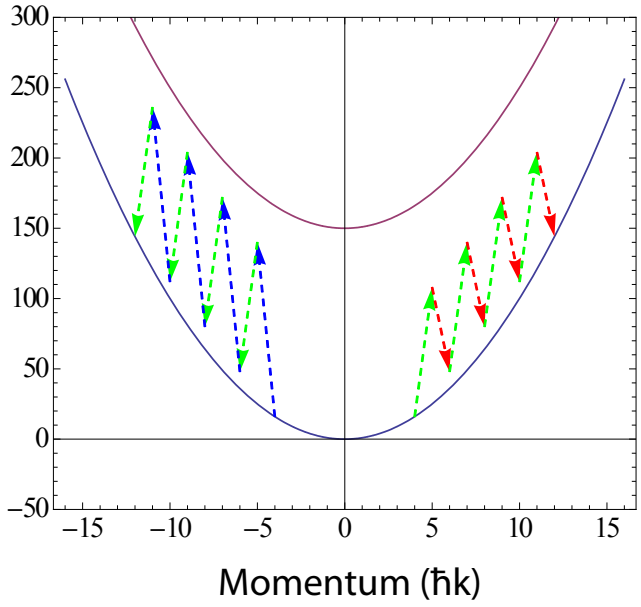

Figure 2.7: Frequency components at the third and fourth Bragg diffraction beam splitters. The y axis shows relative energy levels (not to scale), and the x axis shows the momentum in $\hbar k$ scale. We can see the parabola relation between energy and momentum. The blue and purple parabola lines indicate the energies of the ground state and excited state with different momentum, respectively. Green dashed arrows represent the frequency of the upward-going beam, and the red and blue dashed arrows represent the red detuned and blue detuned frequency of the downward-going beam, respectively.

In figure 2.7, which is the ideal case, the third or the fourth Bragg diffraction pulse just drives the population between $4\hbar k$ to $12\hbar k$ states for the top atom interferometer, and also between $-4\hbar k$ to $-12\hbar k$ states for the bottom atom interferometer. But the two beam splitters can talk to each other (i.e., generate extra transitions), making a population transfer between $4\hbar k$ and $-4\hbar k$. Some examples are drawn in figure 2.8. This causes a phase difference from the ideal case. We can verify the assumption by separating two beam splitters further in the momentum space and keeps the same Bragg diffraction condition. Instead of driving two atom clouds that are $8\hbar k$ away from each other, we can increase the momentum separation between them as $12\hbar k$, $16\hbar k$, an so on. The result is shown in figure 2.9, which indicates that increasing the momentum separation will decrease the phase deviation, as we expected.

We can calculate the relative phase in these $\pi/2$ beam splitters, as shown in figure 2.10. We can see that in a $\pi/2$ pulse case with only two frequency components, it does not matter

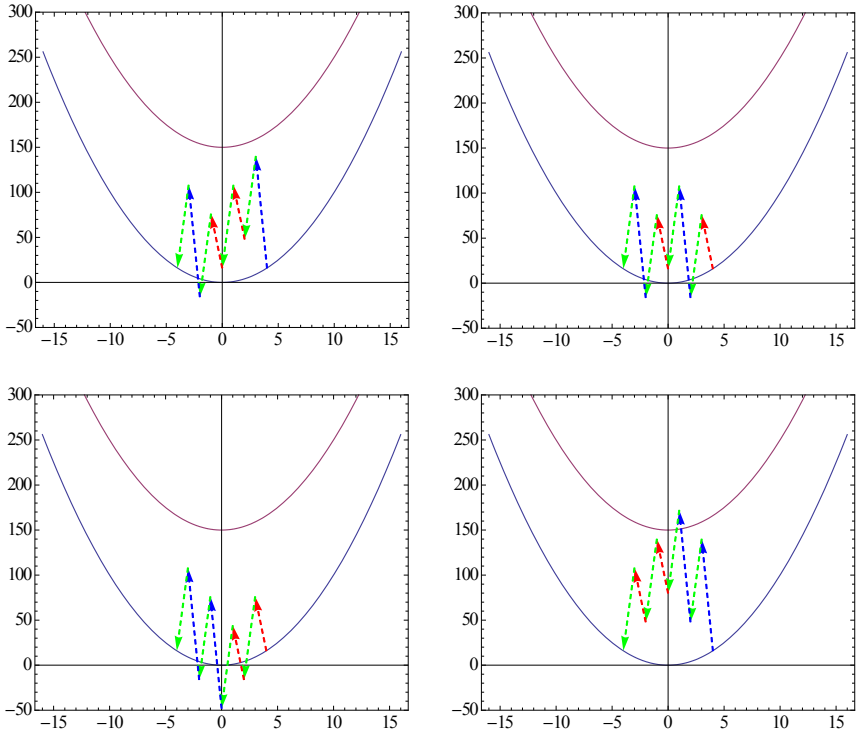

Figure 2.8: Some of possible ways of cross talks in Bragg diffraction beam splitters with more than two frequency components. The symbols are the same as in figure 2.7.

that atoms are initially in the $4\hbar k$ state or $12\hbar k$ state, in both cases the beam splitter will result in extra phase shift of $-\pi/2$, as predicted in section 2.3. However, in the three frequency components case, due to the frequency cross talk, both beam splitter conditions will not generate exactly $-\pi/2$ phase. When atoms are initially in $4\hbar k$, the relative phase is $-87.67°$, there is $2.33°$ difference in the phase. When atoms are initially in $12\hbar k$, the relative phase is $-92.23°$, and there is $-2.23°$ difference relative to an ideal beam splitter. Even though each of the beam splitter is no longer ideal, the sum of two phase differences is still very close to π, as we assume in figure 2.3, because the population still distributes into two outputs.

For conditions which differ from a perfect $\pi/2$ pulse, things are different. The reason that two beam splitters with different input port have an overall π phase difference after reflection is due to the conservation of atom numbers. For a Raman transition, this condition is satisfied almost perfectly. But for Bragg diffraction, the deviation of two-photon detuning δ or pulse amplitude from an ideal $\pi/2$ pulse condition will result in population distributing into more than two states, which yields a possible phase deviation from the ideal case.

Under the consideration of more realistic beam splitters, the two outputs from a beam splitter will be assigned to individual phases. We now write the population of output 1 as

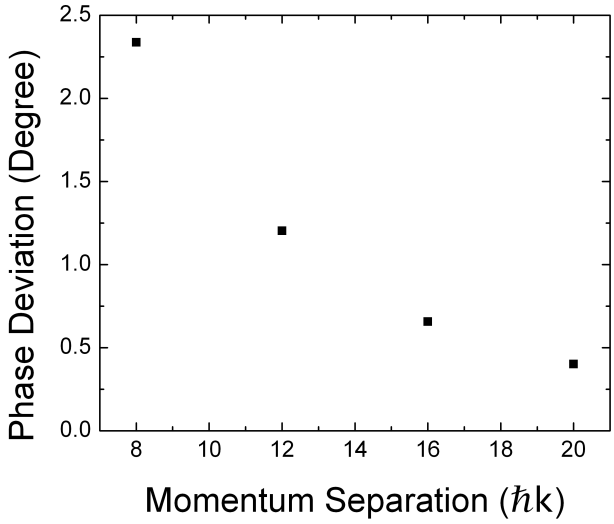

Figure 2.9: Calculated phase deviation at different momentum separation between the two atoms clouds at the third and fourth Bragg diffraction pulses. Instead of the separation, the conditions for Bragg diffraction keep the same. For an ideal case without the cross talk, the phase deviation should be zero.

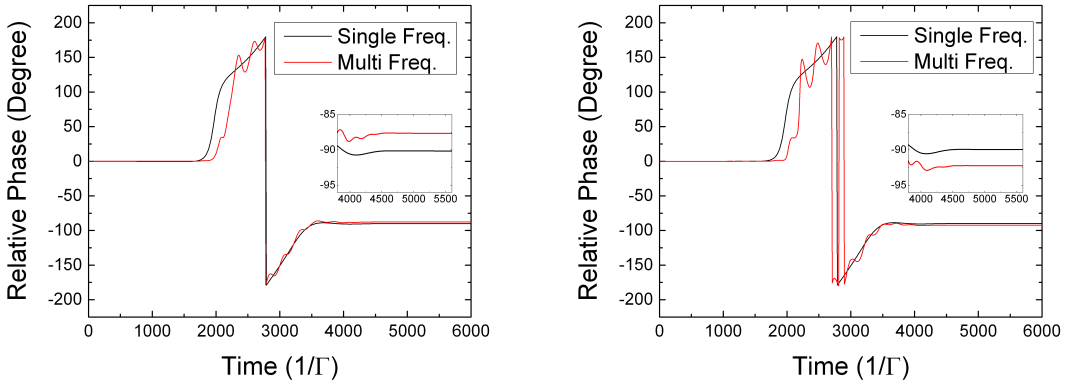

Figure 2.10: Comparison of phase calculation results in different beam splitter configurations. On the right hand side atoms are initially in $12\hbar k$ states before the Bragg diffraction pulse, the lines show relative phase from $4\hbar k$ to $12\hbar k$ state. On the left hand side atoms initially stay in $4\hbar k$ state before the Bragg diffraction pulse, the lines show relative phase from $12\hbar k$ to $4\hbar k$ state. Black line shows the case of the downward-going beam with single frequency component, red line shows the case with multi-frequency components. We add insets to magnify the phase difference at the end of the pulse.

$$
\begin{aligned}
&P_{\text{output 1}} \\
=&\frac{1}{2}\left[1+\cos\left(\Delta\Phi_{\text{laser}}+\Delta\Phi_{\text{free}}+\varphi_{0\to n}+\varphi_{n\to 0}+\varphi'_{-n\to -n}-\varphi_{0\to 0}-\varphi_{0\to 0}-\varphi'_{0\to 0}\right)\right]. \quad (2.94)
\end{aligned}
$$

Instead of $-3/2\pi-(-\pi/2)$, as in equation (2.19), we write it as $(\varphi_{0\to n}+\varphi_{n\to 0}+\varphi'_{0\to -n}+\varphi'_{-n\to -n})-(\varphi_{0\to 0}+\varphi_{0\to 0}+\varphi'_{0\to 0}+\varphi'_{0\to -n})$, where $\varphi_{i\to j}$ shows the phase shift when atoms move from the momentum $2i\hbar k$ state to the momentum $2j\hbar k$ state in the first two Bragg diffraction pulses. The phase coming from the last two Bragg diffraction pulses are represented by $\varphi'_{i\to j}$ with similar definitions.

For example, in $n=5$, $\pi/2$ pulse with 35 μs half width (as in our experiment), the phases are $\varphi_{0\to 0}\approx 80.02^\circ$, $\varphi_{0\to n}\approx -10.00^\circ$, $\varphi_{n\to 0}\approx -10.00^\circ$, and $\varphi_{n\to n}\approx -80.00^\circ$. Note the phase difference between $\varphi_{0\to 0}$, and $\varphi_{0\to n}$, in which atoms are initially in the $0\hbar k$ state, is about $-90.02^\circ\equiv\varphi_0\sim-\pi/2$, as we expect from a $\pi/2$ pulse, where the subscript 0 in φ_0 corresponds to the initial momentum state. In addition, the difference between φ_0 and φ_n is close to π, as expected from figure 2.3. For the last two Bragg diffraction pulses, the values of φ' are $\varphi'_{0\to -n}\approx -95.30^\circ$, $\varphi'_{0\to 0}\approx -8.54^\circ$, $\varphi'_{-n\to 0}\approx -95.30^\circ$, and $\varphi'_{-n\to -n}\approx -2.75^\circ$. Substituting these values into equation (2.94) leaves us

$$
\begin{aligned}
P_{\text{output 1}} &\approx \frac{1}{2}\left[1+\cos\left(\Delta\Phi_{\text{laser}}+\Delta\Phi_{\text{free}}-174.24^\circ\right)\right] \\
&= \frac{1}{2}\left[1-\cos\left(\Delta\Phi_{\text{laser}}+\Delta\Phi_{\text{free}}+5.76^\circ\right)\right]. \quad (2.95)
\end{aligned}
$$

Similarly, replacing $2\pi-0$ in the calculation of output 2 with $(\varphi_{0\to n}+\varphi_{n\to 0}+\varphi'_{0\to -n}+\varphi'_{-n\to 0})-(\varphi_{0\to 0}+\varphi_{0\to 0}+\varphi'_{0\to 0}+\varphi'_{0\to 0})$ yields

$$
P_{\text{output 2}}\approx\frac{1}{2}\left[1+\cos\left(\Delta\Phi_{\text{laser}}+\Delta\Phi_{\text{free}}+6.45^\circ\right)\right]. \quad (2.96)
$$

Taking the contrast from these two populations results in

$$
\begin{aligned}
&\frac{P_{\text{output 2}}-P_{\text{output 1}}}{P_{\text{output 2}}+P_{\text{output 1}}} \\
\approx&\cos\left\{5\left[\omega_{\text{m}}T-5\hbar\frac{(k_1+k_2)^2}{m}T\right]+6.11^\circ-10\frac{mgv_{\text{r}}}{\hbar}(T+T')T\right\}\cos 0.35^\circ \\
\approx&\cos\left[5\left(\omega_{\text{m}}T-40\omega_r T\right)+6.11^\circ-10\frac{mgv_{\text{r}}}{\hbar}(T+T')T\right] \\
=&\cos\left[5\left(\omega_{\text{m}}T-40\omega_r T+1.22^\circ\right)-10\frac{mgv_{\text{r}}}{\hbar}(T+T')T\right]. \quad (2.97)
\end{aligned}
$$

We can calculate similar things for the conjugate Ramsey-Bordé interferometer. Using $\varphi'_{n\to n}\approx -8.54^\circ$, $\varphi'_{n\to 2n}\approx -95.30^\circ$, $\varphi'_{2n\to 2n}\approx -2.75^\circ$, and $\varphi'_{2n\to n}\approx -95.30^\circ$, the populations and contrast are

$$
P_{\text{output 3}}\approx\frac{1}{2}\left[1-\cos\left(\Delta\Phi_{\text{laser,c}}+\Delta\Phi_{\text{free,c}}-6.50^\circ\right)\right], \quad (2.98)
$$

$$P_{\text{output 4}} \approx \frac{1}{2}\left[1+\cos\left(\Delta\Phi_{\text{laser,c}}+\Delta\Phi_{\text{free,c}}-5.81^\circ\right)\right], \tag{2.99}$$

$$\begin{aligned}
&\frac{P_{\text{output 4}}-P_{\text{output 3}}}{P_{\text{output 4}}+P_{\text{output 3}}}\\
\approx&\cos\left\{-5\left[\omega_{\text{m}}T-5\hbar\frac{(k_1+k_2)^2}{m}T\right]-6.16^\circ-10\frac{mgv_{\text{r}}}{\hbar}(T+T')T\right\}\cos 0.35^\circ\\
\approx&\cos\left[-5\left(\omega_{\text{m}}T-40\omega_r T+1.23^\circ\right)-10\frac{mgv_{\text{r}}}{\hbar}(T+T')T\right].
\end{aligned} \tag{2.100}$$

When combining these results with ellipse fitting, the measured frequency ω_{m} now is

$$\omega_{\text{m}} \approx 40\omega_{\text{r}} - \frac{1.23^\circ}{T}. \tag{2.101}$$

Compared with equation (2.50), ω_{m} now will vary at different time separation T. This deviation comes only from the extra transition between $-10\hbar k$ and $0\hbar k$ at the final two Bragg diffraction pulses.

For non-ideal $\pi/2$ pulses, extra effects should also be expected. We can write a more general equation as

$$\omega_{\text{m}} \approx 8n\omega_{\text{r}} - \frac{\delta\phi_{\text{cross}}+\delta\phi_{\text{non-ideal}}}{T}, \tag{2.102}$$

where $\delta\phi_{\text{cross}}$ is the deviation comes from the cross talk, and $\delta\phi_{\text{non-ideal}}$ is the deviation comes from the non-ideal $\pi/2$ beam splitter pulse. For $n = 4$ and $n = 6$ case, the cross talk term $\delta\phi_{\text{cross}}$ with the same pulse width is about 0.75° and 1.47°, respectively. The result of $\delta\phi_{\text{non-ideal}}$ with different intensity and two-photon detuning in Bragg diffraction (with the same 35 μs half width) are shown in figure 2.11 and figure 2.12, respectively. It shows the requirement of a perfect $\pi/2$ pulse will not only generate the best contrast, but also minimize the unwanted phase deviation.

2.7 Compton clock

2.7.1 Classical view

In the rest frame of atoms, the Bragg diffraction pulse makes atoms transfer from $0\hbar k$ to $2n\hbar k$ momentum state with two-photon frequency difference ω_{b} such that

$$n\hbar\omega_{\text{b}} = \frac{4n^2\hbar^2k^2}{2m}, \tag{2.103}$$

$$\omega_{\text{b}} = 4n\omega_{\text{r}} = \frac{2n\hbar k^2}{m} = \frac{2n\hbar}{m}\left(\frac{\omega_{\text{L}}}{c}\right)^2 = \frac{2n\hbar}{mc^2}\omega_{\text{L}}^2 = 2n\frac{\omega_{\text{L}}^2}{\omega_0}, \tag{2.104}$$

where ω_{L} is the angular laser frequency.

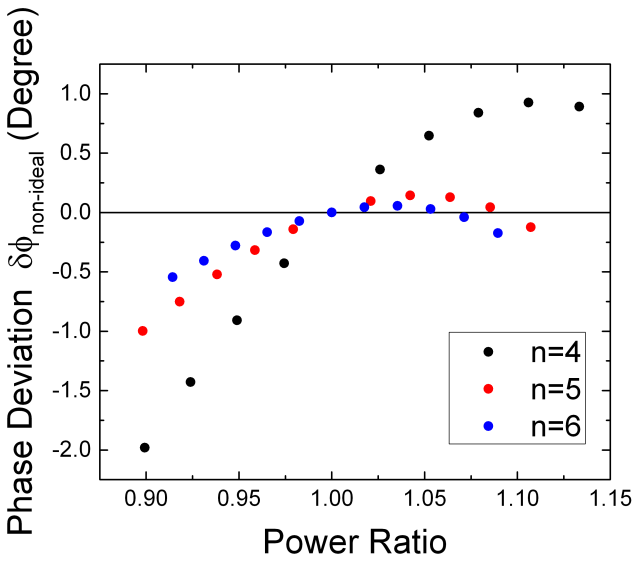

Figure 2.11: Phase deviation $\delta\phi_{\text{non-ideal}}$ under different pulse amplitudes and Bragg order n. The x axis shows the power ratio between this pulse and a perfect $\pi/2$ Bragg diffraction pulse.

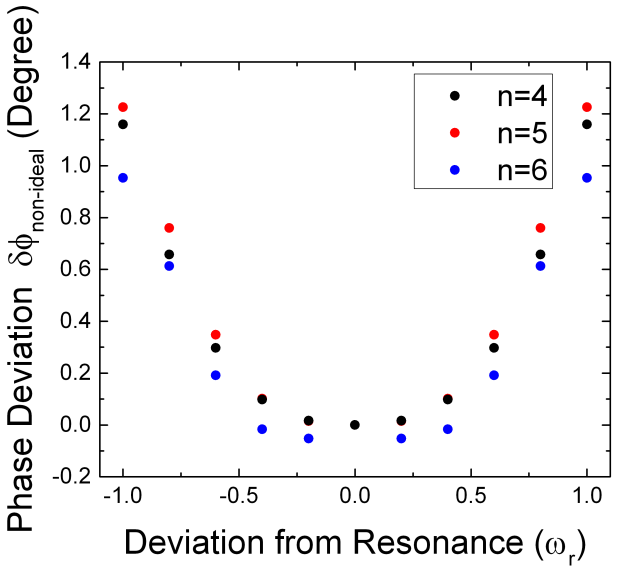

Figure 2.12: Phase deviation $\delta\phi_{\text{non-ideal}}$ under different two-photon detuning and Bragg order n.

As discussed in section 1.3.2, when we realize a Compton clock, the angular laser frequency ω_{L} is set to a certain ratio of the recoil frequency ω_{r},

$$\omega_{\text{L}} \equiv 8nN\omega_{\text{r}} = 2N\omega_{\text{b}}, \tag{2.105}$$

	ω_0	ω_b	ω_r	ω_L
ω_0	1	$8nN^2$	$32n^2N^2$	$4nN$
ω_b	$1/8nN^2$	1	$4n$	$1/2N$
ω_r	$1/32n^2N^2$	$1/4n$	1	$1/8nN$
ω_L	$1/4nN$	$2N$	$8nN$	1

Table 2.1: Relationship between the Compton frequency ω_0, the Bragg diffraction frequency ω_b, the recoil frequency ω_r, and the angular laser frequency ω_L. The table shows the relation $\omega_i = A_{ij}\omega_j$, where ω_i is the ith left column component, ω_j is the jth top row component, and A_{ij} is the corresponding table component.

where N is a fixed value. When this conditions holds, the measured frequency will be

$$\omega_\mathrm{m} = 2\omega_\mathrm{b} = \frac{\omega_0}{4nN^2}, \tag{2.106}$$

which directly links to the Compton frequency ω_0, as what we want. The relation between these different frequencies is tabulated in table 2.1.

2.7.2 Relativistic view

In the semiclassical limit, the Feynman path integral shows that a particle is well described by a wave packet ψ that closely follows the equivalent classical trajectory, whose phase evolves between two space-time events (x,t) and (x', t') according to

$$\psi(x', t') = \psi(x, t)e^{i\Phi_\mathrm{free}}, \tag{2.107}$$

where the relativistic expression for the phase $\Phi_\mathrm{free} = \omega_0\tau$ is simply the Compton frequency multiplied by the proper time τ, defined as the time measured by a clock that moves along with the wave packet.

To obtain simple yet exact expressions for our interferometer phase relativistically, we assume the atom interferometer is in a free falling frame. We start the analysis in a frame of reference in which the output velocities of the beam splitter are equal and opposite, as shown in figure 2.13a, given by $\pm v \equiv \pm\beta c$. The Bragg diffraction resonance condition, or equivalently energy-momentum conservation, requires $m\gamma v = n\hbar k$. Simple algebra shows

$$\beta\gamma = \frac{n\omega_\mathrm{L}}{\omega_0}, \tag{2.108}$$

where $\gamma = 1/(1-\beta^2)^{1/2}$ is the Lorentz factor. We then express the same process in the initial rest frame of the atom, as in figure 2.13b: using the Doppler formula, we express the angular laser frequencies in this frame as

$$\omega_\pm = \omega_\mathrm{L}\left(\frac{1 \pm \beta}{1 \mp \beta}\right)^{1/2}. \tag{2.109}$$

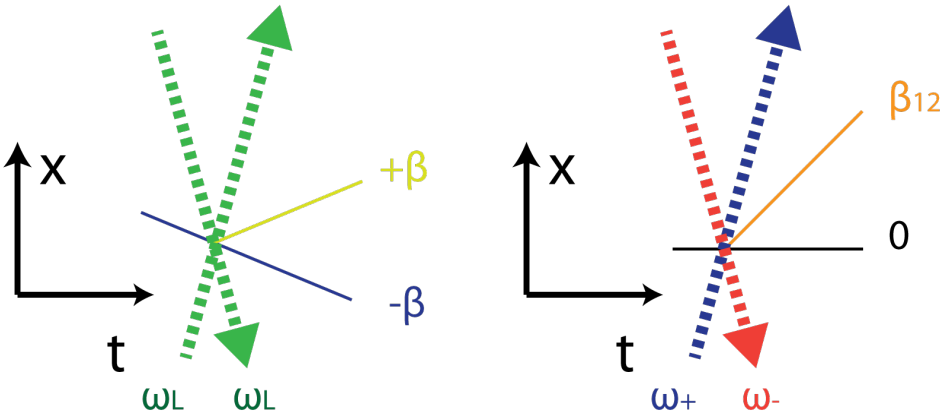

(a) Symmetric frame

(b) Initial rest frame

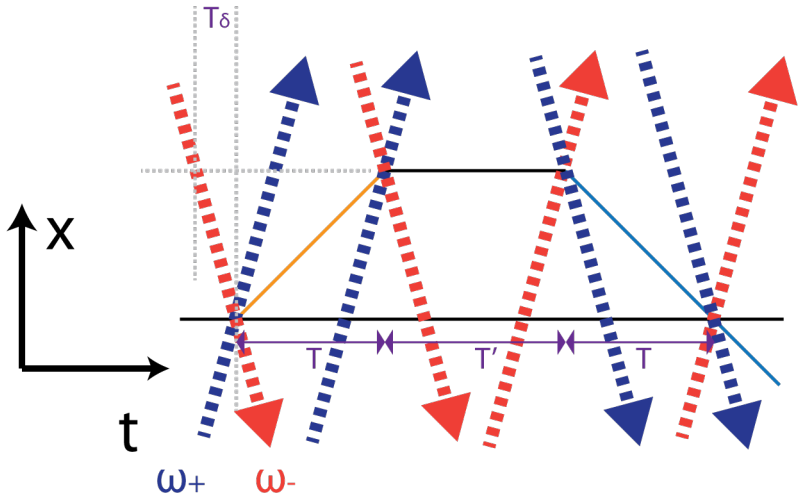

(c) Interferometer

Figure 2.13: Interferometer in a free falling frame. One single beam splitter plotted in the "symmetric" frame of reference is shown in a, and the initial rest frame is shown in b. In c, the black, orange and blue lines are the paths of the matter waves versus time; red and dark blue dashed arrows denote laser beams. Additional paths that do not interfere are not shown.

The velocity addition formula yields the moving atom's velocity $\beta_{12} = 2\beta/(1+\beta^2)$.

The atom interferometer sequence, as shown in figure 2.13c, starts with a beam splitter

based on Bragg diffraction with a pulse of counter-propagating laser beams. After a delay time T, the laser beams are pulsed again, this time bringing the wavepackets to relative rest. Two more flashes of counter-propagating laser pulses with the frequencies $\omega_\pm$ interchanged return the wave packets together to produce interference at the time of the final pulse. The free evolution phase therefore is

$$\Delta\Phi_{\text{free}} = -2T\omega_0\left(1-\frac{1}{\gamma_{12}}\right) = -4\omega_0 T\frac{\beta^2}{1+\beta^2}, \tag{2.110}$$

where the Lorentz factor $\gamma_{12} = 1/(1-\beta_{12}^2)^{1/2} = (1+\beta^2)/(1-\beta^2)$. Note $\Delta\Phi_{\text{free}} \approx -2(K.E.)T/\hbar$ in the nonrelativistic limit, but $\Delta\Phi_{\text{free}} \approx -2T\omega_0$ if $v_{12} \to c$.

The atom-light interaction phase is derived as follows: laser beams travel on null geodesics and each photon carries the phase of the laser oscillator at the time of emission. The effect of the atom's location on the laser phase comes in through the propagation delay. The propagation delay of a laser beam between the upper and lower trajectory satisfies $T_\delta = \beta_{12}T = 2\beta T/(1+\beta^2)$. The oscillation frequencies of the laser are indicated in figure 2.13b. It is understood that the laser phase keeps advancing at these constant frequencies $\omega_\pm$ between the pulse intervals, with frequencies switched during the interval T'. Summing up the phases at the times the laser beams are emitted, with the appropriate sign (plus for absorption, minus for stimulated emission, as in section 2.3.1), yields

$$\begin{aligned}\Delta\Phi_{\text{laser}} =& n\left[\omega_-(T+T_\delta)+\omega_+(T+T'-2T-T'+T_\delta)\right] \\ &+ n\left[\omega_+(0-T+T_\delta)+\omega_-(-T-T'+T_\delta+2T+T')\right].\end{aligned} \tag{2.111}$$

We allow for small deviations of the laser frequencies from these nominal values by substituting $\omega_\pm$ with $(1\pm\varepsilon)\omega_\pm$, where $|\varepsilon \ll 1|$. Since $\omega_+ + \omega_- = 2\gamma(1+\beta\varepsilon)\omega_{\text{L}}$, and $\omega_+ - \omega_- = 2(\beta+\varepsilon)\gamma\omega_{\text{L}}$, substitution for ω_+, ω_-, and T_δ yields

$$\Delta\Phi_{\text{laser}} = 4n\omega_{\text{L}}T\frac{\beta-\varepsilon}{\gamma(1+\beta^2)}, \tag{2.112}$$

which with equation (2.108) turns out to be

$$\Delta\Phi_{\text{laser}} = 4\omega_0 T\frac{\beta^2}{1+\beta^2} - 4\varepsilon\omega_0 T\frac{\beta}{1+\beta^2} + O(\varepsilon^2). \tag{2.113}$$

The notation $O(\varepsilon^2)$ denotes small terms proportional to ε^2 and higher powers. If $\varepsilon \neq 0$, the Bragg resonance condition given by equation (2.108) or (2.109) is not strictly satisfied. If ε is small, however, this has negligible consequences. The $\Delta\Phi_{\text{laser}}$ cancels $\Delta\Phi_{\text{free}}$ if, and only if equation (2.108) holds and

$$\omega_{\text{b}} = \omega_+ - \omega_- = 2\omega_0\frac{\beta^2}{n(1-\beta^2)} = 2\omega_0\frac{\beta^2\gamma^2}{n} = 2n\frac{\omega_{\text{L}}^2}{\omega_0}. \tag{2.114}$$

This result agrees exactly with the nonrelativistic derivation equation (2.104) and with equation (2.50). Moreover,

$$\omega_{\mathrm{L}} = 2N\omega_{\mathrm{b}} = 4N\omega_{\mathrm{L}}\frac{n\omega_{\mathrm{L}}}{\omega_0} = 4N\beta\gamma\omega_{\mathrm{L}}, \tag{2.115}$$

which shows $4N\beta\gamma = 1$ ($n\omega_{\mathrm{L}}/\omega_0 = \beta\gamma$ from equation (2.108)). The particle's velocity (and, thus, the time dilation factor) is therefore given exactly by the frequency multiplication factor N.

2.8 Coriolis force effect

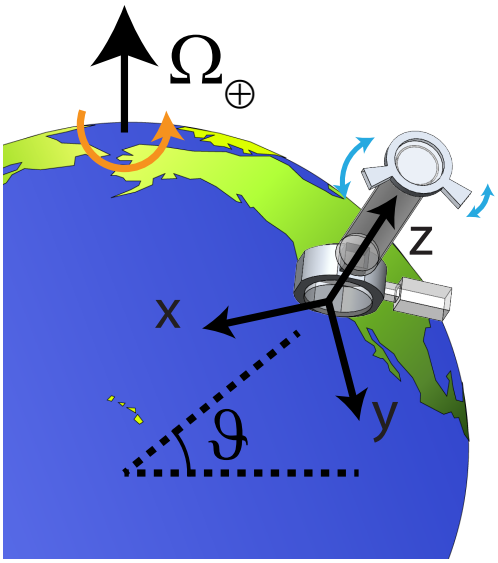

Figure 2.14: Cartoon picture of our experimental setup on rotating Earth. The three axes we used in calculating the Coriolis force are shown in the picture, in which x is pointing west, y is pointing south and z is vertical direction. The two blue arrows on the top of the chamber shows the movements of our top mirror to compensate the Coriolis force, as discussed in section 3.11. Earth rotates at rate $\Omega_{\oplus}$, and our experiment is at latitude ϑ.

Our experiment is on Earth, as shown in figure 2.14, being affected by its gravity and rotation. The cancellation of gravity is discussed in section 2.2 by conjugate Ramsey-Bordé interferometers. Here we will discuss the effects of the Coriolis force. The Coriolis force due to the Earth rotation has the form

$$\vec{F} = -2m\vec{\Omega}_{\oplus} \times \vec{v}, \tag{2.116}$$

where $\vec{v}$ is the velocity of the object, and $\Omega_{\oplus}$ is the Earth rotation rate. In the atom interferometer, atoms with different velocity will be subjected to different forces. Because of

this, the interferometer does not close precisely. To model this, we first assume the initial wavepacket ψ has the form of

$$\psi = \left(\frac{\det A}{\pi^3}\right)^{1/4} e^{-(1/2)\vec{x}A\vec{x}}, \tag{2.117}$$

where A is the matrix which is diagonal with elements σ_1^{-2}, σ_2^{-2}, and σ_3^{-2} [36]. An estimation of the size of the atomic wave packets is provided by the thermal de Broglie wavelength, which in our experimental case with temperature 2 μK is about 100 nm. The overlap integral is independent of time,

$$\int d^3r \psi^*(\vec{r}+\vec{\delta})\psi(\vec{r}) = e^{-(1/4)\vec{\delta}A\vec{\delta}}, \tag{2.118}$$

where $\vec{\delta}$ is the mismatch of wave packets.

We adopt Cartesian coordinates in an inertial frame, one that does not rotate with Earth, to calculate $\vec{\delta}$. We define the z axis such that the laser points vertically upwards along it at T_1. We take the x axis horizontal pointing west and the y axis pointing south. Later, at $T_2 = T_1 + T$, $T_3 = T_1 + T + T'$, and $T_4 = T_1 + 2T + T'$, mirrors rotate relative to the inertial frame and change the direction of the momentum being transferred. As a result, the wave packet's relative velocities during the intervals $[T_1, T_2]$, $[T_2, T_3]$, $[T_3, T_4]$, and $[T_4, T_\infty]$ are

$$v_{12} = 2nv_{\mathrm{r}}(0, 0, 1), \tag{2.119}$$

$$v_{23} = 2nv_{\mathrm{r}}(\Omega_\oplus T\cos\vartheta, 0, 0), \tag{2.120}$$

$$v_{34} = 2nv_{\mathrm{r}}(\Omega_\oplus(2T + T')\cos\vartheta, 0, -1), \tag{2.121}$$

$$v_{4\infty} = 0, \tag{2.122}$$

where $\vartheta = 37.87°$ is the latitude of our laboratory in Berkeley, California. Thus, at T_4, the wave packets miss each other by

$$\vec{\delta} = 4nv_{\mathrm{r}}\Omega_\oplus T(T + T')\cos\vartheta(1, 0, 0). \tag{2.123}$$

The value of mismatch is comparable to the wave packet size when the Bragg order $n = 5$ and the time separation $T > 100$ ms. From the value of $\vec{\delta}$ and equation (2.118), we can estimate the contrast lost due to Coriolis force. The result is compared with experimental data in section 4.1.

2.9 Phase from the gravity gradient

When we improve the overall contrast by conjugate Ramsey-Bordé interferometers and compensating the Coriolis force (section 3.11), we can achieve higher contrast at longer time separation and therefore better sensitivity. The gravity gradient term cannot be neglected

anymore with a longer time separation. For the gravity gradient, we need to know the relation between its value and the phase we measure. To do this we replace the zero order Taylor expansion on gravity to the first order as $g(x) \approx g - \gamma x$. Therefore, the gravitational potential $V(x) = mgx$ will be replaced by $V(x) = mgx - m\gamma x^2/2$. We can treat it as a perturbation and then calculate the phase for original Ramsey-Bordé interferometer. Again assume the atom's trajectory is affected only by the constant gravitational field, as in section 2.4, then the free evolution phase becomes

$$\frac{4n^2 m v_{\mathrm{r}}^2 T}{\hbar}\left[1+\frac{\gamma}{6}\left(2T^2+3TT'\right)\right]-\frac{nmv_{\mathrm{r}}Tg\gamma}{6\hbar}\left(7T^3+14T^2T'+9TT'^2+2T'^3\right). \tag{2.124}$$

Adding $\Delta\Phi_{\mathrm{laser}}$ from equation (2.45) yields

$$\begin{aligned} &nT\left\{\omega_{\mathrm{m}}-\frac{4nmv_{\mathrm{r}}^2}{\hbar}\left[1-\frac{\gamma}{6}\left(2T^2+3TT'\right)\right]\right\} \\ &-nT\left[\frac{2mgv_{\mathrm{r}}}{\hbar}(T+T')+\frac{mgv_{\mathrm{r}}\gamma}{6\hbar}\left(7T^3+14T^2T'+9TT'^2+2T'^3\right)\right]. \end{aligned} \tag{2.125}$$

The other conjugate Ramsey-Bordé interferometer gives the free evolution phase as

$$-\frac{4n^2 m v_{\mathrm{r}}^2 T}{\hbar}\left[1-\frac{\gamma}{6}\left(4T^2+6TT'+3T'^2\right)\right]-\frac{nmv_{\mathrm{r}}Tg\gamma}{6\hbar}\left(7T^3+14T^2T'+9TT'^2+2T'^3\right). \tag{2.126}$$

Similarly, combining this with $\Delta\Phi_{\mathrm{laser,c}}$ yields

$$\begin{aligned} &-nT\left\{\omega_{\mathrm{m}}-\frac{4nmv_{\mathrm{r}}^2}{\hbar}\left[1+\frac{\gamma}{6}\left(4T^2+6TT'+3T'^2\right)\right]\right\} \\ &-nT\left[\frac{2mgv_{\mathrm{r}}}{\hbar}(T+T')+\frac{mgv_{\mathrm{r}}\gamma}{6\hbar}\left(7T^3+14T^2T'+9TT'^2+2T'^3\right)\right]. \end{aligned} \tag{2.127}$$

Combing these two fringes into an ellipse, which yields a differential phase of

$$\phi_{\mathrm{d}} = nT\left\{\omega_{\mathrm{m}}-8n\omega_{\mathrm{r}}\left[1+\frac{\gamma}{12}\left(2T^2+3TT'+3T'^2\right)\right]\right\}. \tag{2.128}$$

From this equation we can correct the measured frequency with a known gravity gradient to first order.

Chapter 3

Experimental Setup

3.1 Overview

Here we give an overview of our atom interferometer (AI). Details are mentioned in the following sections. The overall experimental sketch is shown in figure 3.1. Our experimental setup is on two optical tables. The titanium-sapphire table contains our reference laser system used to offer the overall frequency reference to our experiment. There are also titanium-sapphire lasers which are locked to the reference laser and used to prepare atoms into proper states and make beam splitters. The other optical table is the magneto-optical trap (MOT) table. On this table is our fountain and cooling systems to launch and cool atoms. Atom interferometry happens in the vacuum chamber, which stands on the MOT table.

The overall time sequence summary is shown in figure 3.2. For preparing atoms, at first a MOT is used to trap ^{133}Cs using the D2 line in a vacuum chamber [37]. Atoms in the MOT are then cooled down by polarization gradient cooling [38] and launched vertically with a flux of $\sim 10^9$ atoms per second with temperature ≈ 1.2 μK, which we call the atomic fountain. The vacuum chamber sketch and is shown in figure 3.3. It is 3 meters high and the cylindrical chamber where the interferometry takes place is about is about 1.5 meters long. On the top there is a ion pump to maintain the vacuum pressure below 10^{-9} torr. The atomic fountain allows us to double the distance the atoms travel given a fixed vacuum chamber size. This also allows us to have a smaller setup and make optical alignment easier.

After launch, we need to select out atoms with desirable properties. We prefer the atoms to be in a state which is insensitive to external magnetic fields, so as to reduce systematic errors. We also favor the atoms in a narrow momentum distribution so that all beam splitters can have the same optimized efficiency and result in the largest contrast and optimal signal to noise ratio. For selecting such atoms, one velocity-insensitive Raman transition is used to select the right Zeeman state ($m_{\mathrm{F}} = 0$). For a Raman transition, laser beams whose frequencies will differ by the hyperfine state splitting. These beams enter the bottom of the vacuum chamber, and are reflected upwards, as shown in figure 3.3. After selection, we then

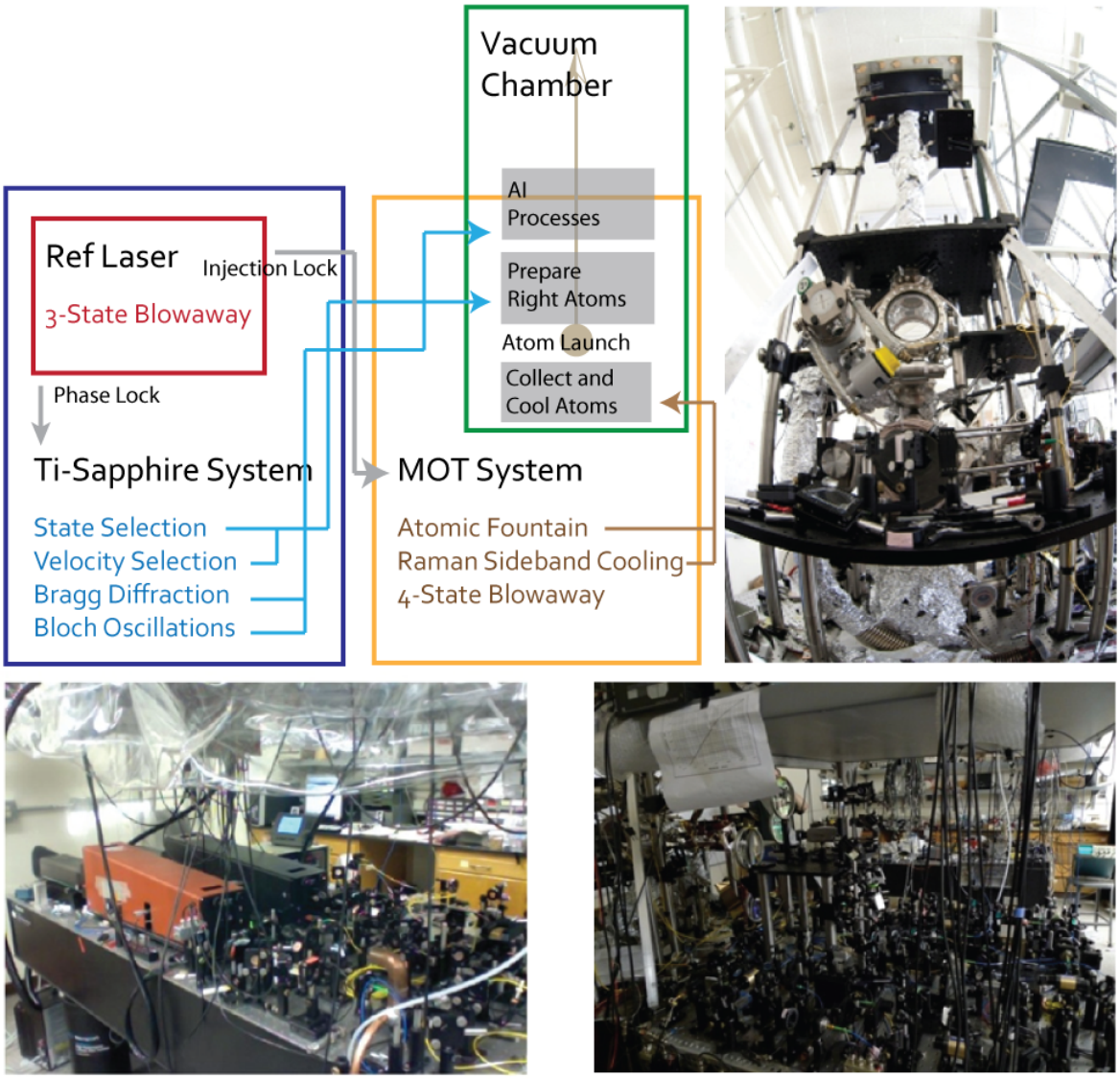

Figure 3.1: Experimental setup overview. Bottom left picture is our titanium-sapphire table. Bottom right picture is our MOT table. Top right picture is our vacuum chamber.

blow away all remaining unwanted atoms by a strong laser beam with a cycling transition. Even though atoms now are in the desired Zeeman state, they are still in a broad momentum distribution which is too large for our beam splitter. We again use another Raman transition, this time a velocity-sensitive one, to select atoms with the desired velocity distribution in the vertical direction. For the velocity-sensitive configuration, the upward laser beam is retro-reflected back by a top mirror, which therefore generates a pair of counter-propagating beams. Atoms with different velocity will see different frequencies for both beams and only

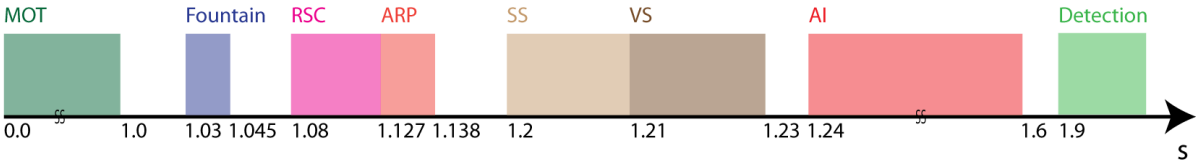

Figure 3.2: Experimental time sequence overview. Each experimental cycle is 2.1 seconds long. The abbreviation RSC stands for Raman sideband cooling, ARP stands for adiabatic rapid passage, SS stands for state selection, and VS stands for velocity selection.

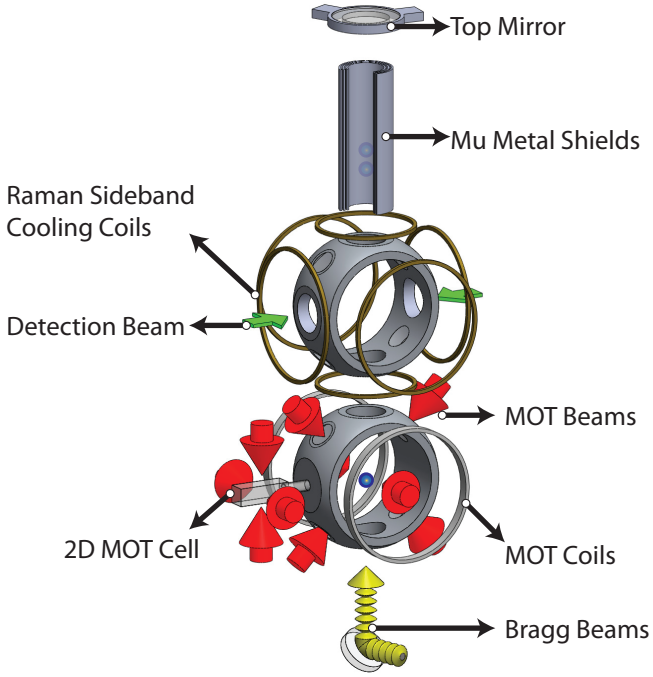

Figure 3.3: Experimental vacuum chamber sketch.

in a certain range of velocity will the beams drive the transition.

After these preparations, the number of atoms remaining is approximately $\sim 10^6$, and the effective temperature along the vertical direction is about hundreds of nK. We use Bragg diffraction as the beam splitters to achieve sufficient momentum separations and therefore high sensitivity. The laser that drives Bragg diffraction shares the same path as the Raman transition beams and separates atoms into different momentum states. The atoms fall back at different times and can be detected by a photomultiplier (PMT) using fluorescence detection. Signals from different branches of the atom interferometer are combined together by ellipse

fitting to get rid of the common mode phase, which changes due to vibrations, to increase the overall contrast. The Coriolis force also get compensated by rotating the top mirror to achieve longer time separation. From the relative phase between the two fringes and the knowledge of our laser frequency we can obtain the recoil frequency. By feeding back the recoil frequency measurement to the optical frequency comb, our lasers can be locked to a certain ratio of the recoil frequency, realizing a Compton clock. The fine structure constant value can also be obtained from this measurement.

We further improve the setup by implementing Raman sideband cooling after launch to cool the atoms down to < 500 nK [39]. After Raman sideband cooling, the atoms are in the $m_{\mathrm{F}} = 3$ state, which is sensitive to external magnetic fields. We apply adiabatic rapid passage using a microwave frequency antenna to transfer atoms from $m_{\mathrm{F}} = 3$ to $m_{\mathrm{F}} = 0$ state and also a velocity-insensitive Raman transition to purify the atoms further. We also update the beam splitter sequence by adding Bloch oscillations between Bragg diffraction to increase the overall momentum separations.

3.2 Reference laser

Our reference laser, which locks to a D2 line of ^{133}Cs, is used to offer a frequency reference for all of our experimental lasers. The overall frequency components sketch is shown in figure 3.4. The reference laser (Newfocus TLB-6917 Vortex II Tunable Laser) has a linewidth of about 300 kHz. The experimental setup is shown in figure 3.6 and 3.7. After going through the double-passed 141 MHz acousto-optic modulator (AOM) 1 and being fiber coupled, the beam passes AOM4. The zero order of the beam passes through an electro-optic modulator (EOM), which is operated at 11 MHz and generates two sidebands. The minus-first order beam through AOM4 carries no sidebands. These two beams pass through a cesium cell with a magnetic shield in opposite directions.

Signals of the zero order beam after passing through the cesium cell is detected and used for frequency modulation saturation spectroscopy [40]. The overall frequency shift is therefore 2.5×141 MHz $= 352.5$ MHz. The reference signal is locked to $F = 3 \rightarrow F' = 2$ state, and the laser frequency is close to the $F = 3 \rightarrow F' = 4$ state. This signal has a good signal to noise ratio (SNR) but with a related Doppler background.

The other signal we detect is for phase modulation transfer spectroscopy [41], which can be described as kind of four-wave mixing. In this four-wave mixing, the minus-first order beam and the frequency components of the zero order beam generate the fourth photon along the direction of the minus-first order beam, which is detected by a diode and demodulated at 11 MHz. The signals are free of the Doppler background, but have worse SNR. In order to take advantage of both signals, the output electronic signals are combined from both detectors. The frequency modulation signals are connected to a capacitor first and corresponding to fast responses. The four-wave mixing signals are connected to a resistor first and correspond to long term drift responses. For stabilizing the diode frequency, the

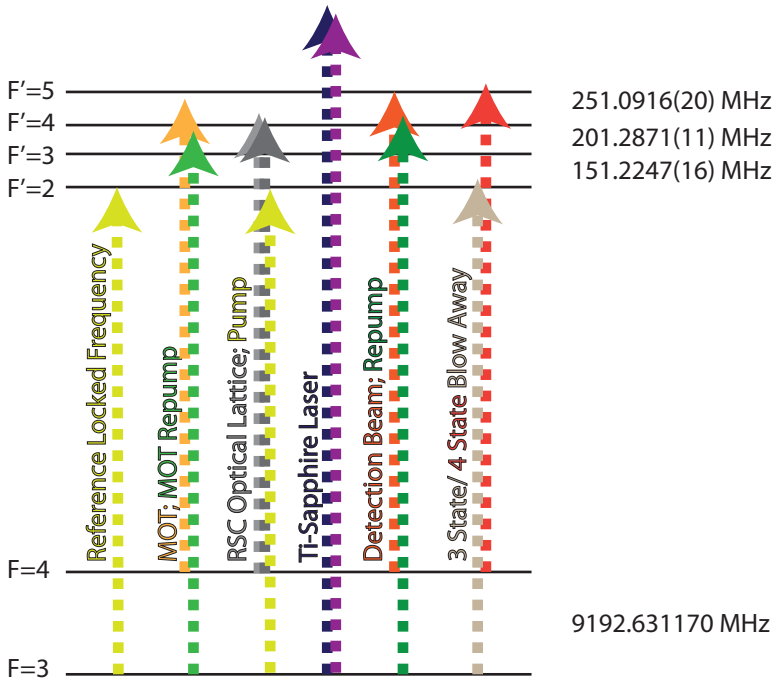

Figure 3.4: Experimental frequency components sketch.

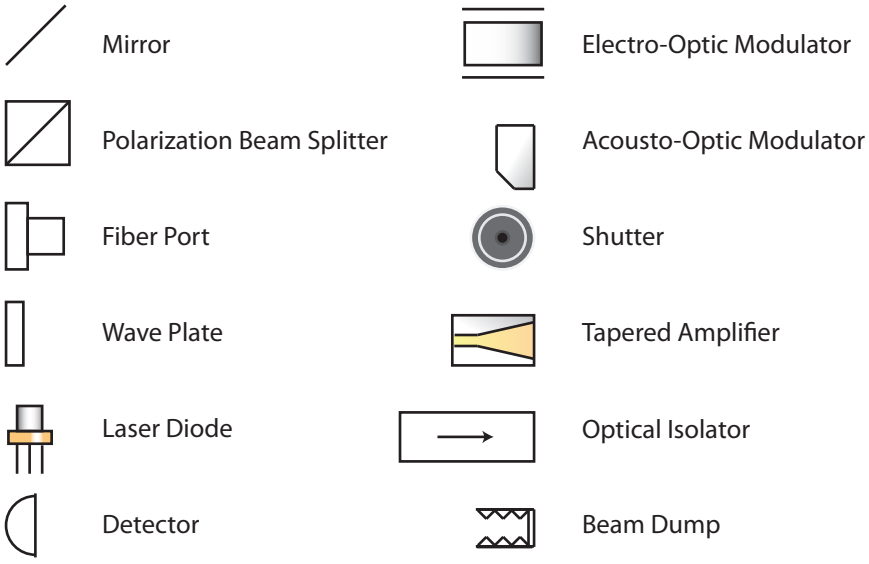

Figure 3.5: Symbols and the corresponding components in experimental sketches.

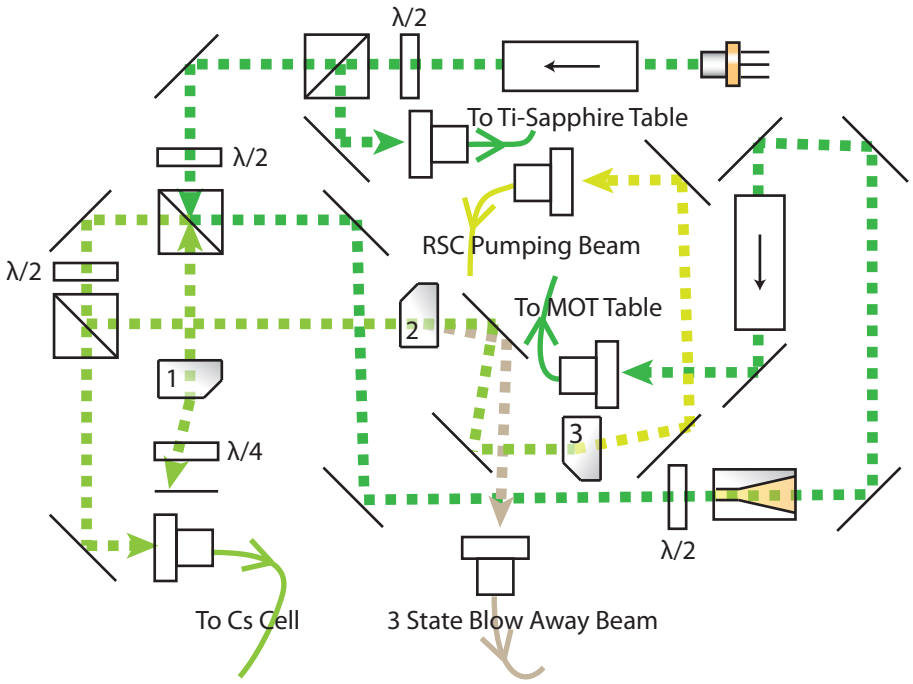

Figure 3.6: Experimental setup on reference table I, as shown in figure 3.1. The frequency details for the reference laser are shown in figure 3.9a. Light with different frequencies are shown in dashed line with different colors. Refer to figure 3.5 for the meaning of symbols in all experimental sketches in this chapter. For simplicity, in all sketches we assume that all fiber-coupled light is polarization-maintained.

fast error signal response feeds back to the diode current and the slow error signal response feeds back to a piezoelectric actuator of the laser diode.

In addition to the spectroscopy, the 3 state blow away beam (section 3.8), the MOT repumping beam (section 3.4), and the Raman sideband cooling pumping beam (section 3.13) are also derived from the reference laser, as shown in figure 3.6. To supply enough power for the derived beams, the light passes through a Sacher Lasertechnik tapered amplifier running at 1.25 Amp, with 4 mW seeding power and 150 mW output power. Details about these are discussed in later sections.

3.3 Time sequence generation

The spectroscopy does not need to switch light frequencies and paths. Things are different for atom preparations and atom interferometry. Our time sequence is controlled by National Instrument PCI-6534 and PCI-DIO-32HS cards. PCI-6534 includes 32 individual channels with external reference connected to a 10 MHz signal. Each channel can be controlled by computer programs and generate 5 V TTL signals. The card has a 20 MHz maximum clock

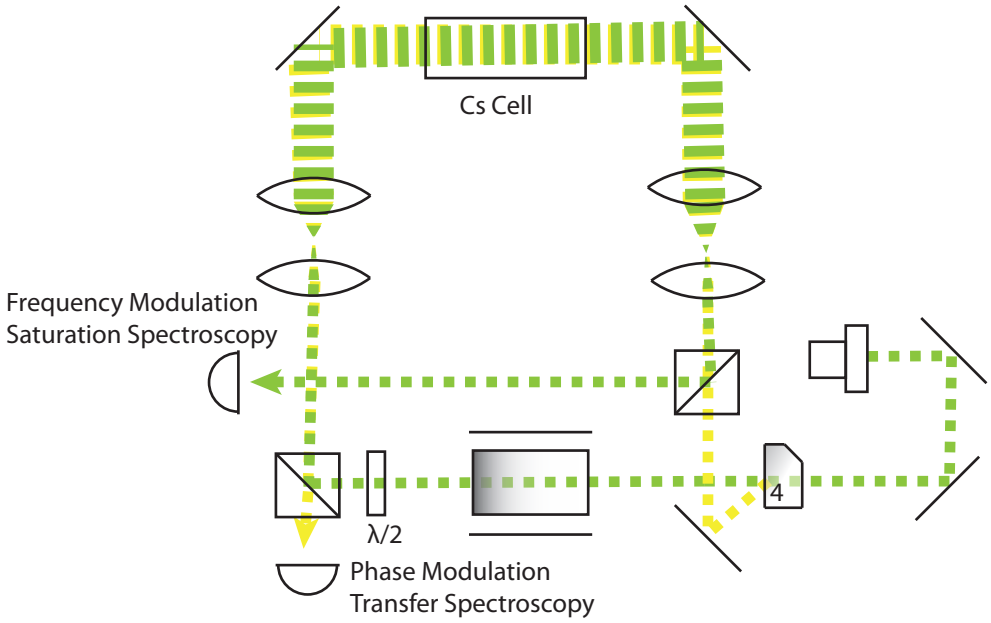

Figure 3.7: Experiment setup on reference table II. Reference laser comes from the fiber coupling in reference table I. The frequency details are also shown in figure 3.9a

rate and 323 MB of on board memory. PCI-DIO-32HS is similar to PCI-6534, but has no internal cache, and is required to load data from a computer. Therefore PCI-DIO-32HS is triggered by PCI-6534, which runs in its own time base to minimize perturbations from the computer and to allow the better synchronization. The time resolution for the card is about 1 μs, which does not have enough accuracy for determining time separations between beam splitter pulses. We use Stanford Research Systems Model DG 535 delay generators to generate trigger signals for the beam splitter pulses, allowing uncertainty of the time separation T and T' down to < 0.1 ppb, which is enough for our experiment.

3.4 MOT system

In order to make atoms launch vertically, we trap them with a MOT first. In a MOT, atoms see a position-dependent energy splitting, which has a linear relation with the distance from center and is generated by a pair of anti-Helmholtz magnetic coils. A red-detuned laser light is used as cooling beams. When the atoms move away from the center, the energy shift will better match the laser frequency. Therefore the atoms will absorb photons with the right polarization more easily, which generates a effective restoring force for atom clouds and confine their movement. The atoms in equilibrium will finally get to a temperature close to the Doppler temperature and limited by spontaneous decay heating.

The laser frequency for operating the MOT is selected to be close to the $F = 4 \rightarrow F' = 5$ transition. We red detune the laser to balance between cooling and confining the atoms. Because of the strong intensity of the MOT laser beams, the atoms will eventually decay into $F = 3$ state, therefore an extra repumping beam, in this case with transition $F = 3 \rightarrow F' = 4$, is required. The repumping frequency is the same as the reference laser, but the MOT beam frequency is shifted by ~ 9 GHz from the reference. In order to shift the frequency, as shown in figure 3.10, light from the reference laser will pass an EOSpace fiber coupled EOM to generate microwave frequency sidebands. The frequency is generated by tripling a microwave frequency of 3.056 GHz and filtering it by a 9 GHz bandpass filer. In figure 3.8, the initial reference laser frequency is close to $F = 3 \rightarrow F' = 4$, and the EOM sideband frequency is $3069.5 \times 3 = 9208.5$ MHz. The laser frequency after EOM and Fabry-Perot etalons will be ~ 15.87 MHz red detuned to $F = 4 \rightarrow F' = 4$ transition and ~ 266.96 MHz red detuned to $F = 4 \rightarrow F' = 5$ transition. We drive AOM5 by 16.35 MHz $\times 8 = 130.8$ MHz, where the 16.35 MHz comes from Agilent 3320A and then passes a 8-times multiplier and a tracking voltage controlled oscillator (VCO). After double passing AOM5, the laser frequency is ~ 5.36 MHz red detuned to $F = 4 \rightarrow F = 5'$ transition. It will inject into a Qphotonics diode (QLD-850-150S) with power ~ 50 μW. The diode is driven by ~ 160 mA with output power ~ 150 mW.

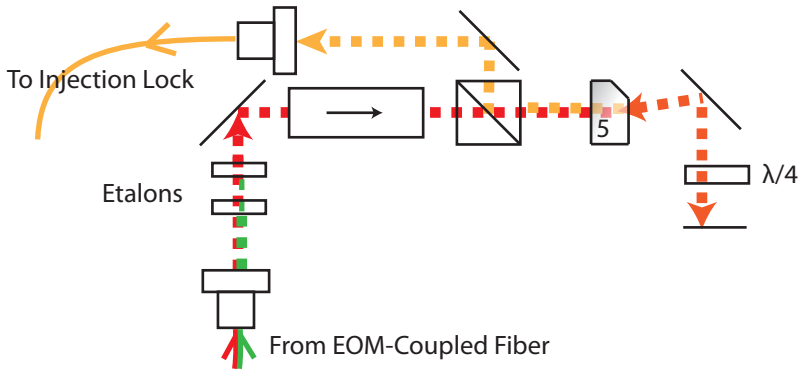

Figure 3.8: Experimental setup for generating the injection lock laser signal from the reference laser. The frequency components are shown in figure 3.9b.

At the start of the trapping sequence, cesium atoms escape from a broken capsule and are directed into a glass cell, in where they are cooled by a 2D MOT. Atoms in the 2D MOT flow in one unconfined direction and enter a large vacuum chamber, as shown in figure 3.3. In the large chamber the flowing atoms are trapped by the 3D MOT. For the 2D MOT, the laser size entering the cell is about one inch by three inches. There are four beams in the 2D MOT system, each of them has about ~ 200 mW of optical power. Similarly, the spot size for the 3D MOT is about one inch in diameter, with a power of about 20 mW. For each MOT beam there are two frequency components. As shown in figure 3.10, we combine

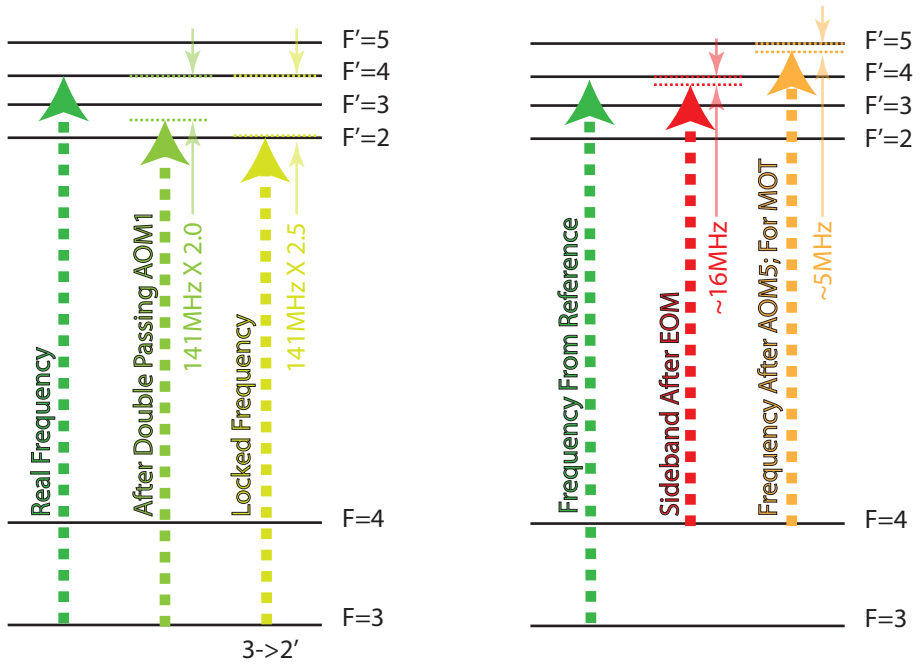

(a) Frequency components in the reference laser experimental setup.

(b) Frequency components about the injection lock of the diode.

Figure 3.9: Frequency components in the reference laser experimental setup and the injection lock of the diode.

the light from the injected diode with the original reference laser and send them into three tapered amplifiers with input power $10 - 15$ mW. These amplifiers are two Eagleyard 1 W, driven by 2.5 Amp for two pairs of 2D MOT beams, and one M2k-laser 1.5 W for 3D MOT beams, driven by 2.5 Amp. The light before the 3D MOT tapered amplifier is shifted 80 MHz by AOM7, which brings extra frequency freedom and is important for the atomic fountain in section 3.5.

For the 2D MOT, lasers after the tapered amplifier pass through pairs of cylindrical lenses to shape the light profile to the right aspect ratio to fit the 2D MOT cell. After passing through optical beam splitters to fine adjust the power, the beams are enlarged by lenses to cover the glass cell, as shown in figure 3.11. Each coil in the 2D MOT system is about 120 turns, and is driven by about 0.7 Amp. The light is controlled by shutters and will turn off after 0.99 seconds from the beginning of the time sequence. The time sequence is shown in figure 3.14.

For the 3D MOT, we use one single pair of 25 turns MOT coils with 8 inches of the diameter which is constructed using hollow core wire so it can be water-cooled. The current turns on at 30 Amp for one second and turns off. The atoms are loaded in this one second. Overall the atom flux is about 10^9 per second.

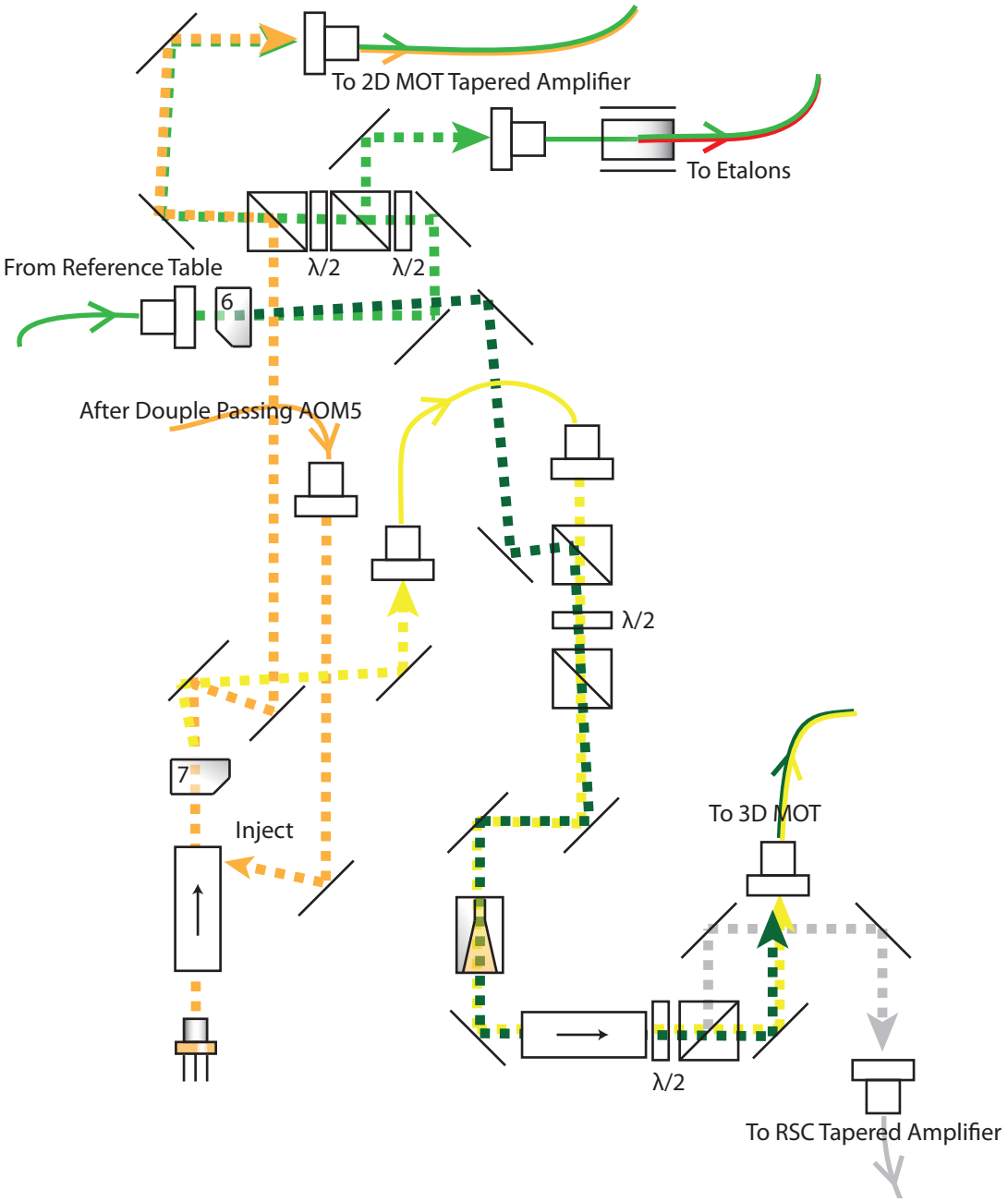

Figure 3.10: Laser system on the MOT table to generate the powerful laser beams for the MOTs. Their frequency components are shown in figure 3.12a. Some light is also used for Raman sideband cooling, see section 3.13.

3.5 Atomic fountain

In addition to the main anti-Helmholtz coil in the 3D MOT, there are three other pairs of compensation Helmholtz coils. They are used to cancel the residual magnetic field after

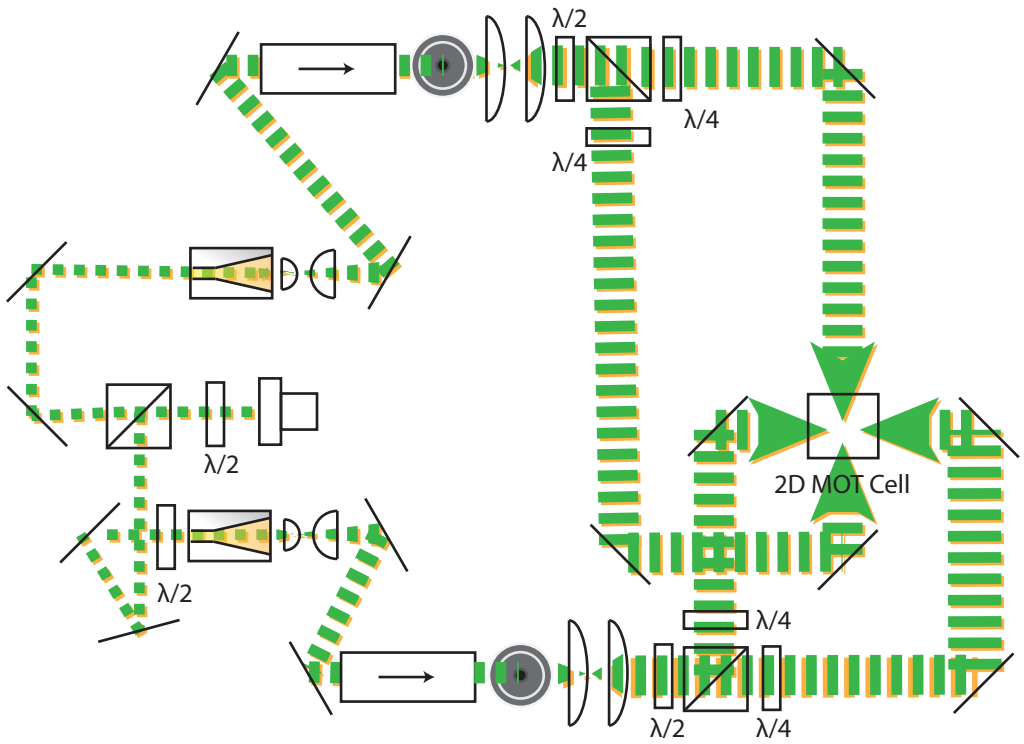

Figure 3.11: Experimental setup for the 2D MOT system. Their frequency components are shown in figure 3.12a.

turning off of the main coil current. The eddy currents will roughly remain for about 30 ms. After 30 ms, three compensation coils make the center of coils nearly zero magnetic field, which is suitable for polarization gradient cooling (PGC). The 3D MOT beams stay on after turning off of the MOT coils for another 45 ms. The time sequence is shown in figure 3.14. During PGC, the laser intensity is ramped down gradually, also the detuning is increased. The laser beams generate a spatial standing wave and also a potential energy modulation due to the AC stark shift. Atoms moving from bottom of the potential will lose their velocity. At the top of the potential, atoms are resonant with a two-photon transition with MOT beams and are transferred into a lower energy magnetic sub-level, which is at the bottom of the energy potential again. The process is repeated and the temperature of atoms will approach the recoil temperature limit.

For the laser detuning in PGC, the frequency driving AOM5 in figure 3.8 is changed from $16.35 \times 8 = 130.8$ MHz to $14.3 \times 8 = 114.4$ MHz, therefore the frequency for the injection lock is red shifted 32.8 MHz. We also red detune the top pairs of the MOT beams by 4 MHz, which is controlled by shifting AOM9 frequency from 80 MHz to 76 MHz, as shown in figure 3.13. Similarly, the frequency of the bottom pairs of the MOT beams is shifted 4 MHz higher by AOM8. These frequency changes generate a moving optical molasses to accelerate the atoms. Therefore, when we switch off the laser beams, the atoms will launch vertically

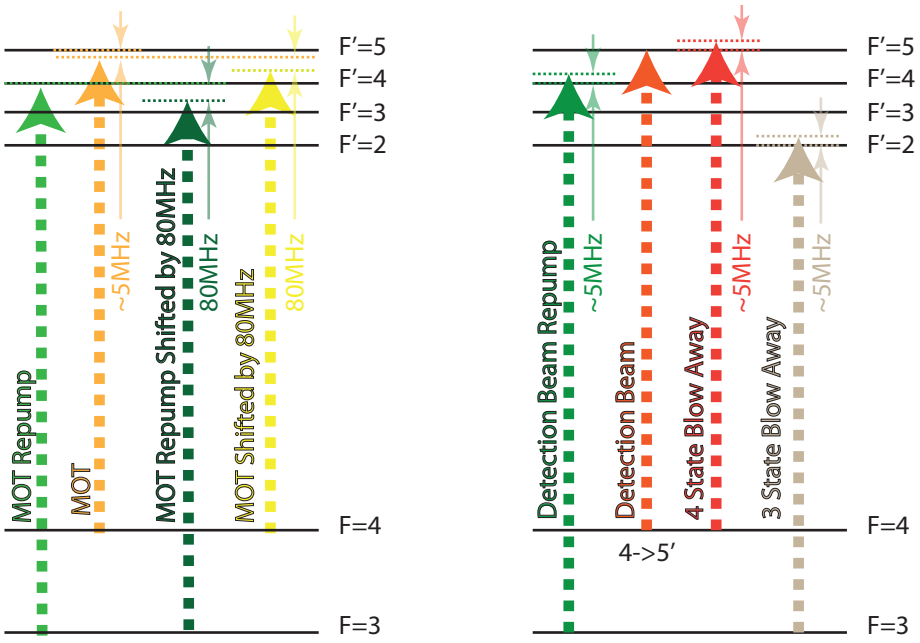

(a) Frequency components for 2D MOT and 3D MOT.

(b) Frequency components for detection and blow away.

Figure 3.12: Frequency components for 2D MOT, 3D MOT, detection and blow away.

with a velocity of 4.8 m/s at temperature of 1.2 μK. The velocity is due to the detuning and the geometry of the beams (in our case, the angle from top or bottom pairs to the horizontal plane is about 45°) and the temperature is measured by comparing the fountain signal width at different times. The atoms will take about 0.5 seconds to travel to the highest point of the trajectory. The overall height that atoms can achieve in this configurations is about 1 meter.

Because lasers for the 4 state blow away and detection also drive transition $F = 4 \rightarrow F' = 5$, these two functions can also be derived by the same beam as the 3D MOT with the help of AOM11 and AOM12, as shown in figure 3.13. Due to a non-overlap in the time sequence between the MOT beams, the detection beam and the 4 state blow away beam will all have enough power. Blow away and detection are discussed in further details in section 3.8 and section 3.10, respectively.

3.6 State selection

Because the phase of atoms with a nonzero magnetic dipole momentum will depend on external magnetic fields to the first order, we want to select atoms with $m_F = 0$ Zeeman state. We achieve this by using a co-propagating Raman transition, which will transfer

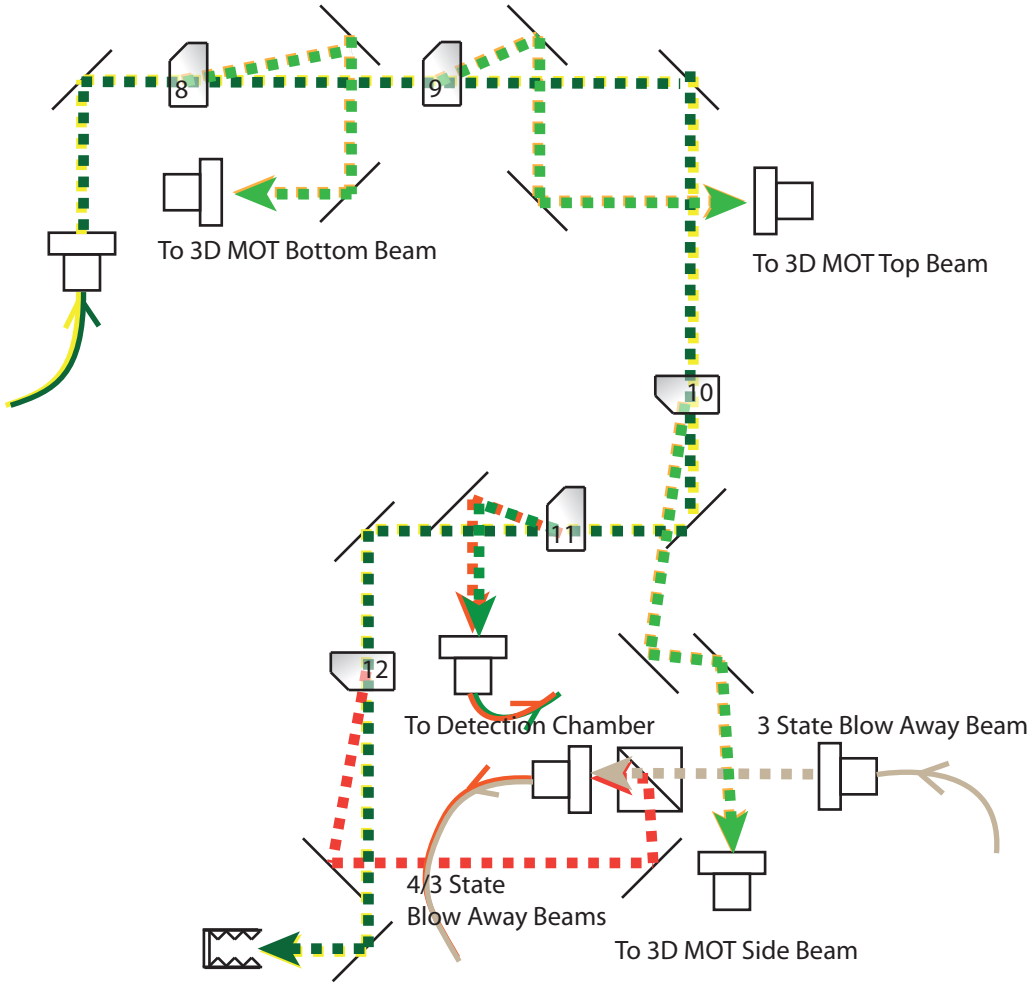

Figure 3.13: Experimental setup for light after the M2k-laser 3D MOT tapered amplifier. The frequency components other than the 3D MOT are shown in figure 3.12b.

atoms between different hyperfine states and is velocity insensitive. In the fountain atoms are distributed into nine Zeeman states after launch. We use laser light along the same path as Bragg diffraction (shown in figure 3.3) to drive the Raman transition. Initially the atoms are in the hyperfine state $F = 4$, and we drive the Raman transition to make the atoms transfer to $F = 3$ state. Because this process happens in a solenoid with a constant small current, there will be energy splittings between different Zeeman states. Outside the solenoid are three layers of mu metal shields to prevent the perturbation of environmental magnetic field. Therefore, we can choose different frequency difference between the pair of laser beams to drive the desired transition, which is $m_{\mathrm{F}=4} = 0 \rightarrow m_{\mathrm{F}=3} = 0$.

In order to generate a laser with far detuned frequency from D2 line for the Raman transition, we use a 1 W titanium-sapphire laser pumped by a 10 W Coherent Verdi, which

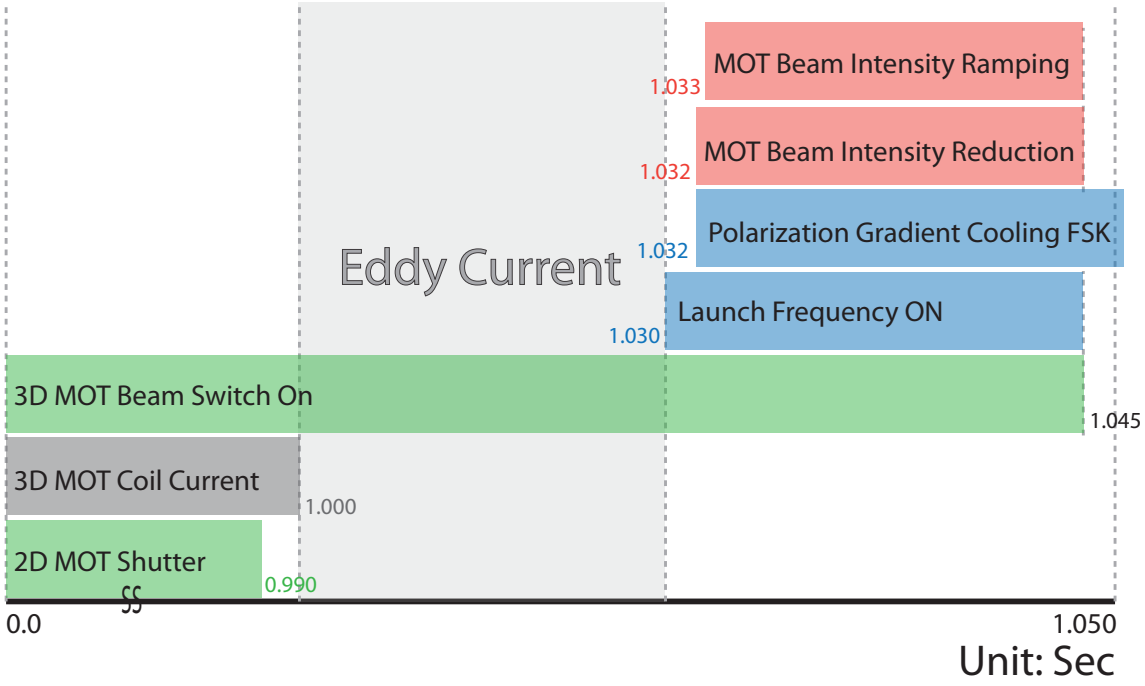

Figure 3.14: Time sequence for the MOT, polarization gradient cooling and the fountain. The bottom line shows the time arrow of the experimental time sequence. For each time period, the beginning and ending times are shown at the bottom left and the bottom right, respectively. Here FSK stands for frequency shift key. In these diagrams of the time sequence, green, blue, red and grey color blocks correspond to light switch, frequency shift, intensity modification, and current switch, respectively.

is phase locked to the reference laser. To do the phase lock, we pick up light from the titanium-sapphire laser and couple it into a fiber together with the reference laser, as shown in figure 3.15. The signal is detected by a fast-response photon diode and mixed with an external microwave frequency, whose value varies from 4 GHz to 12 GHz. The mixed signal will then finally be phase-locked with an external frequency of 160 MHz, whose error signal will be fed back to the titanium-sapphire servo. The half-line width of the beat signal is ~ 350 kHz. Because there are sidebands resulting from the mixer, an external wavemeter is required to make sure the frequency is red or blue detuned from the reference laser.

The titanium-sapphire laser whose frequency is locked to the reference laser passes through AOM13 and is injected into a 6 W titanium-sapphire laser pumped by a Coherent 18 W Verdi. The output of the 6 W titanium-sapphire is partially picked up and sent into a Wollaston prism to generate error signals to stabilize the frequency. The fast response

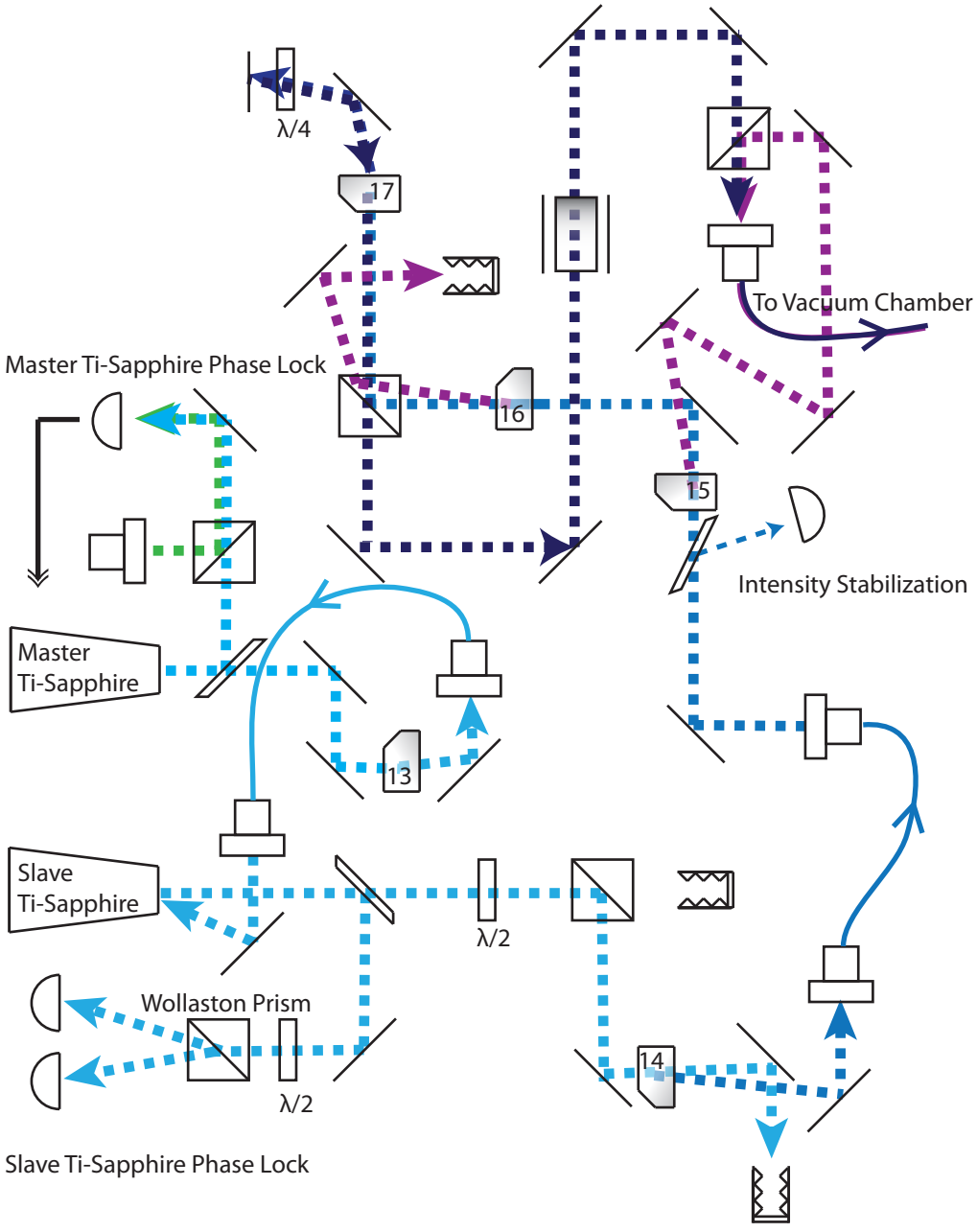

Figure 3.15: Experimental setup on the titanium-sapphire table, including state selection, velocity selection, Bragg diffraction and Bloch oscillations (section 3.14). The frequency components are shown in figure 3.16a.

is controlled by AOM13 by frequency modulation and the slow response is controlled by feeding back to a piezoelectric actuator mirror of the titanium-sapphire laser. The output of the 6 W titanium-sapphire laser then passes through the intensity-stabilization AOM14, and

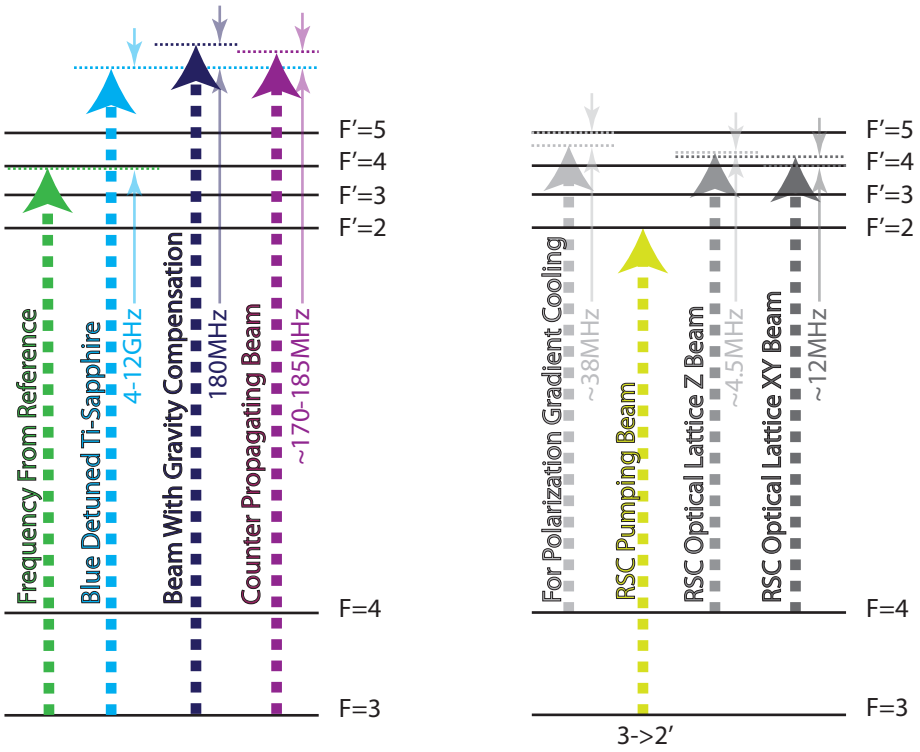

(a) Frequency components on titanium-sapphire table.

(b) Frequency components about Raman sideband cooling.

Figure 3.16: Frequency components for state selection, velocity selection, Bragg diffraction, Bloch oscillations and Raman sideband cooling.

the first order diffracted beam couples to a fiber. The light after the fiber is partially picked up and detected by a fast diode to compare with reference voltage, which comes from a TTL pulse after voltage regulation. Any deviation will be compensated by the radio frequency power of AOM14, which stabilizes the intensity of the beam.

After intensity stabilization, the frequency of the laser beam needs to be shifted to drive the transition between different hyperfine states. We realize this by passing the laser through an EOM with a frequency close to the hyperfine splitting of cesium 6s $^2S_{1/2}$ states. The EOM frequency is generated by a dielectric resonator oscillator that is phase locked to a 180 MHz reference multiplied by 51 by a radio frequency comb and mixed with frequency 12.623 MHz. The frequency 12.623 MHz is used to fine tune the microwave frequency. The exact frequency ($180 \times 51 + 12.623 = 9192.623$ MHz) will not perfectly match the hyperfine state of cesium atoms (9192.631170 MHz) due to the AC Stark shift. The EOM ensures a perfect phase coherence between the frequency components, which is important to achieve a coherent and efficient Raman transition, as shown in equation (2.80). But these sidebands will generate other issues in state selection. As shown in figure 3.17a and figure 3.17b, two

sidebands combined with the original carrier will drive not only one but actually two Raman transitions. For different detunings there will be different frequency compositions for state selection. Therefore state selection depends on the sign and amplitude of the single photon detuning Δ, as verified by the experiment. In addition, the second and third harmonics of sidebands will still contribute to the transition, though they may be negligible. We can always minimize the effect by adjusting the power of the EOM to change the relative amplitude of different sidebands.

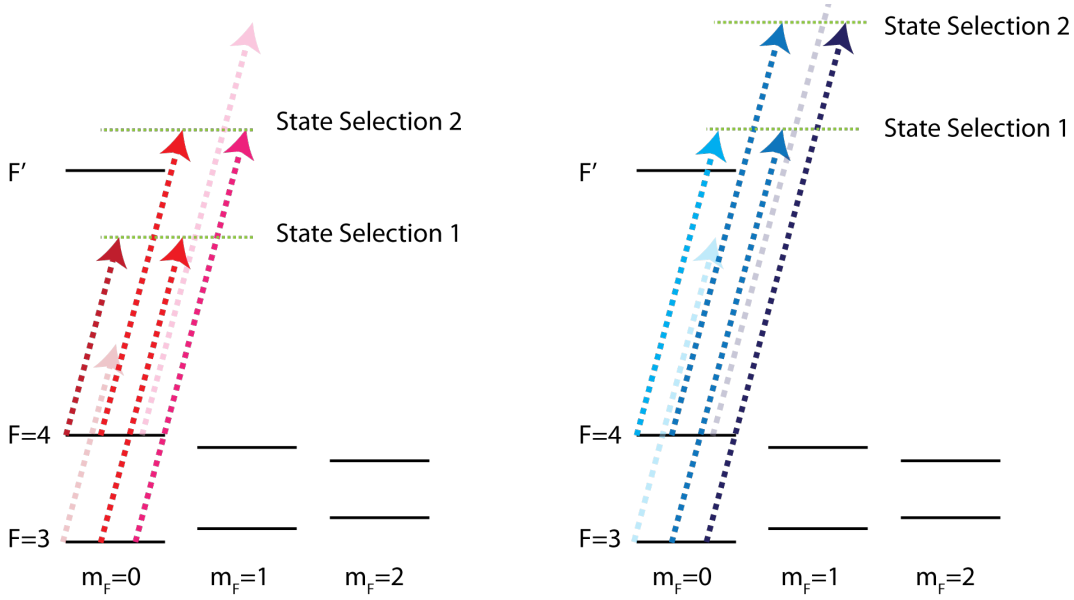

(a) State selection in red detuned case. (b) State selection in blue detuned case.

Figure 3.17: Possible frequency combinations in state selection. They contain one carrier and two sidebands for each case. Frequency components of the transition are shown in opaque dashed lines and components which are not resonant are shown in half transparency.

Things get more complicated when considering retro-reflected light. The retro-reflected light will shift the frequencies seen from the atoms, due to the Doppler effect. The polarization will also change, for example, from σ_+ transition to σ_- transition, due to a $\lambda/4$ waveplate before the retro-reflected mirror. These extra components during state selection can drive other unwanted transitions, as demonstrated in figure 3.18. This transition is velocity sensitive due to the Doppler shift and also sensitive to external magnetic fields. This may generate fake peak signals, but can be checked by changing the solenoid coil current. Moreover, even with correct frequency components, the polarization of the laser is spatially-modulated due to the retro-reflected beam. The overall effective Rabi frequency of state selection depends on the Clebsch-Gordan coefficients (i.e., polarization), therefore the effective intensity is modulated spatially. This results in a shape modification of state selection signals and can be verified by misaligning the top mirror on purpose. For aligning the top

mirror, we install two micrometers (Newport BM25.40) that rest on a homemade framework to hold the mirror against a bellow.

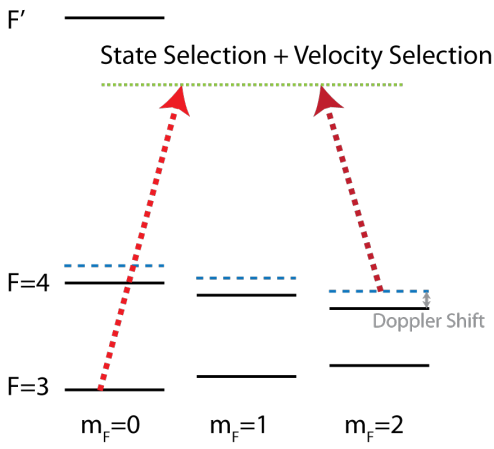

Figure 3.18: Possible wrong frequency combinations in state selection.

Measured signals after state selection in different condition are shown in figure 3.19. The frequency separation between the signal peaks is about 180 kHz, which in our experiment corresponds to 0.1 Amp current in the solenoid. The correct transition can be verified by varying the solenoid current. Signals from the desired $m_{\mathrm{F}=4} = 0 \rightarrow m_{\mathrm{F}=3} = 0$ transition should be insensitive to the current change. Because the two-photon transition linewidth only depends on the pulse duration, it should be long enough so different transition will not be mixed. In our case the pulse duration is 100 μs, as shown in figure 3.20. After state selection, the remaining $F = 4$ atoms are removed by a 4 state blow away beam (see more details in section 3.8). Because initially the atoms are distributed evenly in nine Zeeman states, the efficiency of state selection will be about 10%.

3.7 Velocity selection

In our atom interferometer, we use Bragg diffraction to change the vertical trajectories of atoms. In Bragg diffraction, the frequency detuning between different momentum states is relatively small, about 8 kHz each order. In order to drive the same Bragg diffraction for as many atoms as possible, the momentum distribution in vertical direction should be narrow. We achieve this by a counter-propagating Raman transition. Atoms with different velocity will see different two-photon detuning during the transition, and only a certain velocity range will be resonant. Therefore the result is velocity dependent. A 150 μs velocity selection pulse drives atoms from $F = 3$ to $F = 4$ first and then the remaining atoms are removed by a blow away beam. After the first velocity selection, another pulse with the same configuration drives a transition with the same frequency components but in opposite

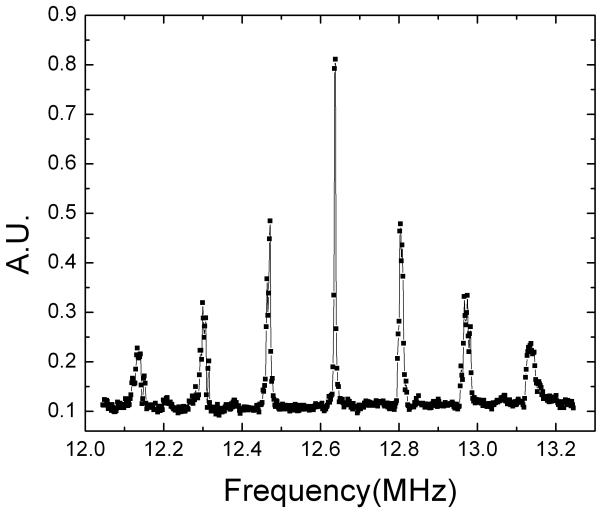

Figure 3.19: State selection signals for transitions between different Zeeman states. The absolute value in the x axis has no specific meaning, only the frequency difference is related to the energy difference in different Zeeman states. There are seven peaks in the signals, corresponding to the seven possible transitions in state selection.

direction ($F = 4 \rightarrow F = 3$), again the remaining atoms are blown away to make narrower momentum distribution.

In order to generate the counter-propagating beam, AOM15 in figure 3.15, driven with 180 MHz, separates laser beams into two different optical paths. These beams are combined again with orthogonal polarizations. Because the laser polarization seen by the atoms will be changed after the retro-reflection of the top mirror, both counter-propagating beams will have the same polarizations and keep the Zeeman state unchanged from $m_{\mathrm{F}} = 0$. Because in velocity selection atoms are transferred between different hyperfine state, the zero order laser beam still contains sidebands due to the EOM. To avoid driving the velocity-insensitive state selection again, the sideband frequency is changed after the state selection, as shown in figure 3.20 (9192.623 MHz $\rightarrow$ 9188.623 MHz). The amount of frequency shift is close to the Doppler shift but not exact, due to the AC stark shift. The possible combinations of frequency components in velocity selection is shown in figure 3.21. There are many possible transitions, and most of them are not desired. The resulting velocity selection signal will have extra momentum $\hbar(k_1 + k_2)$, therefore the peak position is different before and after one velocity selection, which is useful to determine the right peak.

Besides the sideband frequency change, we need to also consider local gravity. State selection is velocity-insensitive, but velocity selection without compensating the deceleration of atoms will have not the same effect at different times, resulting in worse selection efficiency. We use another double-pass AOM17 shown in figure 3.15 to compensate the local gravity and

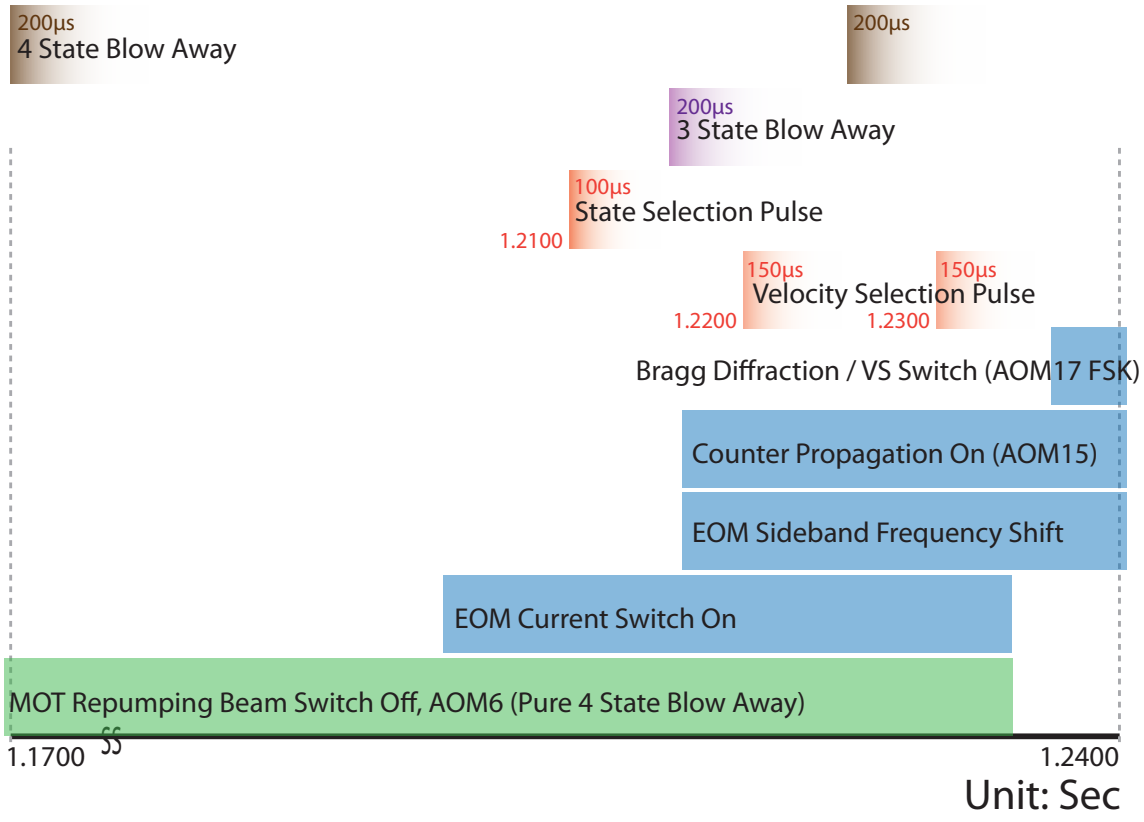

Figure 3.20: Atom preparation time sequence including state selection and velocity selection. For short pulses such as state selection and velocity selection, the time block is shown in gradient color, and the pulse width is shown in the top-left. Exact starting and ending times are not shown if they are not critical to the final result.

also change the two-photon transition detuning for velocity selection. The radio frequency sent into AOM17, which is about 90MHz, comes from a VCO whose input frequency is derived from the sum of a gravity compensation ramping and a frequency doubled Agilent 3320A. The gravity compensation frequency is generated by Analog Devices AD9954, ramped from 59.474999968 MHz to 47.974999984 MHz, ramping 0.146 Hz in each 0.0127 μs step. For simplicity, we ramp only the upward-going beam. The ramping rate is therefore twice the Doppler shift. Agilent 3320A in this setup is used to fine tune the two-photon frequency difference δ to select the correct transition.

The signals before and after velocity selection are shown in figure 3.22. We can see the

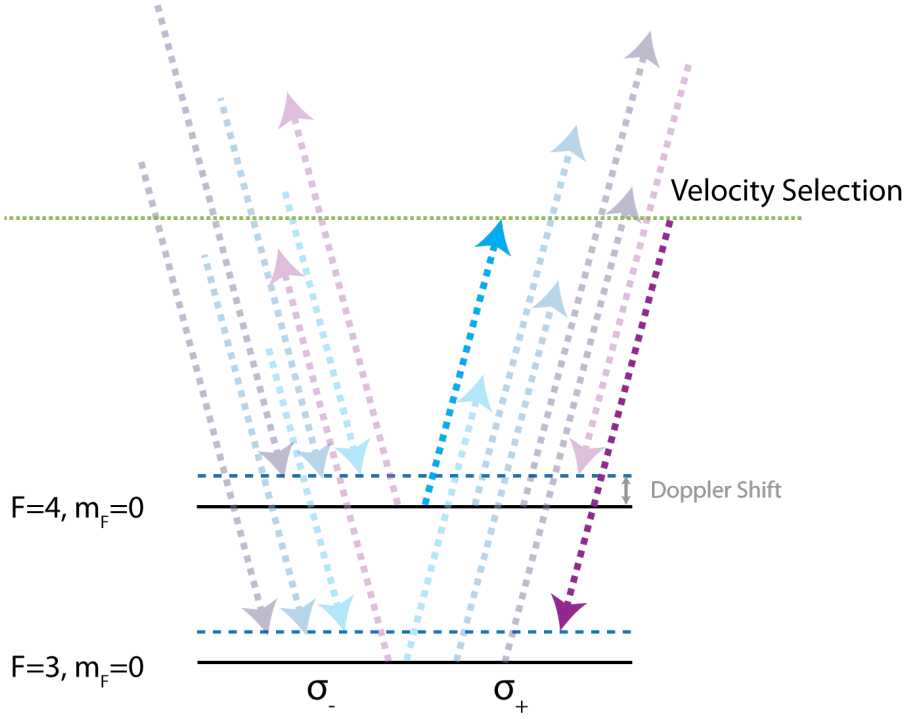

Figure 3.21: Possible frequency combinations in velocity selection. Initially there are three frequency components from light passing through the EOM in blue color and one from light not passing in purple color. We assign the beam passing the EOM as σ_+ polarization, and the other as σ_-. They are shown as arrows pointing up. After being retro-reflected, these beams, which are shown as arrows pointing down, change their polarizations and Doppler shift their frequency relative to the atoms.

resulting smaller signal width, which corresponds to a narrower velocity distribution.

3.8 Blow away

After each state selection or velocity selection pulse, atoms are transferred into the other hyperfine state. The remaining atoms should be cleaned to get better signals. The way of doing this is to shine in a strong laser beam with a cycling transition that transfers large momentum to the remaining atoms. We call these laser beams the blow away beams. Depending on the hyperfine state driven, they are classified into 4 state blow away and 3 state blow away beams. The frequency components are shown in figure 3.12b. Atoms with undesirable hyperfine state will gain a large momentum and fall back to the detection region at a much later time. Therefore they will not perturb signals detected. If the blow away beam does not work properly, the remaining atoms will cause a hump in the signal and the tail of the hump will add to the atom interferometer signals detected, which introduces extra

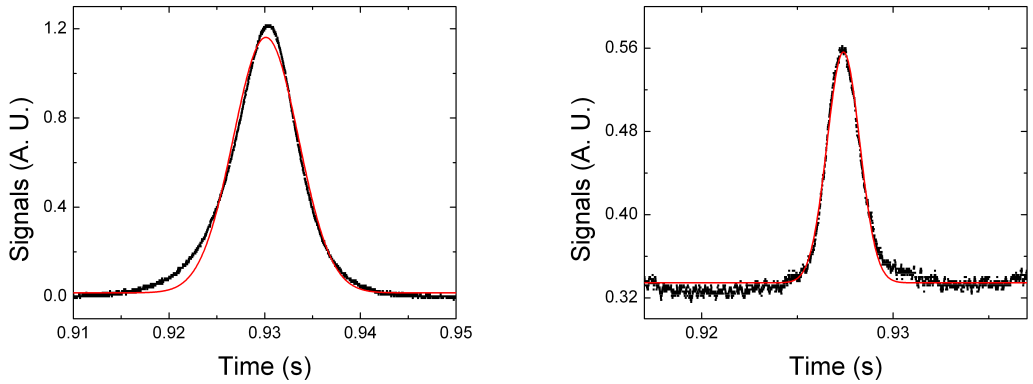

(a) Signals without velocity selection, whose half width is about 6.8 ms.

(b) Signals with velocity selection, whose half width is about 1.7 ms

Figure 3.22: Comparison between fountain signals with and without velocity selection. The y axis shows the voltage signal from a PMT, and the x axis shows the time coordinate. The Gaussian fitting curve is shown in red line, and the data points are in black.

noise.

The 3 state blow away beam is obtained from the reference table, as shown in figure 3.6. The 4 state blow away beam is derived from the MOT table, as shown in figure 3.13. The 4 state blow away switch is controlled by AOM12. On the table, in addition to the $F = 4 \rightarrow F' = 5$ transition of the blow away, there is the MOT repumping beam which drives the $F = 3 \rightarrow F' = 4$ transition. The repumping beam will ruin the function of the blow away beam, therefore we switch it off using AOM6, as shown in figure 3.10.

The 3 state blow away and 4 state blow away beams are combined into a fiber before entering the vacuum chamber, and therefore share the same optical path. However, due to the limited power of 3 state blow away ($\sim$ 2 mW), the blow away beams do not share the same path as the titanium-sapphire laser, otherwise the extra optical beam splitter will suppress the overall available optical power for blow away. As shown in figure 3.23, one lens is added in the blow away beam path to make sure blow away beams cover the same region as the titanium-sapphire laser beam.

In order to achieve better performance, blow away beams should not be circular polarization due to the dark states in $F = 3 \rightarrow F' = 2$ transition. In addition, their frequency should be a little blue detuned to compensate the Doppler shift. A poor blow away configuration will not only require longer pulse but can also introduce some hot atoms into the undesired hyperfine state from spontaneous decay. In our case, the efficiency of the 3 state blow away beam is worse and we choose the 4 state blow away beam as our final step.

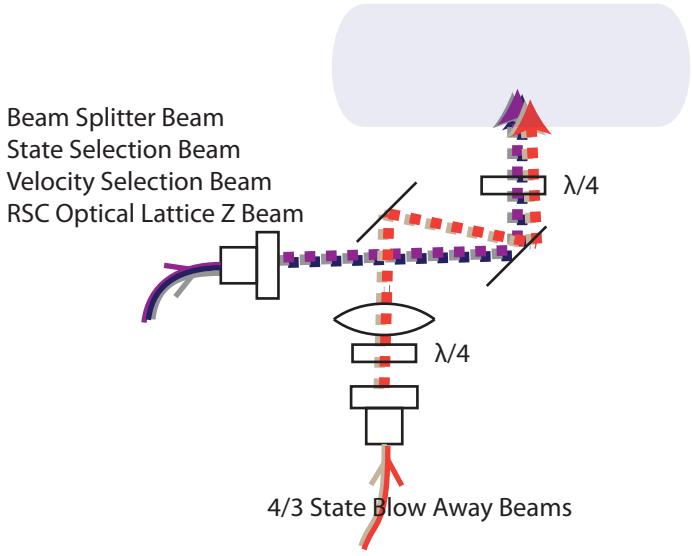

Figure 3.23: Bottom part of the vacuum chamber. In where the blow away beams and beams from the titanium-sapphire table enter the chamber. The half-transparent blue rounded rectangle represents the vacuum chamber.

3.9 Bragg diffraction

The setup for Bragg diffraction is similar to velocity selection. After one state selection pulse and two velocity selection pulses, atoms are in the $F = 3$ state, and we use far detuned (4.5 GHz to 13 GHz, blue or red) laser beams to generate Bragg diffraction. The large detuning is used to prevent single photon transitions which destroy accumulated phases of the atoms. Under large detuning, strong intensity is required to make Bragg diffraction work. From equation (2.81), we can estimate the power required to drive Bragg diffraction order n with a detuning of $\Delta = 10$ GHz will be about $10n^2$ mW/cm^2. In our setup, we usually adopt $n = 5$ as a balance between reasonable maintenance time and high sensitivity. The intensity stabilization mentioned in section 3.6 now compares the detected light with a Gaussian profile generated from Agilent 3320A to make intensity fluctuation down to less than 5%. The stability of Bragg diffraction pulses will lower the overall noise.

After intensity stabilization, we again generate counter-propagating beams by steps mentioned in section 3.7. Compared to velocity selection, Bragg diffraction only drives atoms into the same hyperfine state, and its frequency components are relatively straightforward for the first two beam splitters. The EOM is not switched on, and the radio frequency that drives AOM17 is shifted after velocity selection to satisfy the Bragg diffraction condition, as shown in figure 3.20.

For the third and fourth pulses there should be two beam splitters driven at the same time. Therefore AOM15, which generates counter-propagating beams, is now driven by 180

MHz $\pm\,\omega_{\mathrm{m}}/2\pi$, where ω_{m} is mentioned in section 2.3. Driving two frequencies at the same time will cause amplitude modulation in the zero order of AOM15 which will disturb the Bragg diffraction condition. We add AOM16 to drive the same frequency component but out of phase, which smooths out the pulse shape of the zero order Bragg beam. Due to the extra frequency components, the overall Bragg diffraction intensity needs to be adjusted to allow for the same Rabi frequency for all four beam splitters.

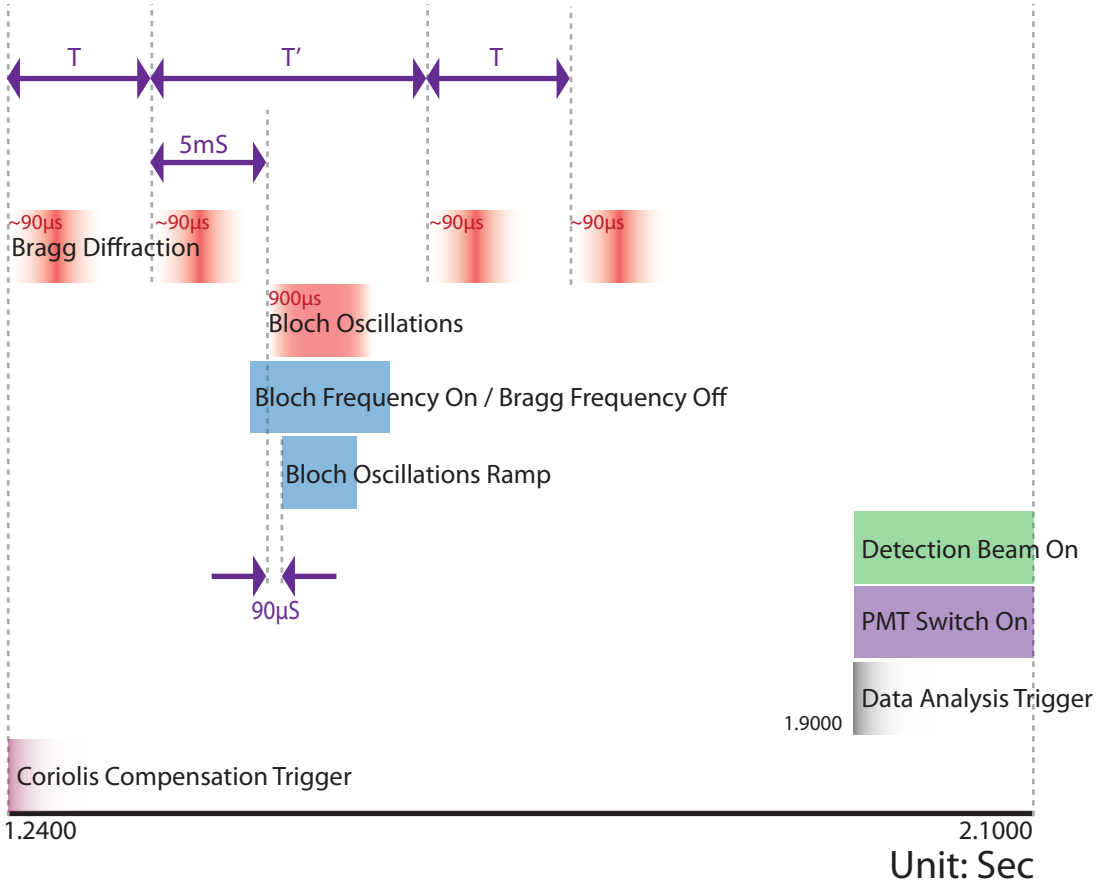

Figure 3.24: Atom interferometer time sequence. For Bragg diffraction and Bloch oscillations (see section 3.14), because the light pulse changes its intensity in time, these areas are shown in gradient color. The pulse time is shown in the top left of the block. For Bragg diffraction, the pulse time is defined as the time between two points whose value is 1/40 of the peak amplitude in the Gaussian profile reference. The time T and T' is the same as used in the phase calculation. For the time sequence without Bloch oscillations, T' is chosen to be 2 ms instead of > 5 ms.

3.10 Detection and data analysis

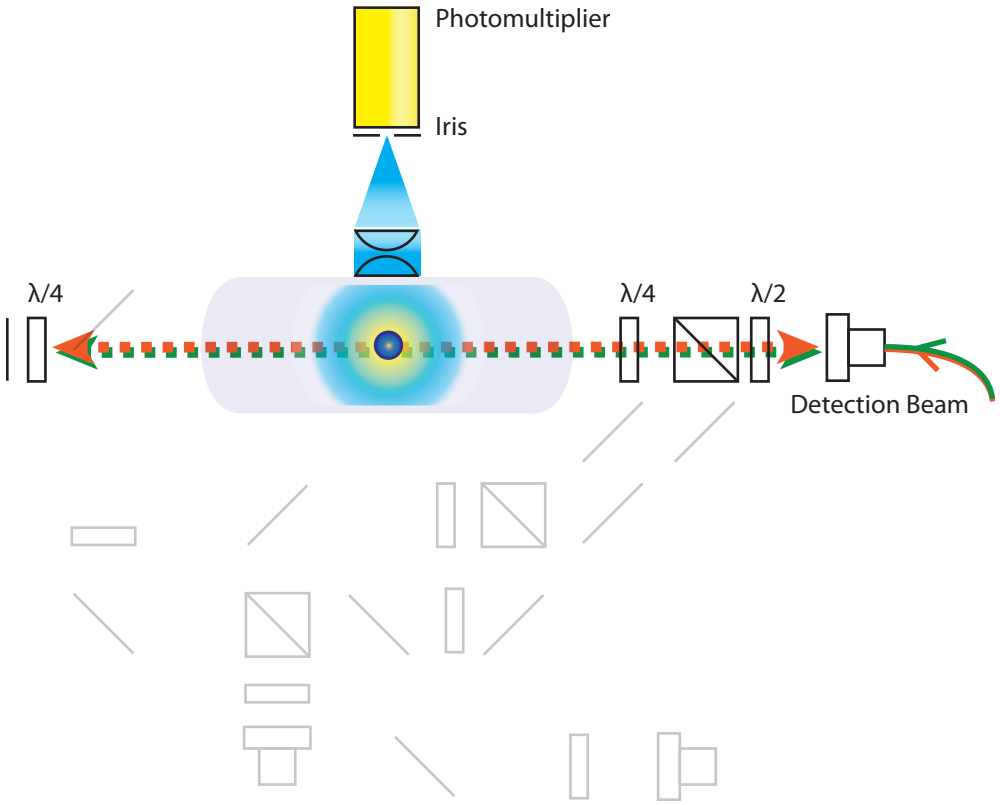

Figure 3.25: Experimental setup of detection. Other setups are half transparent. Atoms shown in gradient blue circle are inside the chamber with fluorescent light. The fluorescence is shown in half-transparent gradient from yellow to blue.

After the four beam splitters, the falling atoms are detected by fluorescence method. We switch on the detection beam at 1.9 seconds of the time sequence, as shown in figure 3.24. For detecting atoms, we use the laser with resonance frequency $F = 4 \rightarrow F' = 5$ combined with $F = 3 \rightarrow F' = 4$, which is very similar to the MOT frequency. The frequency components are shown in figure 3.12b. We add AOM12 at the end of the MOT beam to make the frequency on resonance, as shown in figure 3.13. The fluorescence is detected by a Hamamatsu photomultiplier R943-02 with voltage of 720 V and converted to voltage by a preamplifier. In order to have as much solid angle as possible, two N/A ~ 1, 10 cm diameter lenses are used to collect the fluorescence, as shown in figure 3.25, covering about $\sim 5\%$ of the overall solid angle. It is also possible to use another spherical mirror at the opposite side to double the collected signals.

The high sensitivity of PMT will amplify small amount of scattered light from the experiment, which can contribute to significant noise signals. Therefore scattering light blocking

is required. We can also adjust the iris before the PMT to narrow down the detection region and select the desired light signals.

A data analysis trigger starts a National Instruments card NI4474 which collects signals from the PMT, as shown in figure 3.24. From the signals we can observe the fluorescence peaks for atoms with different velocities, as shown in figure 3.26a. The four main peaks from left to right correspond to output 1-4 in figure 2.1 and 2.2, respectively. In our Ramsey-Bordé atom interferometer, only half of the atoms participate in the interference (the solid lines in figure 2.1 and 2.2), yet other atoms will also be detected. Due to the velocity difference, these atoms will not overlap perfectly with output 1-4. Therefore the detected signal will not only be four peaks, but four pairs of close peaks in short time separation. However, it is easy to distinguish different kinds of peaks, since atoms without interference will keep the same amplitude in each shot. The size of the vacuum chamber and the launch velocity limits the maximum time separation can be achieved. In our case, for time separation larger than 300 ms, there is no enough time for separating atoms with different recoil velocity, which results in low visibility of the fringes.

In order to remove the effect of these remaining atoms, we weigh detected signals with a Gaussian curve which has narrower width than the received signals. From the weighted values in each shot, one point of an ellipse can be drawn, as shown in 3.26b. From the ellipse phase, the recoil frequency can be calculated.

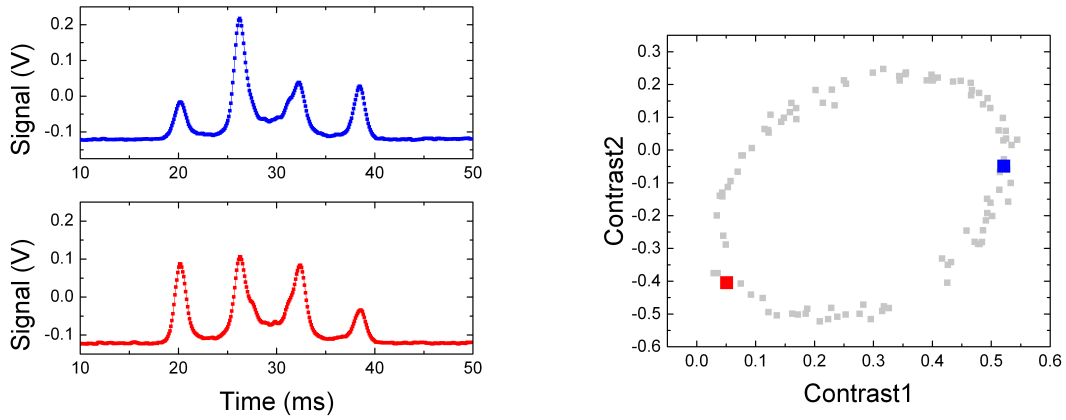

(a) Data taken from the PMT after the data analysis trigger.

(b) Ellipse which is obtained from 100 detected signals.

Figure 3.26: Examples of data analysis. The red and blue lines show detected signals. From the signals, contrasts can be calculated and corresponding points can be drawn in a x-y plane (red and blue squares). An ellipse can be fitted after a certain number of points.

As mentioned in section 2.5.2, in the ideal case we will not choose $8n\omega_r$ from equation (2.50) as the measured frequency but would like to choose $8n\omega_r \pm \omega_\varepsilon$ such that the relative phase between the two fringes will be $2\phi_d = 2n\omega_\varepsilon T = 2\pi/5$ (72°) for a better ellipse fitting. However, we are not able to choose the correct frequency in the beginning due to the

statistical uncertainty and systematic errors. Therefore, the initial frequency ω'_{m} may not be exactly $8n\omega_{\mathrm{r}}$ as we expected. In this case, the two frequency $\omega'_{\mathrm{m}} + \omega_{\varepsilon}$ and $\omega'_{\mathrm{m}} - \omega_{\varepsilon}$ will generate phases other than 72°. The difference between the two ellipses will no longer be zero, but $4nT(\omega'_{\mathrm{m}} - 8n\omega_{\mathrm{r}})$, which can be used to correct ω'_{m} to the value of supposed $8n\omega_{\mathrm{r}}$.

3.11 Coriolis force compensation

As we showed in section 2.8, the Coriolis force will introduce a mismatch of the wavepacket which decreases the overall contrast. In order to compensate this, we installed two Thorlabs AE0505D16F piezoelectric actuators above the micrometers that holds the top mirror. The two piezoelectric actuators define the rotation axes, and are roughly pointing west ≡ x' and south ≡ y', enclosing an angle of 82°, as shown in figure 3.27. The actuators have been calibrated against an Applied Geomechanics 755-1129 tilt sensor. We can use this to give the momentum transfer $k_1 - k_2$ a constant direction as seen from the inertial frame, in spite of Earth's rotation, to compensate for the Coriolis force. The Coriolis compensation trigger will occur at the beginning of AI process, which causes a voltage ramp to drive the piezoelectric actuators, as shown in figure 3.24.

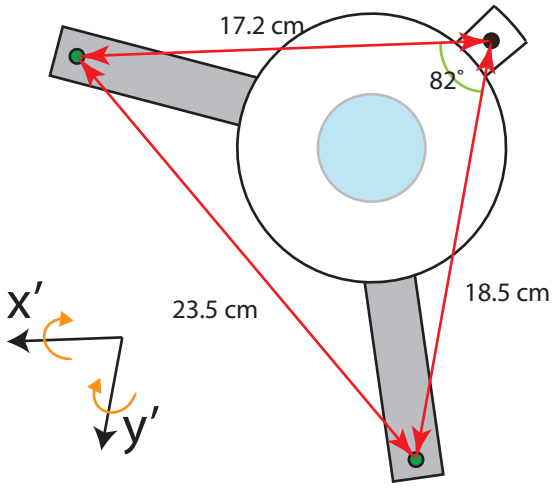

Figure 3.27: Top mirror sketch. Blue circle represents the top mirror, black spot indicates a fixed point holding the bellow (white part), and green spots indicate where the piezoelectric actuators are placed. The rotational axes are shown in bottom-left.

3.12 Compton clock

For the Compton clock, the crucial requirement is to make sure the result only depends on the particle's mass. In order to make a timebase reference of all the equipment, a voltage-

controlled 10 MHz crystal oscillator O1 (FTS 1050A) with angular frequency ω_{cryst} is the master oscillator for all frequency sources, pulse generators, and lasers involved in the Compton clock experiment. The frequency comb multiplies ω_{cryst} by a factor of $N_{\text{c}} = 35173594.165$ into the optical frequency range, and stabilizes the laser angular frequency to $N_{\text{c}}\omega_{\text{cryst}}$.

To switch ω_+ and ω_- as shown in section 2.7.2, a direct digital synthesizer (DDS) generates $2(\omega_+ - \omega_-) = 2\omega_{\text{b}} = N_{\text{DDS}}\omega_{\text{cryst}}$ at ~ 82 kH$z \times 2\pi$, where $N_{\text{DDS}} = 2326621801616/2^{48}$. The factor N is thus $N = N_{\text{c}}/N_{\text{DDS}} = 4255305521.31286$. As shown in figure 3.28, the servo includes the program measuring the relative phase, and compares it with the ideal phase output (which we set as $\pm 72°$, as mentioned in section 3.10). For the correct frequency ω_{b}, the atom interferometer result should stay in the center of zero fringe (i.e., both ellipse have 72° phase). From the deviation we can calculate the correction, and output the corresponding control voltage to the crystal oscillator.

Our frequency comb generator (Menlo Systems FC8004) is based on a mode-locked, femtosecond titanium-sapphire laser and a photonic bandgap fiber [21]. The comb's output spectrum has components at angular frequencies $\omega_q = q\omega_{\text{rep}} + \omega_{\text{off}}$, where q=1,2,... . The 200 MHz repetition rate ω_{rep} is phase-locked at 20 ω_{cryst} to the signal from O1; the offset frequency ω_{off} of 20 MHz is phase-locked to 2 ω_{cryst} by carrier-envelope phase stabilization. A sample of the laser frequency is sent to the comb laboratory via an optical fiber; its beat note with the $q = 1758678^{\text{th}}$ comb line is obtained. The beat frequency is bandpass filtered at 30 MHz and compared with 3 ω_{cryst} to phase lock the laser. When the feedback loop is closed,

$$\omega_{\text{L}} = (20q + 2 + 3 + 8 + 12.165 + 9)\omega_{\text{cryst}} = N_{\text{c}}\omega_{\text{cryst}}, \tag{3.1}$$

where the summands of 2, 3, 8, listed in order of appearance represent: the shifts due to the comb offset ω_{off}, the beat frequency, and AOM14 to shape the laser pulses, as shown in figure 3.15.

The term of 12.165 ω_{cryst} in equation (3.1) represents AOM13 at 121.65 MHz used in laser frequency stabilization, as shown in figure 3.15. It is monitored by a frequency counter referenced to ω_{cryst} and thus has a known ratio to ω_{cryst}.

In the original experimental set up, only one frequency component of the counter-propagating beam pair is ramped. Therefore the overall momentum $\hbar(k_1 + k_2)$ is changed during the atom interferometer. We can compensate this by adding AOM18 to ramp the reference laser frequency in the opposite direction, and sending the ramped laser to beat with the frequency comb, as shown in figure 3.29. The beating signal is used to phase lock titanium-sapphire laser, therefore the laser frequency from the titanium-sapphire laser before AOM17 is ramping all the time. Hence these two frequency ramping from AOM17 and AOM18 will keep $\hbar(k_1 + k_2)$ unchanged, and the net frequency shift from this pair will be 9 ω_{cryst}, as mentioned in equation (3.1).

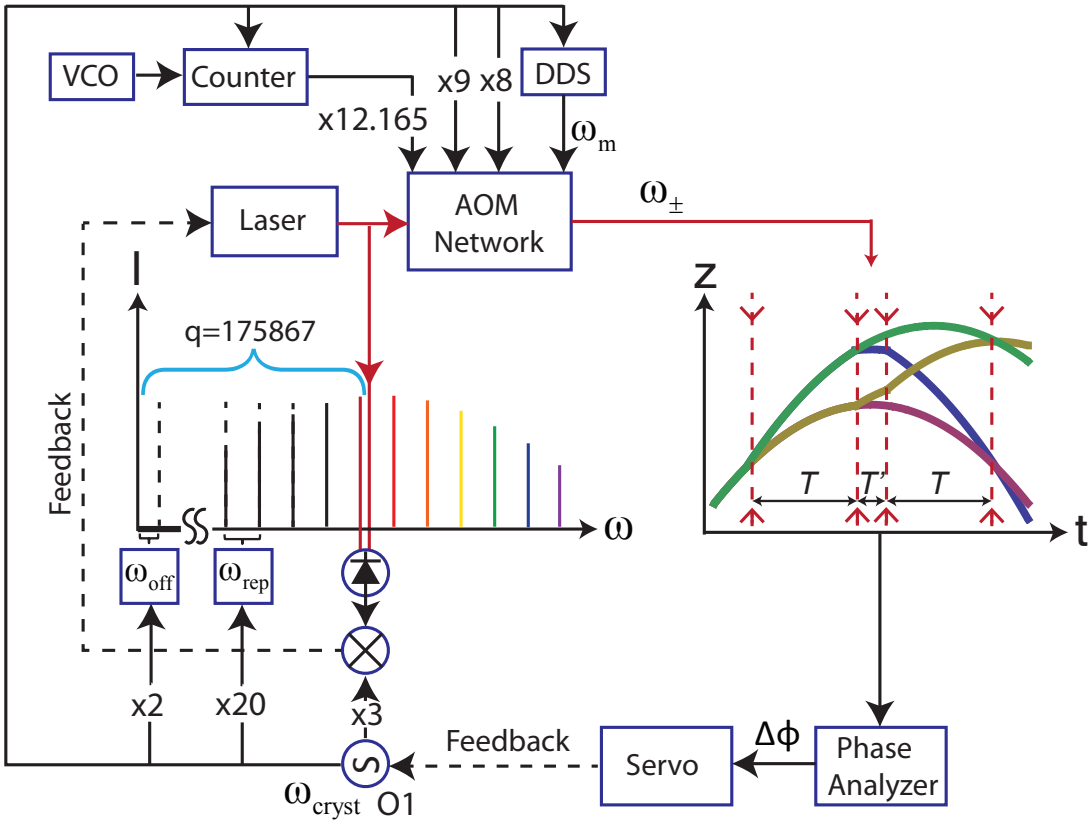

Figure 3.28: Demonstration of the Compton clock setup. Right hand side shows the atom interferometer to measure the phase related to $\hbar/m$, and the left hand side shows the frequency comb to lock the laser frequency. All experiments are referenced to the 10MHz crystal signal ω_{cryst}.

3.13 Raman sideband cooling

In order to further cool atoms and increase the SNR, we can implement Raman sideband cooling after the launch. The idea of Raman sideband cooling is to trap atoms into an optical lattice, and then apply a magnetic field and an external pumping beam to drive atoms into the minimum vibrational state, therefore decreasing the temperature of the atoms. The cartoon picture of this principle is shown in figure 3.30. For example, atoms which are initially in $m_{\mathrm{F}} = 1$ and the vibrational ground state can be transferred into $m_{\mathrm{F}} = 2$ and the first vibrational excited state by a Raman transition, whose light comes from the optical lattice beams. Atoms in $m_{\mathrm{F}} = 2$ and the first vibrational excited state can be transferred into $m_{\mathrm{F}} = 3$ and the second vibrational excited state by the same method. This process can

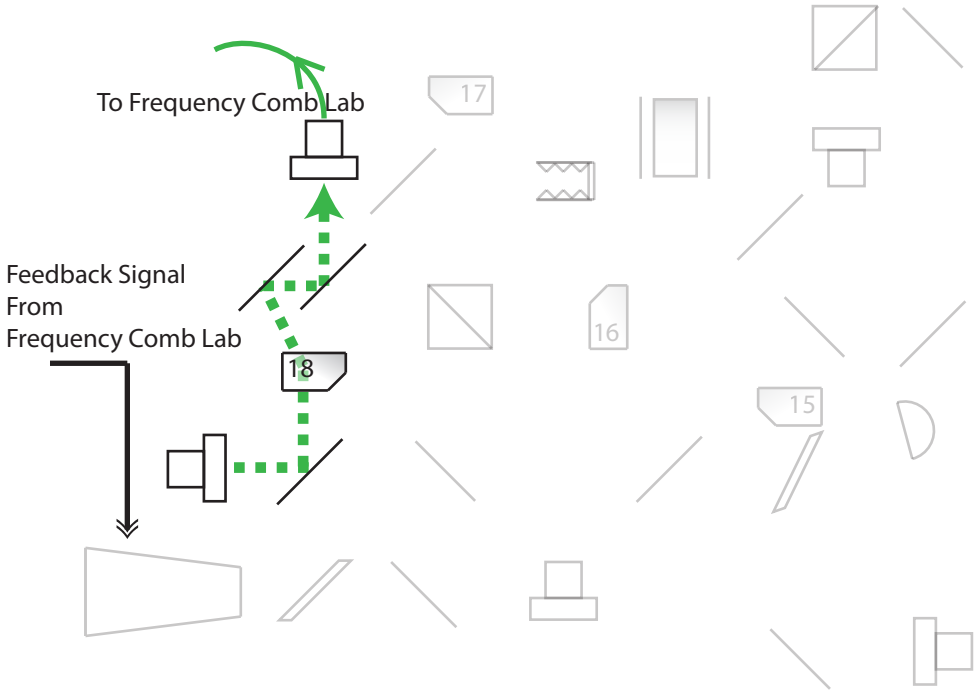

Figure 3.29: Experimental setup to keep the same momentum transfer of the beam splitters in the Compton clock experiment.

be reversed. Therefore, any state other than the vibrational ground state of $m_F = 3$ will be transferred into $m_F \neq 3$ states. Atoms in these states will be pumped into excited state and have a chance to fall into the desired state, or dark state. This process can continue until no atoms are in states other than the dark state, which is a vibrational ground state.

For building the optical lattice, four beams are intersected at 39 cm above the 3D MOT center. They load atoms into the optical lattice. Three beams are in the horizontal plane. Two of them are counter-propagating, and another beam intersects them at about 90°, as shown in figure 3.31. The fourth beam comes from bottom to top, using the same path as the Bragg diffraction beam. In order to share the same path as the beam splitter pulse, the optical beam overlaps with first order of AOM15 and gets coupled into the same fiber, as shown in figure 3.32. Because Raman sideband cooling will load atoms into the optical lattice, it will change the atom launching velocity. For further processes, we want the new velocity direction to be aligned with the beam splitter pulse direction, therefore allowing all the beam splitters to share the same atom conditions.

To get enough power for the optical lattice, parts of the light after the 3D MOT tapered amplifier is directed into another M2k-laser tapered amplifier, as shown in figure 3.10 and figure 3.33. The beam intensity after the fiber is about 15 mW, and the M2k-laser tapered amplifier is driven by 2.5 Amp. The output after another coupled fiber is about 400 mW. The

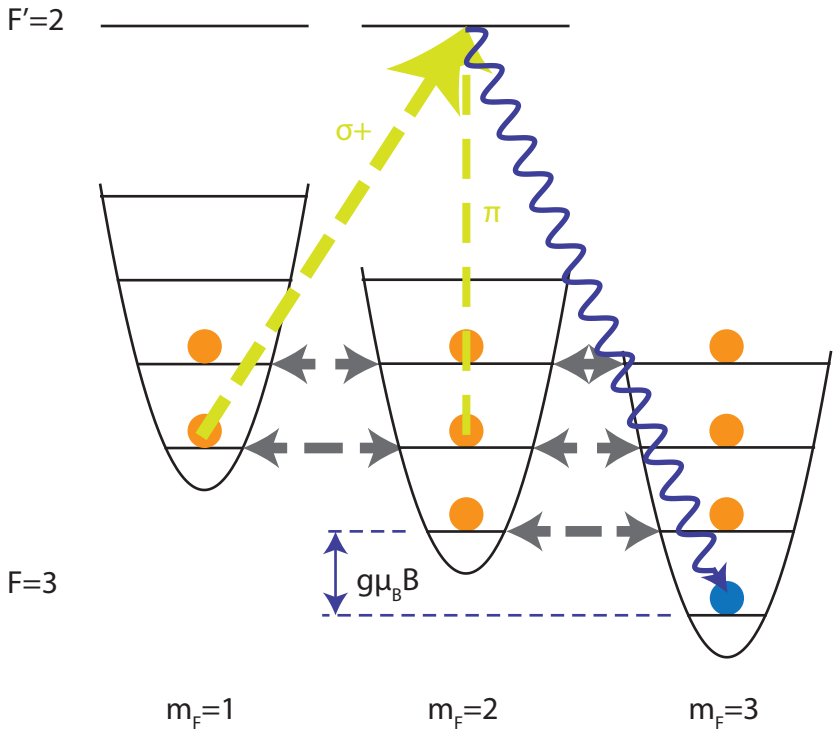

Figure 3.30: Demonstration of Raman sideband cooling principles. Atoms are trapped in an optical lattice, and an external magnetic field B is tuned to make the energy splitting $g\mu_{\mathrm{b}}B$ match the vibrational energy splitting of the lattice. The atoms that are in the dark state are shown in blue, and others are in orange. The optical lattice light is shown in gray, and the pumping beam is shown in green-yellow, the same as in figure 3.31. The spontaneous decay is shown in dark blue curved line.

beam then passes two AOMs, the minus-first order of AOM19 supplies the optical lattice light of the horizontal plane, and the other minus-first order of AOM20 shares the same Bragg diffraction beam path. Because the Bragg diffraction beam is in circular polarization, the vertical direction of the optical lattice will be circular polarized. We therefore choose all other three beams to be circular polarized. The spot sizes for the horizontal optical lattice beams are about 10 mm diameter with overall power $\sim$ 80 mW. The z axis beam size depends on the Bragg diffraction fiber port, which is about 12 mm diameter with power $\sim$ 40 mW. The optical lattice beams may accidentally satisfy the Bragg diffraction condition and therefore generate signals look like Raman sideband cooling signals. The fake signals usually have wider width and do not follow the power change of the pumping beam.

The frequency of the optical lattice beams will be close to the $F = 4 \rightarrow F' = 4$ transition. Therefore the $F = 3 \rightarrow F' = 4$ MOT repumping beam is switched off by AOM6 during Raman sideband cooling. At the same time, the frequency driving AOM5 remains unchanged

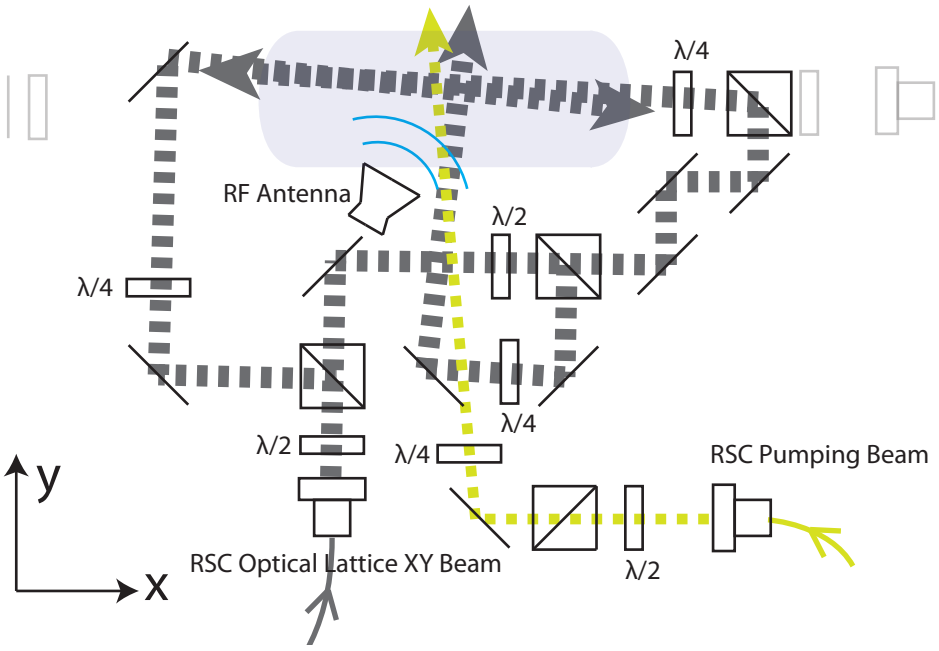

Figure 3.31: Experimental setup of Raman sideband cooling, including x-y direction optical lattice beams and a microwave antenna. At the same stage there is also a detection beam, but the light is not shown in this figure, and related optical components are half transparent. The definition of x and y are shown in bottom-left.

from the PGC process, which is about 38.2 MHz red detuned from $F = 4 \rightarrow F' = 5$. The relevant time sequence is shown in in figure 3.34. Combined with 120.9 MHz which drives AOM19, and another 80 MHz shift by AOM7, the overall frequency is 11.99 MHz blue detuned from the transition. Because the atoms are moving vertically, the vertical beam of the optical lattice should be blue detuned from the horizontal beams. The frequency driving AOM20 is 116.4 MHz and is about 4.5 MHz less compared with AOM19, which corresponds to the Doppler shift. The atoms are in $F = 4$ state after the launch, and they will be transferred into $F = 3$ by spontaneous emission when they are excited by the optical lattice beams. Once the atoms are in the $F = 3$ state, the optical lattice beams are ~ 9 GHz far detuned.

The external pumping beam is used to make the atoms have a chance to decay into the dark state. The frequency of this pumping beam is resonant with the transition $F = 3 \rightarrow F' = 2$. The light is derived from the reference table, as shown in figure 3.6. Because there are less Zeeman states in $F' = 2$ compared to $F = 3$, the pumping beam should be a combination of σ_+ and π polarization as seen by the atoms. The σ_+ polarization pumping beam can achieve this by having $\sim 10^\circ$ angle between the y direction magnetic field coil. In our setup, the pumping beam will shine directly into the PMT and burn out the tube if the PMT is on. Therefore an extra switch is added to turn on the PMT only during the

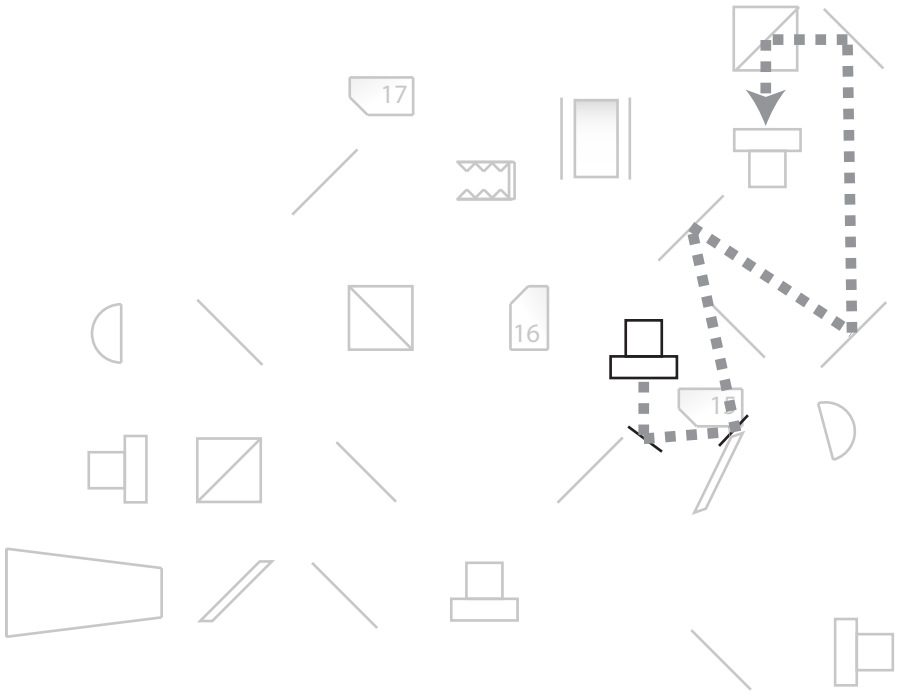

Figure 3.32: Experimental setup of the z directional optical beam in Raman sideband cooling. Other components, also shown in figure 3.15, are not related to Raman sideband cooling and are shown in half-transparency.

detection period, as shown in figure 3.24.

Because Raman sideband cooling requires an uniform magnetic field around the trapped atoms, another three pairs of compensation coils are set around the detection chamber. Just before the atoms entering the optical lattice region, current for the coils is turned on for 47 ms to achieve an uniform magnetic field along the y direction, as shown in figure 3.34.

After Raman sideband cooling, most of the atoms are in the $m_{\mathrm{F}} = 3$ Zeeman state. In order to make the atoms magnetic-insensitive, we prefer them to be in the $m_{\mathrm{F}} = 0$ Zeeman state. We accomplish this by introducing a microwave frequency antenna, as shown in figure 3.31, with frequency ramp from 9192.514 MHz to 9193.640 MHz. The power is amplified by a Hughes 1177H03F000 Traveling Wave Tube Amplifier, with 10 W power output. It then drives adiabatic rapid passage from $m_{\mathrm{F}} = 3$ state to $m_{\mathrm{F}} = 0$ state. The microwave shares the same frequency locking scheme as in state selection, section 3.6. We install a switch to change the 12.623 MHz in state selection to a ramping radio frequency. Compared to the 9192.627 MHz in state selection, we can see the frequency is scanning through different Zeeman states, as expected. The magnetic field along the pumping beam is also further increased to make a larger difference between Zeeman states during adiabatic rapid passage and therefore better efficiency, as shown in figure 3.34. The atoms after Raman sideband

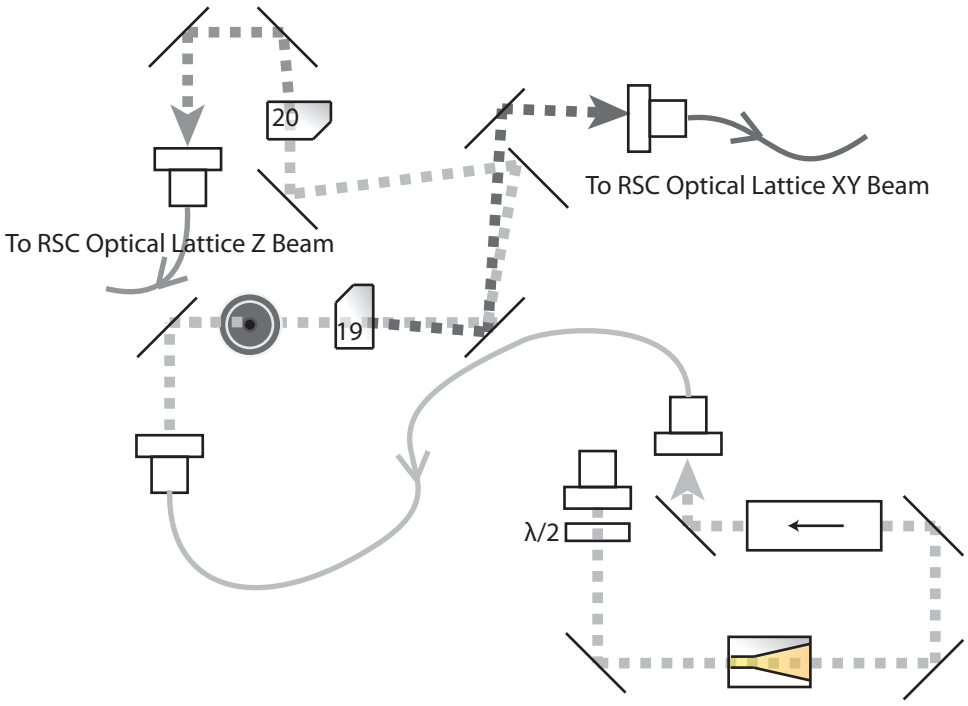

Figure 3.33: Experimental setup of laser preparation for Raman sideband cooling. Frequency components are shown in figure 3.16b.

cooling are in $F = 3$ state, which is changed to $F = 4$ after adiabatic rapid passage. An additional Raman transition pulse for state selection is added to select favored atoms with $m_{\mathrm{F}} = 0$ state and therefore the selected atoms are in $F = 4$ state again, which is the same as the original setup.

Figure 3.35 shows the time of flight fluorescence signal of atoms before and after Raman sideband cooling. The signals can be two to three times higher than the bare fountain. After Raman sideband cooling, adiabatic rapid passage has efficiency of about 50%, which is about five times higher than the original state selection using a Raman transition. Because the temperature after Raman cooling is lower, the atoms will see a more uniform pulse intensity profile during velocity selection, which yields twice the efficiency ($\sim$ 20%) compared with the original one. Overall, Raman sideband cooling can increase the signal by about twenty to thirty times. The temperature can also be estimated as less than 500 nK, which is about two times better than the bare fountain.

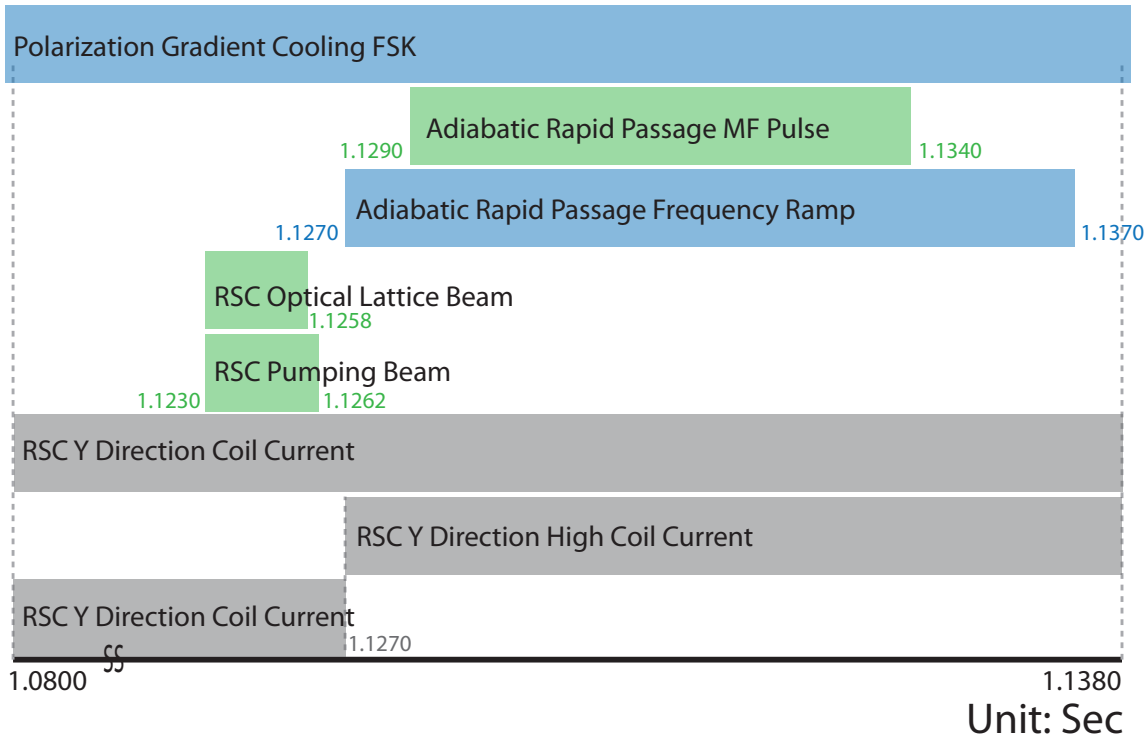

Figure 3.34: Time sequence in Raman sideband cooling. The timing depends on the velocity of the atoms and also the position of the optical lattice. Here MF stands for microwave frequency.

3.14 Bloch oscillations

In our case, Bloch oscillations can be viewed as a modification of Bragg diffraction, as shown in section 2.6. The difference is whether there is a frequency ramp or not. For atoms with momentum $2n\hbar k$, the related Doppler shift will be

$$\frac{2n\hbar k}{m}\frac{1}{c}\omega_{\mathrm{L}} = \frac{2n\hbar k^2}{m} = 4n\omega_{\mathrm{r}}. \tag{3.2}$$

This value is for one laser beam. For moving optical lattices, the frequency difference between the two beams should satisfy $8n\omega_{\mathrm{r}}$ to load atoms with $2n\hbar k$ momentum. For demonstration of Bloch oscillations, we can replace the stable frequency of Agilent 3320A which drives AOM17 in figure 3.15 with a linear frequency ramp, which changes the two-photon frequency difference of the counter-propagating beams. The two-photon frequency difference is chosen as to satisfy the requirement of $8n\omega_{\mathrm{r}}$ as just mentioned. A result of a Bloch oscillations is shown in figure 3.36. Bloch oscillations can have $\sim 45\%$ efficiency for a momentum transfer of $\sim 250\hbar k$. We define n' in this case as ~ 125, which is analogous to the Bragg order n.

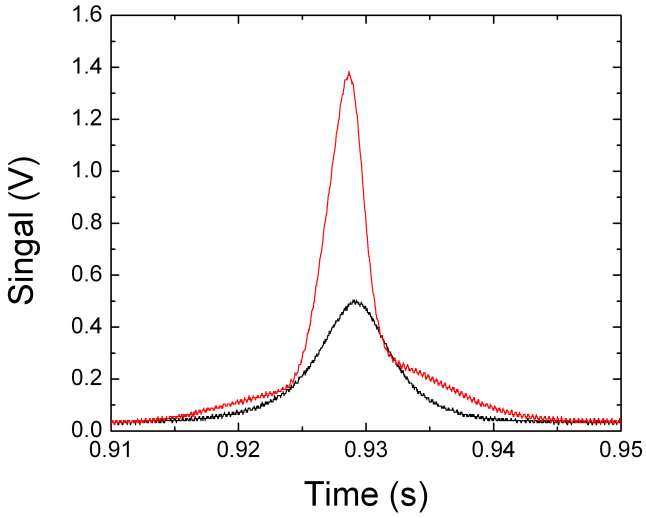

Figure 3.35: Comparison between bare fountain (black line) and fountain plus Raman sideband cooling (red line) signals.

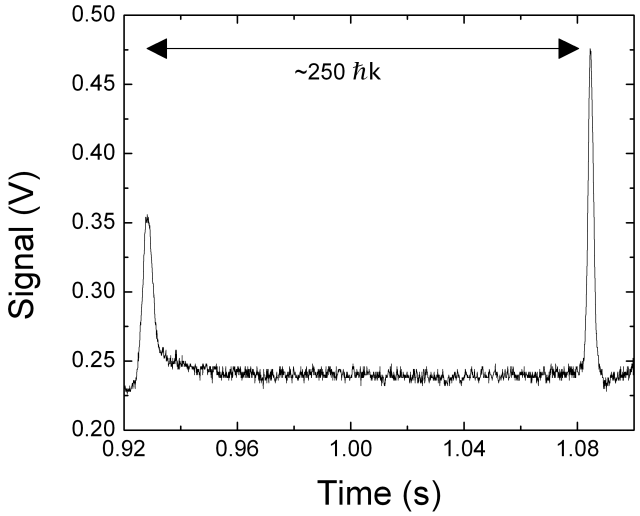

Figure 3.36: Demonstration of Bloch oscillations. The x coordinate is the time, and y axis is the signal of the atoms detected by PMT.

In the measurement of the recoil frequency, we insert Bloch oscillations between the second and the third Bragg diffraction pulse, as shown in figure 3.37. The time sequence is shown in figure 3.24. Bloch oscillations start 5 ms later than the second Bragg diffraction pulse. The pulse is 900 μs long and the ramping rate is about 4.967 Hz in 0.013 μs. To

satisfy the adiabatic condition, the shape of the pulse is generated by another Agilent 3320A function generator with 70 μs rising edge and falling edge. The frequency ramp starts 90 μs after the start of the pulse. Bloch oscillations work on both branches of the conjugate Ramsey-Bordé interferometers. Therefore, we drive two Bloch oscillations simultaneously to separate the atoms further. Because they change both arms in one Ramsey-Bordé atom interferometer at the same time, we do not worry about the beam splitter phase, since it will be a common mode phase and can be removed by our scheme. The measured angular frequency ω_{m} after performing Bloch oscillations is no longer the same as in equation (2.50), but

$$\omega_{\mathrm{m}} \approx 8(n' + n)\omega_{\mathrm{r}}. \tag{3.3}$$

The result can be derived from the similar methods discussed in section 2.2, 2.3.

For generating the required two-photon frequency difference δ, we switch the constant ω_{m} in section 3.9 with a linear ramping frequency during Bloch oscillations. The two-photon frequency difference in the initial two Bragg diffraction pulses with order n is $\omega_{\mathrm{b}} = 4n\omega_{\mathrm{r}}$, as shown in equation (2.104). At the beginning of Bloch oscillations, the values of δ should be $4n\omega_{\mathrm{r}} - 4n\omega_{\mathrm{r}} = 0$ and $4n\omega_{\mathrm{r}} + 4n\omega_{\mathrm{r}} = 8n\omega_{\mathrm{r}}$ to load atoms with 0 and $2n\hbar k$ momentum state, respectively. At the end of Bloch oscillations, assuming the angular frequency is from $\pm 4n\omega_{\mathrm{r}}$ to $\pm 4\tilde{n}\omega_{\mathrm{r}}$, δ will be $4(n - \tilde{n})\omega_{\mathrm{r}}$ and $4(n + \tilde{n})\omega_{\mathrm{r}}$, and corresponds to momentum $\hbar k(n - \tilde{n})$ and $\hbar k(n + \tilde{n})$, respectively.

The frequency ramp is generated by Analog Devices card AD9959, which is ramped from 4.041325985 MHz to 4.305819019 MHz. It will be mixed with 4 MHz and passed through a low pass filter. The extra 4 MHz is used to make higher harmonics filtering easier. After passing the filter, the frequency will go from $\approx$ 41 KHz ($\tilde{n} = 5$) to $\approx$ 306 KHz ($\tilde{n} = 37$). This corresponds to momentum from $0\hbar k$ and $10\hbar k$ to $-32\hbar k$ and $42\hbar k$, with a momentum transfer of $32\hbar k$ for both arms. It corresponds to $n' = 16$, which is chosen as a balance between high sensitivity and good contrast.

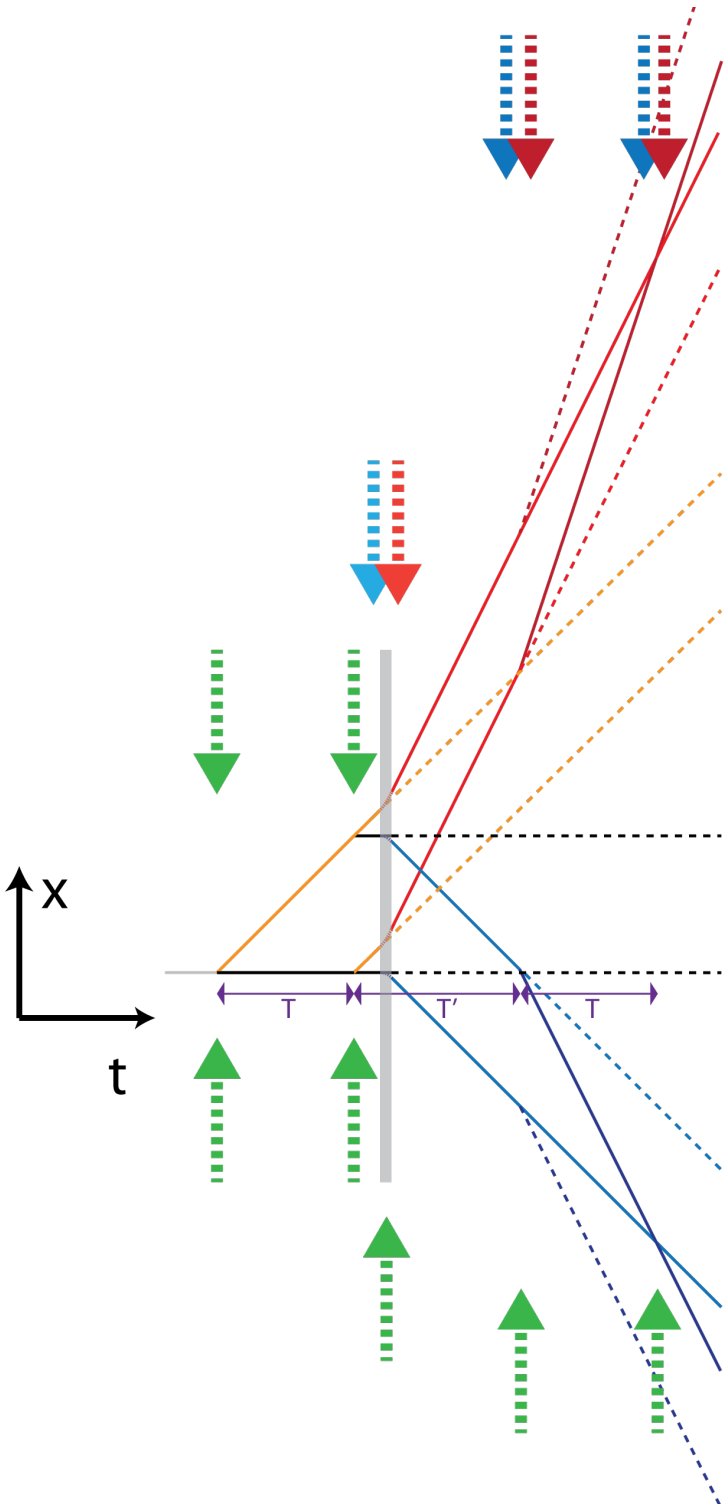

Figure 3.37: Atom interferometer with extra Bloch oscillations. Symbols are similar as in figure 2.2. Extra Bloch oscillations occur in the grey region.

Chapter 4

Result

4.1 Coriolis force compensation

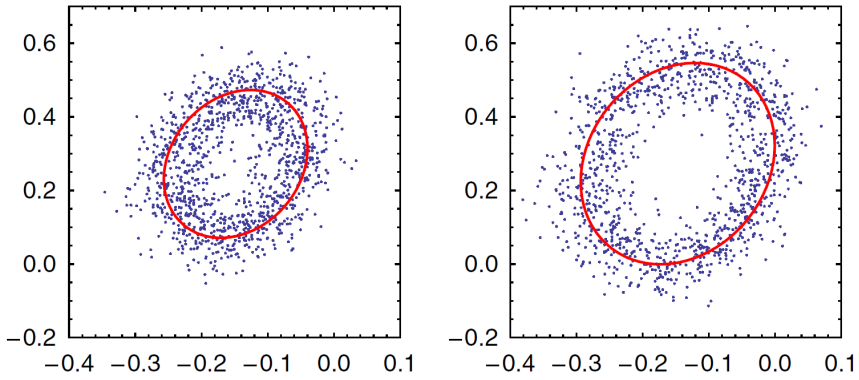

Figure 4.1: Comparison before (left) and after (right) the Coriolis force compensation. The x axis and y axis are the population ratios from two fringes. Blue spots show the data taken, and red solid lines show fitting results.

Figure 4.1 demonstrates the difference in contrast before and after the Coriolis compensation, in the $n = 5$ and $T = 160$ ms case, without Bloch oscillations and Raman sideband cooling. The data with correct compensation shows improvement of the overall contrast. Figure 4.2 shows the contrast as a function of the tip-tilt rotation rate around the y' axis for various pulse separation times. A Gaussian function of the rotation rate (with the center Ω_{opt}, width σ_Ω, amplitude and offset as fit parameters) fits the data within the standard error. The fit results are tabulated in table 4.1. A weighted average for the optimum tip-tilt rotation rate is $\Omega_{\text{opt}} = 51.3 \pm 0.8$ μrad/s. We also performed a similar measurement for the x' axis, as shown in figure 4.3. From both measurements, we compute the magnitude of the rotation rate, which is 58.5 ± 1.0 μrad/s (taking into account the actual angle of 82° between x' and y'). This agrees with $\Omega_\oplus \cos\vartheta = 57.4$ μrad/s within $\sim 1\sigma$ error.

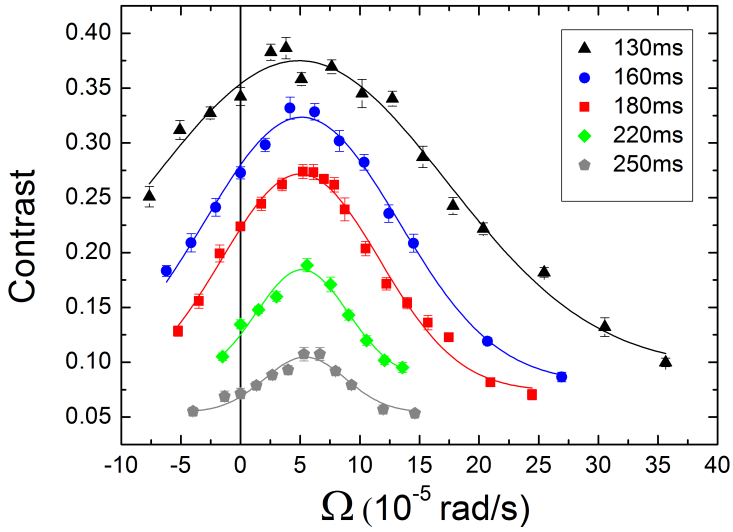

Figure 4.2: Contrasts versus mirror rotation rates along y' axis under different time separation T. The x' axis rotation rate is fixed at -26.2 μrad/s.

T(ms)	$\Omega_{\text{opt}}(\mu\text{rad/s})$	σ_Ω(nm)	σ(nm)
130	49 ± 4	124 ± 8	106 ± 7
160	51 ± 2	81 ± 4	105 ± 5
180	50 ± 2	66 ± 3	108 ± 5
220	52 ± 2	38 ± 5	92 ± 12
250	54 ± 2	34 ± 4	107 ± 13

Table 4.1: Fitting results for the Coriolis force compensation. The parameters Ω_{opt} and σ_Ω are the fitting center and width from figure 4.2. The value of σ is calculated from σ_Ω and equation (2.118).

The experiment validates the model shown in section 2.8. From the mismatch of the final beam splitter and the result in contrast loss, we can estimate the wavepacket size in all three directions. According to table 4.1, the measured widths of the overlap integral agree with one another for all measured T. From the data, we can determine the parameters of the overlap integral. The symmetry of the atomic fountain suggests that the principal axes of the matrix A from equation (2.118) coincide with the x, y, z laboratory rotatory frame. In what follows, we neglect the small difference in the x, x' and y, y' directions. The weighted average of the numbers in the last column of table 4.1 is $\sigma_{\text{x}} = 105 \pm 3$ nm. The fit shown in figure 4.3 yields $\sigma_{\text{y}} = 86 \pm 7$ nm. To determine σ_{z}, we vary the time interval between T_3 and T_4 (the definition are in section 2.8), see figure 4.4. The fitted width corresponds to $\sigma_{\text{z}} = 813 \pm 21$ nm. This much larger width demonstrates the validity of velocity selection.

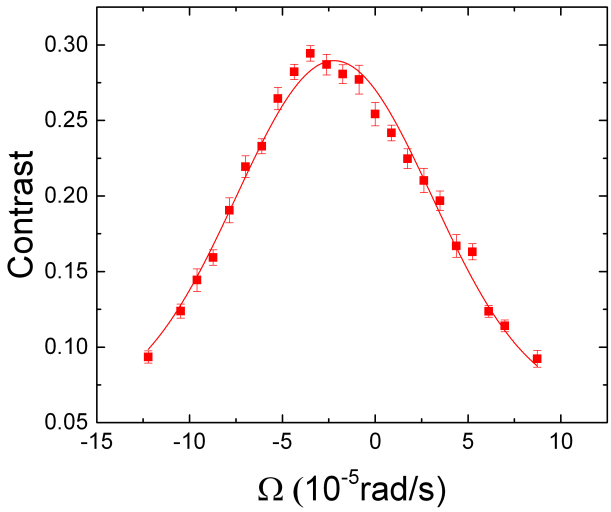

Figure 4.3: Contrasts versus rotation rates in x' axis. The y' axis rotation rate is fixed at 69.8 μrad/s.

Because each atom interferes only with itself, these measured quantities are properties of individual atoms, averaged over the atomic ensemble. They need not be related to the temperature of the ensemble.

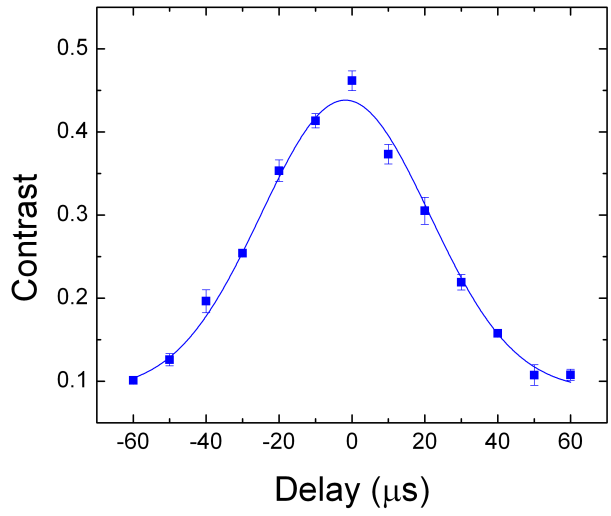

Figure 4.4: Contrasts versus mismatch along z axis.

4.2 Compton clock

The difference between a working Compton clock and a recoil frequency measurement is shown in figure 4.5. The first 10 data points are taken in for a comb multiplication factor of N_c. At the 11th data point we briefly disable the feedback, so that ω_{cryst} is free-running and the experiment is running as a Ramsey-Bordé recoil measurement. The measured recoil frequency is proportional to $\omega_L^2 = (N_c\omega_{cryst})^2$. If we increase N_c by 100 ppb, we obtain a 100 ppb increase in ω_L. Thus, a 200 ppb increase in ω_m is observed. Starting with the 13th data point, we close the feedback loop again. Once the feedback turns on, the closed loop adjusts the frequency ω_{cryst} of O1 to maintain zero phase difference. From equation (2.106), we know that $N_{DDS}\omega_{cryst} = \omega_m = \omega_0/4nN^2 = \omega_0 N_{DDS}^2/4nN_c^2$. The value of ω_m is thus inversely proportional to N_c^2. We therefore expect the measured frequency to decrease by 400 ppb, so that it ends up 200 ppb lower, which is indeed what observed. In a Compton clock, the recoil frequency ω_m is thus conjugate to the angular laser frequency ω_L and keep the Compton frequency ω_0 constant.

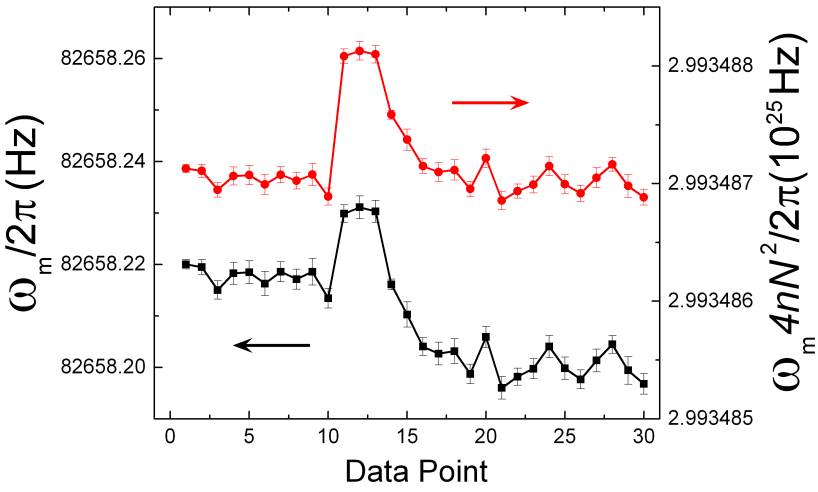

Figure 4.5: Comparison between a Compton clock and a recoil frequency measurement. The black line shows the measured frequency without considering the influence of laser frequency. The red line shows the result with laser frequency compensation and therefore is related to Compton clock oscillation.

Quantitative agreement is demonstrated by comparing the rest-mass stabilized frequency ω_{cryst} to a rubidium frequency standard (SRS FS725) over 6 hours, as shown in figure 4.6. It averages to 9 999 998.127 Hz with a standard deviation of the mean of 0.015 Hz. A chi-squared test yields a normalized $\chi^2 = 1.4$. Our statistical uncertainty is 0.015 Hz $\times (\chi^2)^{1/2} =$ 0.018 Hz, or 1.8 ppb. The Allan deviation, show in figure 4.7, is below $10^8/[t/(1000s)]^{1/2}$,

Systematic error term	Correction for $\omega_m/2\pi$ (Hz)	Ratio (ppb)
Constant Phase Shift	0.02814 ± 0.00026	340.4 ± 3.1
Gravity Gradient Shift	-0.00121 ± 0.00007	-14.7 ± 0.9
Gouy phase	0.000016 ± 0.00001	1.9 ± 0.1
Beam Alignment	-0.00012 ± 0.00009	-1.5 ± 1.1

Table 4.2: Systematic errors for the Compton clock measurement.

where t is the integration time. Using equation (2.104) and correcting for systematic effects, we obtain the Compton frequency $\omega_0/2\pi = (2993486252 \pm 12) \times 10^{16}$ Hz. The deviation from the expected values is -5.2 ± 4.0 ppb and is consistent with zero within 2σ [13]. We will discuss systematic effects in section 4.3. From the Compton frequency, we can also calculate the fine structure constant and get the value as $\alpha^{-1} = 137.03599872(28)$, with uncertainty of 2.0 ppb.

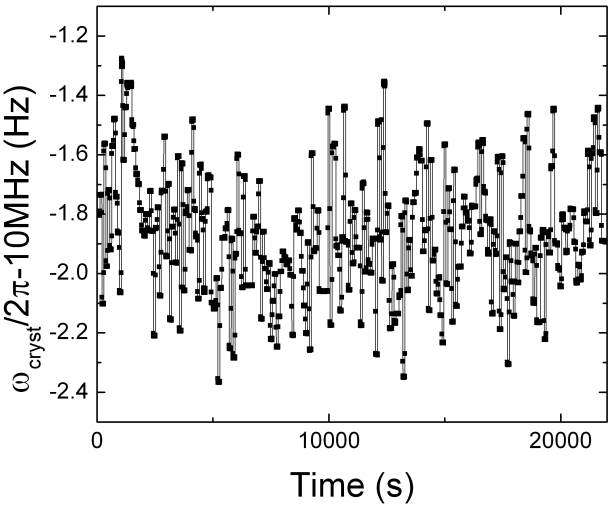

Figure 4.6: Six hour data set for the Compton clock measurement.

4.3 Systematic error

Here we discuss the leading systematic errors in measuring the Compton frequency and the fine structure constant. Values of these errors can be found in table 4.2.

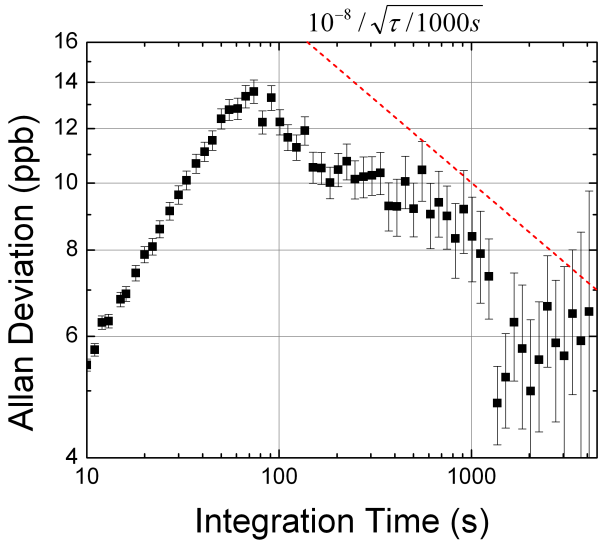

Figure 4.7: Allan deviation for the Compton clock data. The slope before $t = 100$ s is an artifact of the 80 s update cycle of the experiment.

4.3.1 Gravity gradient

The gravity gradient γ value is $(3.4 \pm 0.2) \times 10^{-6}/\mathrm{s}^2$, measured nearby in Palo Alto, CA [42]. It causes a fractional shift in ω_m of $(\gamma/12)(2T^2 + 3TT' + 3T'^2)$, as discussed in section 2.9. For Compton clock measurement, $T = 160$ ms and $T' = 2$ ms, whose value $\approx 14.7 \pm 0.9$ ppb.

4.3.2 Constant phase shift

When measuring ω_m, its value will be different at different T. When plotting its value versus a reciprocal time scale, the resulting fit is close to a straight line, which is what we called the one over T effect. This property hints that the difference in measured ω_m may come from a constant phase shift error ϕ_err. Once there is a constant phaseshift, the measured frequency will differ from real frequency in a reciprocal time scale tendency, like

$$\omega_\mathrm{m} T = 8n\omega_\mathrm{r} T - \phi_\mathrm{err}, \tag{4.1}$$

$$\omega_\mathrm{m} = 8n\omega_\mathrm{r} - \frac{\phi_\mathrm{err}}{T}. \tag{4.2}$$

The value of ϕ_err can be estimated by the slope of the data fitting. Once ϕ_err is obtained, ω_m should be corrected correspondingly. Therefore the fitting error of ϕ_err will influence the overall uncertainty we can obtain in the recoil frequency measurement, and then the fine structure constant measurement and the Compton clock. In the Compton frequency measurement, data is taken at different T from 2 ms to 160 ms. It determines the size of the effect to be 340.4 ± 3.1 ppb for $T = 160$ ms, as shown in figure 4.8.

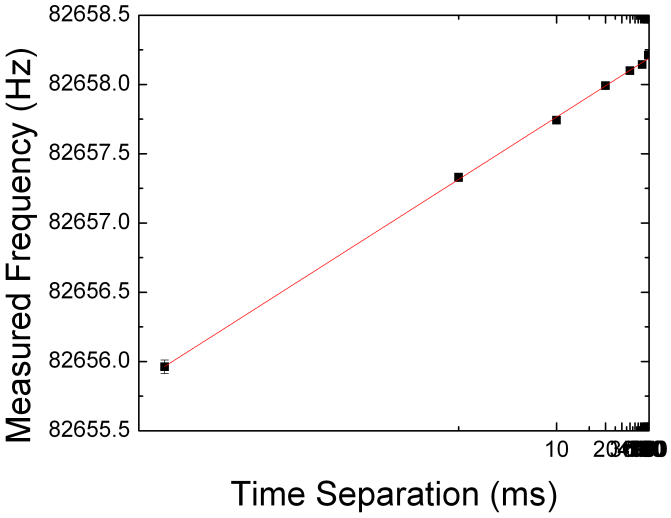

Figure 4.8: One over T effect in the Compton frequency measurement.

Since ϕ_{err} does not depends on T, a reasonable suggestion of this error source will be beam splitters. When we decrease the Bragg diffraction pulse amplitude, the measured ϕ_{err} will become lower, as shown in figure 4.9. It verifies the assumption that ϕ_{err} should mostly originate from the beam splitters.

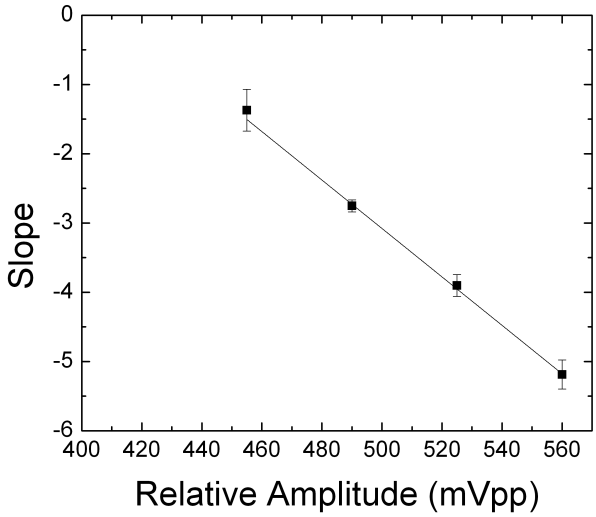

Figure 4.9: One over T versus Bragg diffraction pulse amplitude. In the experiment, the zero slope corresponds to almost zero contrast.

When we consider beam splitters more carefully and do some simulations, the theoretical discussions in section 2.6.1 shows a possible source of ϕ_{err}. Comparison of equation (4.2) and equation (2.102) shows the similarity between ϕ_{err} and $\delta\phi_{\text{cross}} + \delta\phi_{\text{non-ideal}}$. The value of $\delta\phi_{\text{cross}}$ in $n = 5$ is given by $\sim 1.23°$. Experimental data shows the sign of measured one over T errors are insensitive to blue or red single photon detuning, as shown in figure 4.10. The independence indicates this effect is not sensitive to the AC stark shift, therefore justify our assumption of the adiabatic condition for calculations in section 2.6.1.

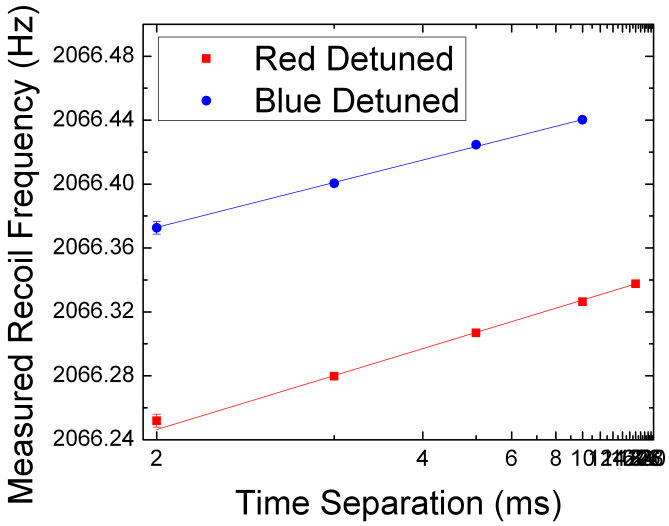

Figure 4.10: One over T versus single photon detuning. Because different single photon detuning corresponds to different wavelength, the measured recoil frequency $(\omega_{\text{m}}/8n)/2\pi$ will be different. But the slopes of fitted lines are similar.

The value of $\delta\phi_{\text{non-ideal}}$ can be estimated from the finite velocity distribution of atoms after velocity selection. For a 150 μs velocity selection pulse, the frequency width of atoms is about 3 ω_{r}. Comparing with figure 2.12, we can estimate the introduced phase deviation $\delta\phi_{\text{non-ideal}}$ to be $\leq 1°$. Combined with $\delta\phi_{\text{cross}}$, the overall phase shift is $\leq 2.23°$. Compared to the experiment result $\sim 1.6°$, the theory overestimates the phase shift by about $\leq 39\%$, which may be explained by two things. First, Bragg diffraction itself can work as one kind of velocity selection. Atoms being diffracted by Bragg diffraction will have a narrower velocity distribution. Second, the detected signals of falling atoms are related to a convolution between atom's position distribution and velocity distribution. If we mainly focus on the peak amplitude of the signals, as what we do in the experiment, then we select atoms with a narrower velocity distribution.

The comparison between experimental data and calculations with various pulse amplitudes (figure 2.11) is shown in figure 4.11. The measured value varies less compared with the calculations, which can be explained by the transverse Gaussian profile of the beam split-

ter pulse. Atoms with different position will see different intensity and the detected signal takes the average over the entire transverse plane. Some of the positive phase deviation can be canceled out by the negative phase deviation part, which results in a more uniformer deviation versus amplitude.

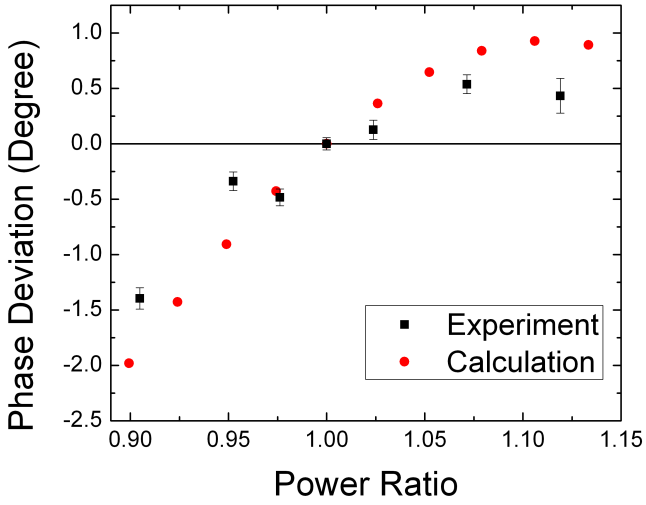

Figure 4.11: Comparison between calculated values and experimental data for the one over T effect with different pulse amplitude. The experimental data is taken at $n = 4$, $T = 2$ ms with 35 μs half width of the Bragg diffraction pulse.

We can also compare the result from calculations (figure 2.12) with experimental data with different two-photon detuning, as shown in figure 4.12. The two results agree with each other pretty well. The asymmetry in experimental data may come from the perturbation of other Bragg orders, since the pulse is not resonant.

To reduce this phase shift error, one solution is to use longer velocity selection pulses, which can bring down $\delta\phi_{\text{non-ideal}}$ with the trade off of smaller signals. The other way is to use Bloch oscillations to enlarge the momentum separation between the conjugate atom interferometers while retaining the same Bragg diffraction order, therefore suppressing the phase from possible extra multi-photon transitions ($\delta\phi_{\text{cross}}$), as suggested in figure 2.9. We can also try to increase ω_{m}. Because ϕ_{err} is a fixed value, the higher overall phase will correspond to the lower relative uncertainty comes from this error.

4.3.3 Gouy phase

A laser beam of finite $1/e^2$ intensity radius w_0 exhibits an additional phase shift (Gouy phase) when going through its Rayleigh range, which corresponds to a relative increase in its effective wavenumber by $\lambda^2/(\pi^2 w_0^2)$. In our case, the waist is determined by blade method,

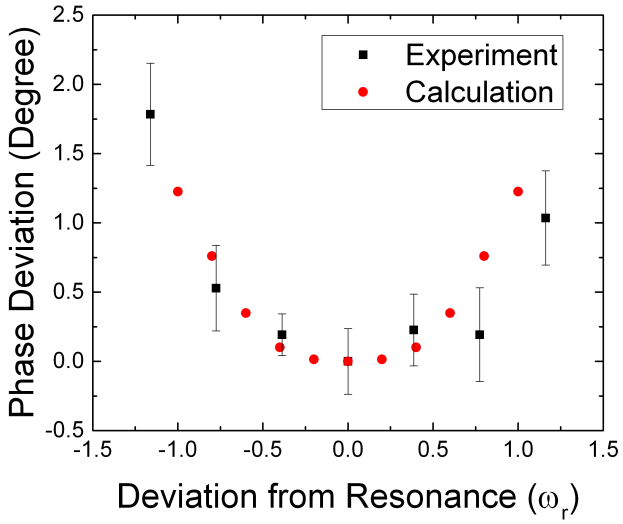

Figure 4.12: Comparison between calculated values and experimental data for the one over T effect with different two-photon detuning. The experimental data is taken at $n = 5$, $T = 40$ ms with 35 μs half width of the Bragg diffraction pulse.

as shown in figure 4.13. The result is $w_0 = 6.18 \pm 0.15$ mm and corresponds to 1.9 ± 0.01 ppb error in the recoil frequency measurement.

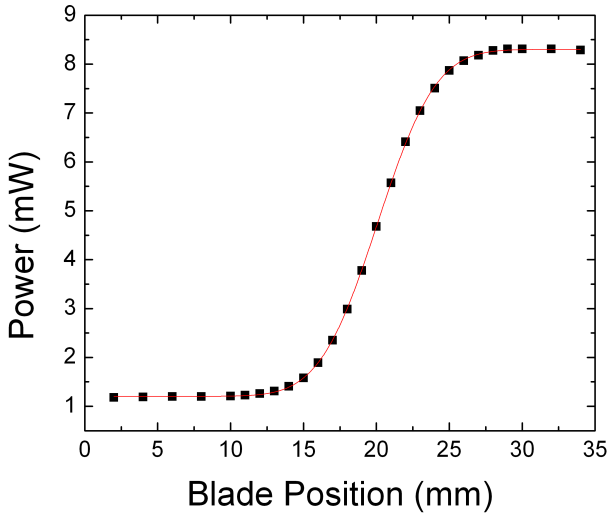

Figure 4.13: Measurement of the beam profile. The y axis is the power measured after the razor blade, and the x axis is the relative position of the razor blade. The black squares are data taken, the red line is the fitting result of a error function.

4.3.4 Beam alignment

Misalignment of the counter-propagating beams relative to each other by an angle θ reduces the effective wavenumber from $k_{\mathrm{eff},0} = (k_1 + k_2)/2$ to $k_{\mathrm{eff}} = k_{\mathrm{eff},0}(1 + \cos\theta)/2$. We verify counter propagation by testing whether the retro-reflected beam re-couples into the single-mode optical fiber that launches it. Theoretically, a 1/e reduction of the back-coupling efficiency results from a $\lambda/(\pi w_0) = 75$ μrad misalignment which, in turn, causes a 2.8 ppb reduction in ω_{m}. In practice, however, we found the sensitivity of this method to be lower, probably due to beam distortions, as shown in figure 4.14. The smallest angle we can reliably rule out is 66 μrad. Since no such deviation is observed, we assume that the beam points into a random direction within a circle of 66 μrad radius, and correct ω_{m} by -1.5 ± 1.1 ppb.

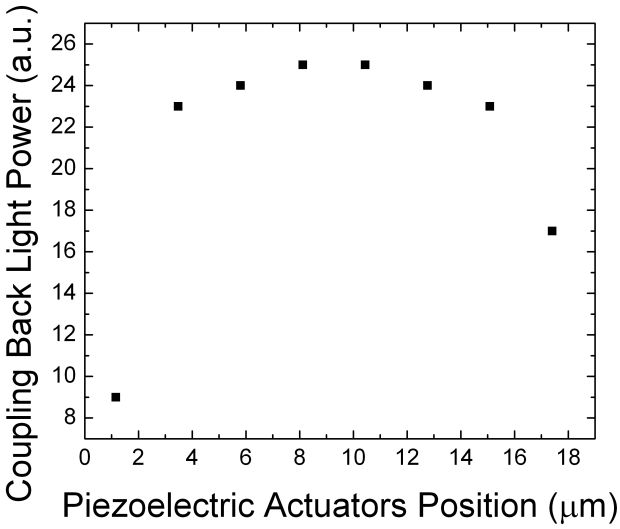

Figure 4.14: Backward fiber coupling efficiency for different top mirror alignments.

4.4 Improved result

Here we demonstrate the improvements in measuring the recoil frequency after implementing Raman sideband cooling and Bloch oscillations.

4.4.1 Sensitivity achievement

After the implementation of Raman sideband cooling and Bloch oscillations, the sensitivity showed improvement. After six hours of data taking, as shown in figure 4.15, in which $n = 5$, $n' = 16$, and $T = 80$ ms, the sensitivity of the recoil frequency measurement can achieve 0.96 ppb in six hours with preliminary data analysis, which is about two times higher than what

was achieved in the Compton clock measurement. The Allan deviation, shown in figure 4.16, also shows a lower noise floor than in the Compton clock measurement, as shown in figure 4.7.

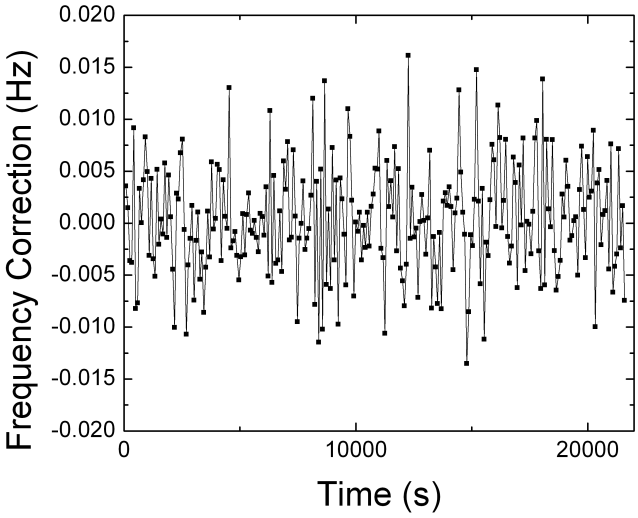

Figure 4.15: Six hour data set for the improved recoil frequency measurement.

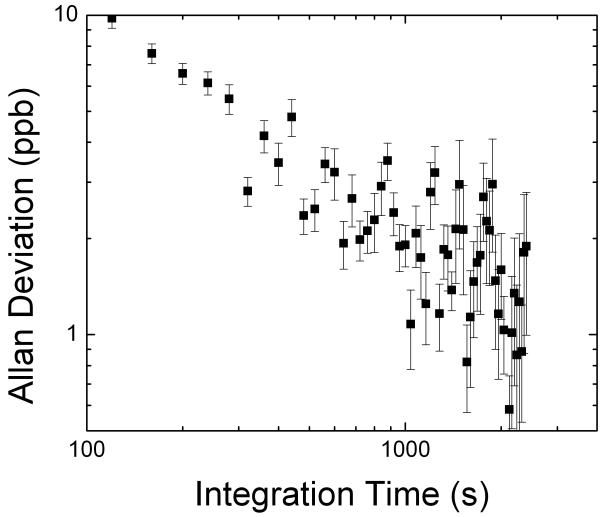

Figure 4.16: Allan deviation for the improved recoil frequency measurement.

The data can be analyzed with different ellipse fitting parameters, as shown in figure 4.17. We obtain a better result of 0.66 ppb uncertainty for the recoil frequency measurement

with bin size equals to 90. The number of bin size corresponds to how many data points are required to fit an ellipse. Larger bin size will lead better fitted ellipses, but will reduce the number of fitted ellipses and may increase the overall error. Our default setting for bin size is 20.

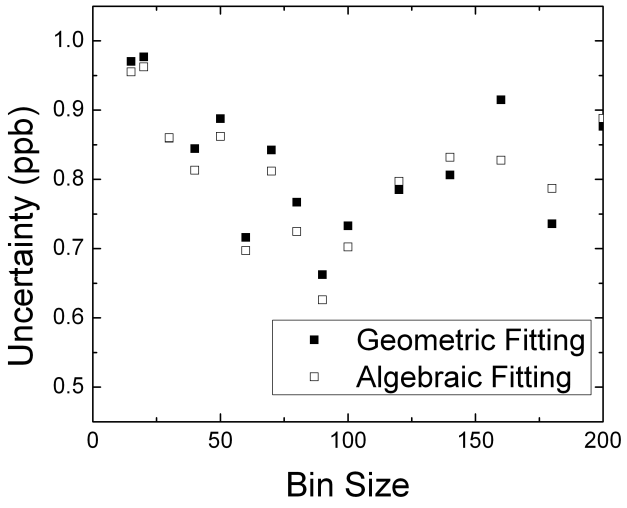

Figure 4.17: Uncertainty under different bin size and different fitting methods. Solid squares show results for the geometric fitting method, and the unfilled squares show results for the algebraic fitting method.

4.4.2 Constant phase shift after implementing Bloch oscillations

Once we implemented the combination of Bloch oscillations and Bragg diffraction, the decrease of the phase error amplitude is significant, as shown in figure 4.18, with a correction of about 44.8 ± 1.2 ppb at $T = 80$ ms.

As suggested in section 4.3.2, Bloch oscillations will mostly reduce $\delta\phi_{\text{cross}}$, which is about 1° of the overall 1.6° phase error ϕ_{err}. Therefore the implementation of Bloch oscillations should reduce the amount of ϕ_{err} (slope in the figure 4.18) to about one-third of the original value, which is what we observe.

However, the fitting itself sometimes deviates from a straight line, as shown in figure 4.19. The deviation correlates to the contrast, as shown in figure 4.20, with a dip happening at 20 ms time separation. In figure 4.19, the measured frequency also deviates from the expected straight line at 20 ms time separation. A first guess would be some external noise at range $1/\ 20$ ms ~ 50 Hz, but the contrast does not drop at higher harmonics of the supposed noise frequency. Another guess would be some local perturbations which happen in the chamber and result in the discrepancy. We check this assumption by shifting the overall time sequence

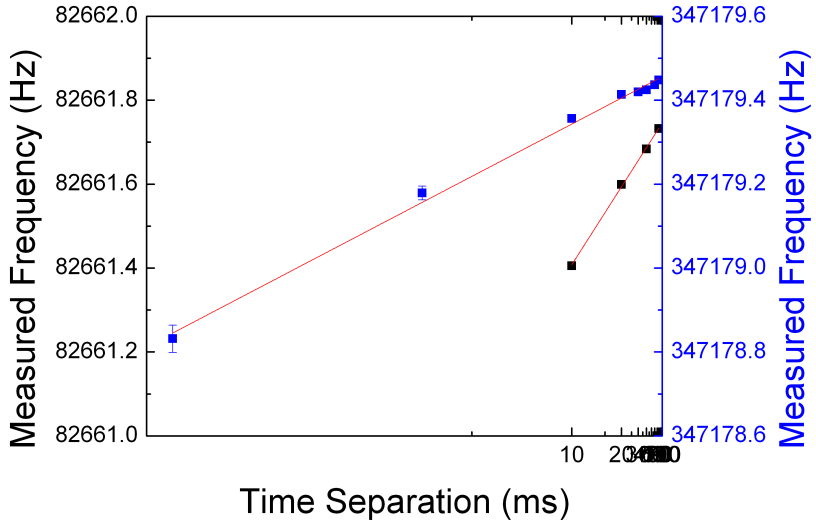

Figure 4.18: Comparison of one over T before and after Bloch oscillations. The blue axis and points represent the result after implementing Bloch oscillations, and the black axis and points represent the original result. The two coordinates in y axis are chosen to have the same 1 Hz interval to make the comparison easier.

80 ms later to compare the results, as shown in figure 4.21. From the data it appears that the deviation does not originate from local perturbations.

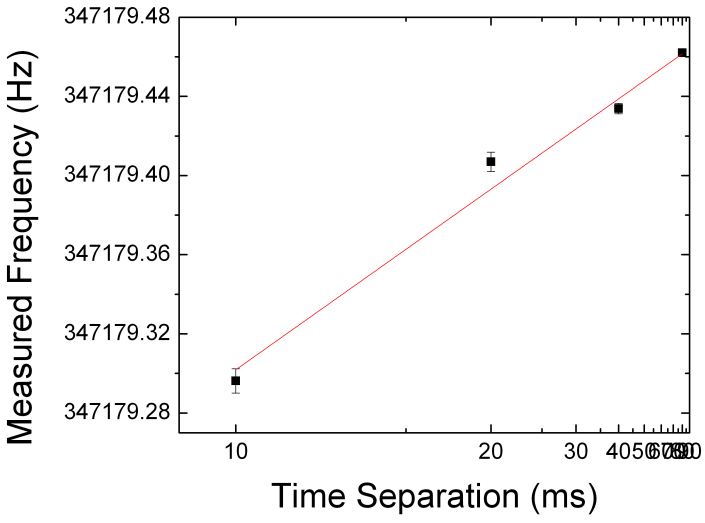

Figure 4.19: Demonstration of the deviation from a straight line in one over T. Here the measruement is made in blue detuned $\Delta = 12$ GHz case.

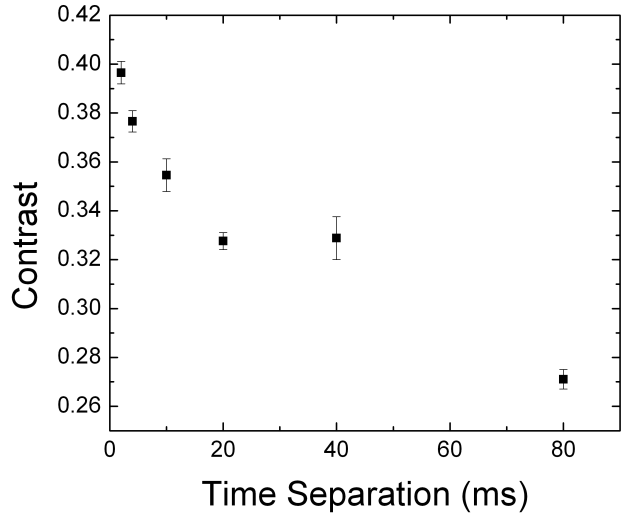

Figure 4.20: Contrast versus time separation. There is a drop in contrast around $T = 20$ ms.

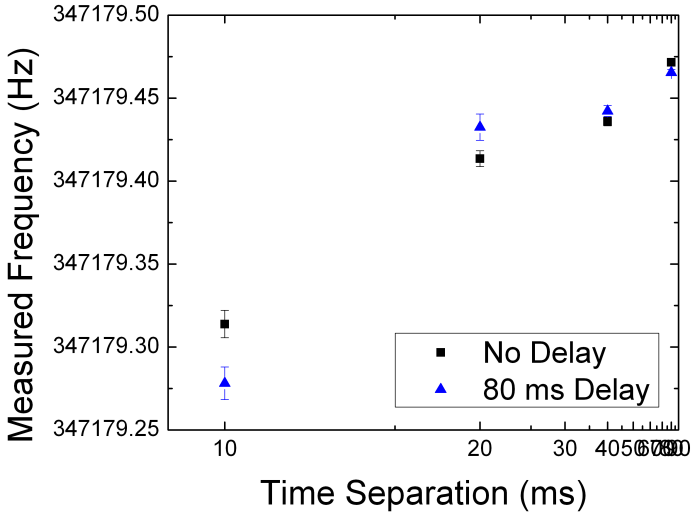

Figure 4.21: Comparison of the deviation from a straight line in one over T with different starting times. The black square show the results of a regular atom interferometer time sequence, and the blue triangles show the results of delaying the atom interferometer time sequence by 80 ms.

After ruling out the possibility of environmental perturbations, what remains is some hidden mechanism inside the experiment. The external magnetic field does not influence

the deviation significantly, as shown in figure 4.22, where we change the solenoid current to six times higher and compare the resulting one over T deviation. The result excludes the possibility of extra transitions involving Zeeman states as the main factor of this deviation. Figure 4.23 shows the deviation depends on the sign of single photon detuning, highlighting the role of the beam splitter. This deviation happens even when there are no extra Bloch oscillations, as shown in figure 4.24. That means if the deviation source comes from the beam splitters, it is mainly due to Bragg diffraction.

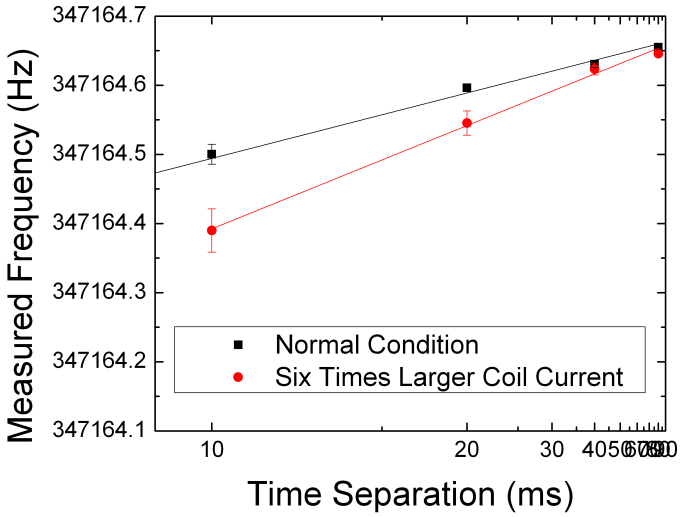

Figure 4.22: One over T effect deviation for different external magnetic fields.

The deviation of one over T will limit our overall uncertainty in measuring the recoil frequency. However, the consistency of the deviation in the experimental data suggests that we might be able to simulate it by further considerations of Bragg diffraction, including more energy levels, non-adiabatic condition, and space-time wavepacket simulations.

4.5 Contrast loss

Here we discuss some possible ways for the contrast to decrease. The contrast loss will diminish the signal to noise ratio and can limit the uncertainty of the measured value.

4.5.1 Thermal expansion

For atoms with finite temperature, the extra transverse velocity distribution will change the atoms' transverse position during the atom interferometer process, therefore the atoms will see the same beam splitter pulse as different intensity at different times. The various pulse amplitude will contribute to different beam splitter efficiencies and therefore decrease the

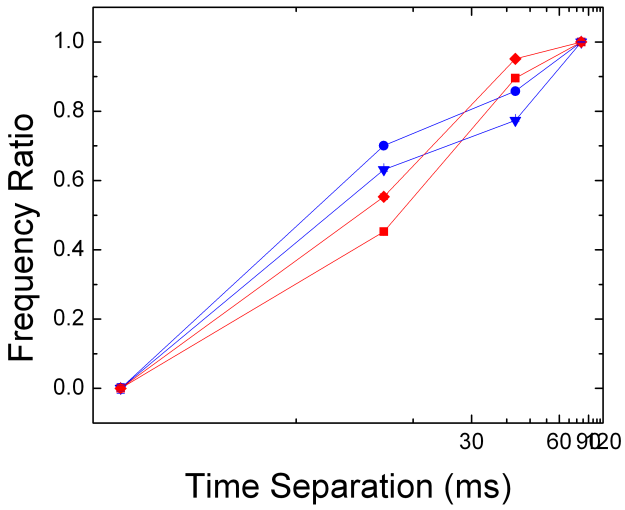

Figure 4.23: One over T effect deviation with different Δ. The blue and red lines are the results for the blue and red detuned case, respectively. The y axis shows the normalized ratio, which is supposed to be a straight line in the ideal one over T case.

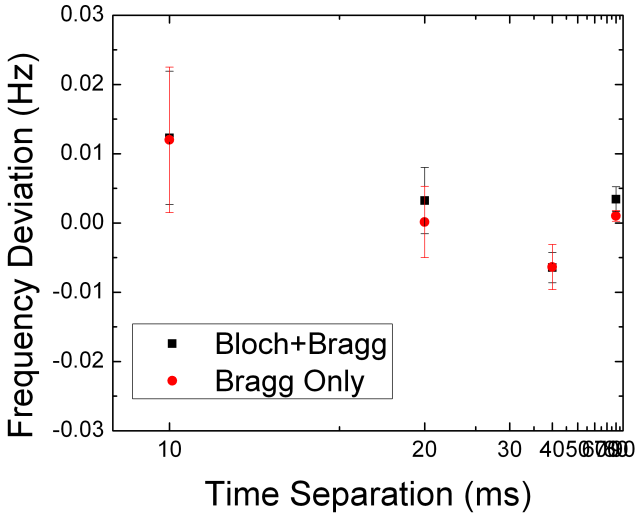

Figure 4.24: One over T effect deviation with different atom interferometer beam splitter configurations. Black squares represent the case of Bragg diffraction and Bloch oscillations, and red circles represent the case of Bragg diffraction only. Because ω_{m} is different in each case, only the deviation from the one over T straight line is plotted.

overall contrast, since for the ideal case maximum contrast will only be achieved under the condition of having all beam splitters equal.

4.5.2 Coriolis force effect

Without Coriolis force compensation, the drop of contrast can be calculated from equation (2.118). The Coriolis force compensation actually should be implemented with two mirrors. However, the first order compensation is already good enough at the time separation and momentum difference we use.

4.5.3 Wavefront distortion

The surface quality of all the optical components after the beam splitter fiber port, including mirrors, wave plates and windows may affect the overall signal contrast. Laser beams passing through an uneven surface will obtain inhomogeneous phase distribution among the profile, so called wavefront distortion. Atoms at different position will therefore obtain different phase value from photons. Vibrations of the optical components and the thermal expansion of the atom cloud will make this additional phase not the same at each beam splitter and therefore add noise into the measured ellipse, which decreases the overall contrast. Our vacuum chamber window has the surface quality of $\lambda/10$, which is worse than the mirrors and waveplates with $\lambda/20$ unevenness and dominates the wavefront distortion effect.

The contrast may improve for the retro-reflected mirror setup, since one optical window is removed. Moreover, every time an atom obtains a transverse position-dependent phase from absorbing photons, the same phase will be removed by simultaneous emission of the same photons which are retro-reflected back. However, the extra quarter waveplate to satisfy the Bragg diffraction polarization requirement and the retro-reflected mirror both have its own surface unevenness, and will still cause some contrast drop.

4.5.4 Wall-scattered light

We can change the fiber port size for Bragg diffraction, making the pulse more homogeneous in space. However, the overall effect may not be better. There are two things we are mainly concerned with when switching from a medium sized fiber port to a big one. One thing is the available optical intensity. For the larger size fiber port we need the roughly double optical power to drive the same beam splitter, which may exceed of maximum available titanium-sapphire laser power. The other issue is wall scattered light. In our experiment, the larger size fiber port does not always guarantee better performance. Sometimes the contrast is lower for larger beam sizes. We can demonstrate this effect by putting an iris just after a large fiber port. When the iris gets a little smaller, the contrast actually gets higher, as shown in figure 4.25. When the iris further closes, the contrast gets smaller again, and this time we can view the diffraction pattern on the top charge-coupled device (CCD) camera, as shown in figure 4.26.

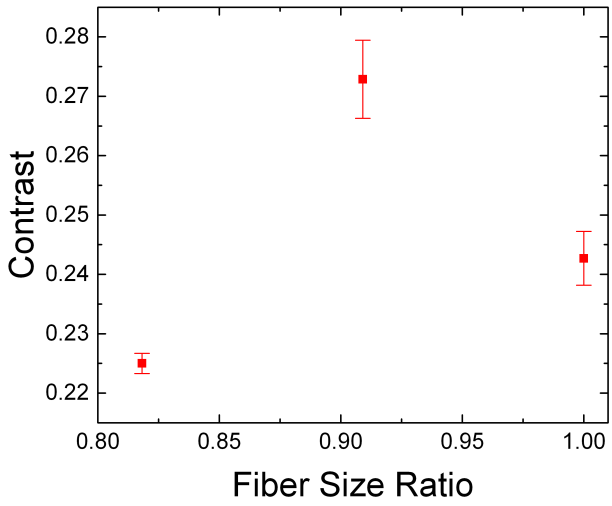

Figure 4.25: Contrast with different iris sizes next to a large fiber port for the beam splitter.

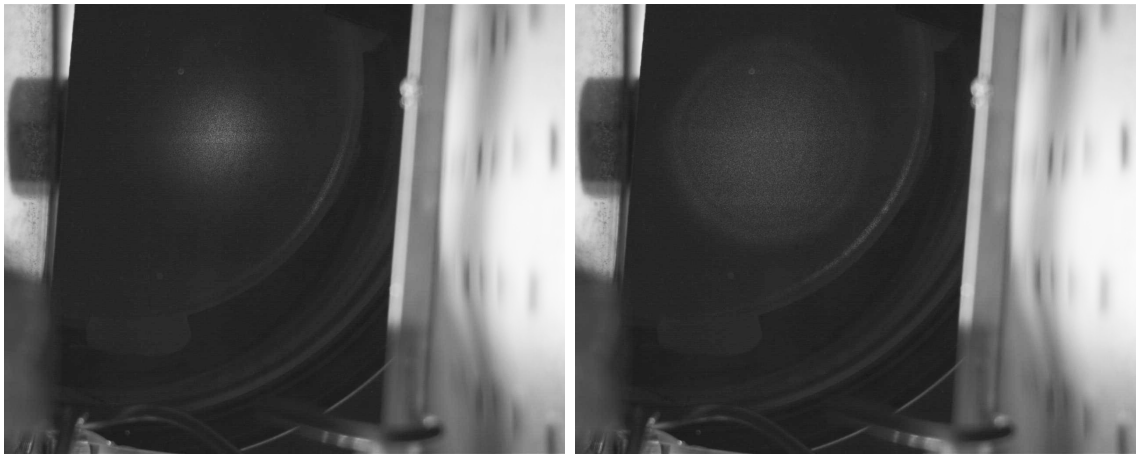

(a) The Bragg diffraction beam profile from a medium sized fiber port.

(b) The Bragg diffraction beam profile from a large sized fiber port.

Figure 4.26: Pictures of Bragg beams from different sized fiber ports. They are taken using a CCD camera at the top of the vacuum chamber. We can see the diffraction rings occurring in the right picture.

This result shows the possibility of the wall-scattered light affecting the overall contrast. In the vacuum chamber, the solenoid tube which has a diameter of 1.5 inches may severely cut the Gaussian beam profile from the large fiber port. The tube determines the maximum beam size we can use in the setup. A long term solution may be to increase the vacuum tube size, but then the homogeneousness of magnetic field will be the next consideration,

since the diameter of the solenoid gets larger.

4.5.5 Bloch oscillations scattering

When we utilizes Bloch oscillations for our atom interferometer, the contrast is better under the blue detuned laser condition, since the single photon scattering rate is higher in the red detuned case and is lower in the blue detuned case. Because the Bloch oscillations pulse is turned on for 900 μs, a low scattering rate is enough to destroy the overall phase without heating atoms. Even though the signal showed on the scope has the same shape, the increasing Bloch oscillation intensity can already diminish the contrast down to zero. The solution will be further detuned lasers to generate Bloch oscillations, since Bloch oscillations do not require as high intensity as Bragg diffraction.

Chapter 5

Conclusion

5.1 Current status

5.1.1 Compton clock

The Compton frequency we measured from the Compton clock is $\omega_0/2\pi = (2993486252 \pm 12) \times 10^{16}$ Hz, which has uncertainly 4.0 ppb, and the largest systematic error is 3.1 ppb for the constant phase shift. The measured value matches CODATA 2010 within 2σ.

5.1.2 Fine structure constant

The value of the fine structure we measured is $\alpha^{-1} = 137.03599872(28)$, with uncertainty 2.0 ppb. The comparison between the new value and old measurements is shown in figure 5.1. The result is about three times better compared with the result from the previous cesium recoil frequency measurement [9]. With the implementation of Bloch oscillations and Raman sideband cooling, the statistical uncertainty has improved from 0.90 ppb to 0.33 ppb in six hours (0.66 ppb in the recoil frequency measurement), which is about two times better than the best recoil frequency measurement [16]. In addition, the original leading systematic error has improved from 1.65 ppb to 0.60 ppb. These promise better fine structure constant measurements in the future.

5.2 Future prospects

5.2.1 Recoil frequency: upcoming improvements

The sensitivity of the recoil frequency measurement is not very close to the shot noise limit. To get better signals, we need to have a more uniform atom ensemble, reduce the contrast loss, suppress the vibration, and have better detection.

Because atom interferometer signals come from individual atoms, any difference in atoms may contribute to larger standard errors. The stability of the velocity distribution of the

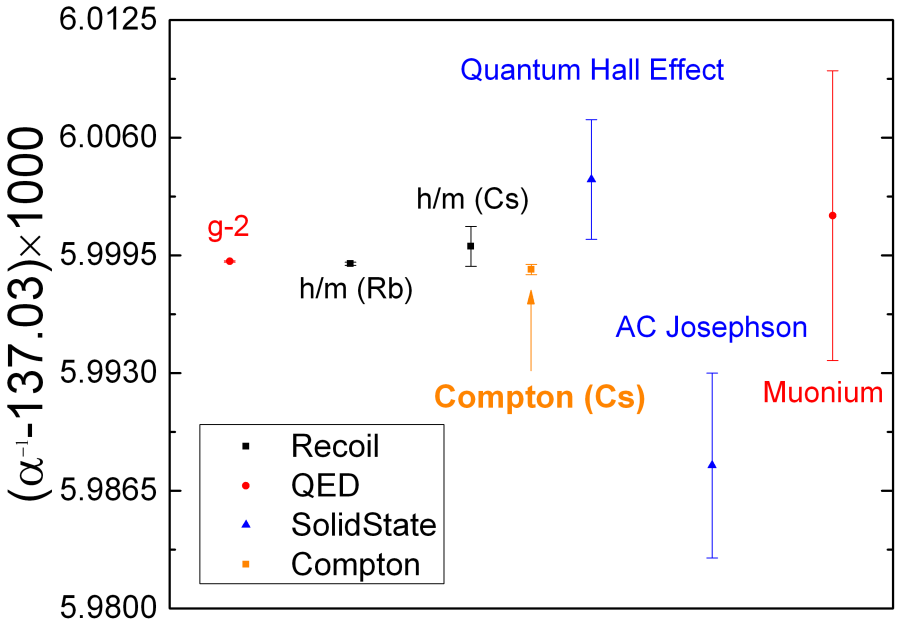

Figure 5.1: Measurements of the fine structure constant with the new measurement from the Compton clock.

atom cloud in each shot can be further improved by intensity stabilization for the MOT system. The spatial distribution of the atoms can be more compressed by different configuration of the MOT system. For preparing atoms with state and velocity selection, phase locking two lasers together for Raman transitions instead of using an EOM can simplify the possible frequency combinations that drive undesired transitions and therefore obtain the atoms with purer states.

The contrast loss is discussed in section 4.5.The most feasible improvement is to use lasers with larger detuning for Bloch oscillations to reduce the scattered light. We can also increase the overall acceleration but reduce the pulse duration [43]. Better intensity stabilization of both frequency components of the beam splitters will also keep the ellipse signal from fluctuating and increase the optimum contrast.

The vibration of the top mirror in Bragg diffraction will affect the k_{eff} and therefore introduce noise. Better vibration isolation will help.

Anti-reflective coating for the detection optical window can reduce the possibility of etaloning and improve the quality of detection. CCD camera may also be useful to extract more information than a PMT [44].

5.2.2 Compton frequency: mass and frequency, new clock

The Compton frequency measurement relates frequency and mass, the two are connected by the Planck constant. In 2011, the General Conference on Weights and Measures (CGPM-2011) considered a revision to the SI units that would assign an exact value to the Planck constant. Under the proposed redefinition, Compton frequency measurements are mass measurements.

In practice, measuring macroscopic and microscopic masses involves different experimental methods and poses different challenges. Microscopic masses m_x can be weighed as

$$m_\mathrm{x} = \frac{m_\mathrm{x}}{\mathrm{u}} \frac{\mathrm{u}}{m_\mathrm{e}} m_\mathrm{e}. \tag{5.1}$$

The ratio m_x/u of the unknown mass and the atomic mass unit u is determined by mass spectroscopy to often better than 0.5 ppb accuracy [45, 46]. The u itself has been related to the electron mass m_e with 0.40 ppb accuracy [13], and m_e is obtained from the Rydberg constant, the defined values of h and c, and the fine structure constant α. This involves both an extremely precisely measured constant of nature and an extremely precise but highly involved calculation. The overall accuracy of this chain of measurements depends on the unknown mass, but will be better than 1 ppb for many atoms.

An alternative path is provided by applying

$$m_\mathrm{x} = \frac{m_\mathrm{x}}{m_\mathrm{At}} \frac{m_\mathrm{At}}{\hbar} \hbar, \tag{5.2}$$

where At is an atomic species for which $\hbar/m_\mathrm{At}$ has been measured (e.g., ^{87}Rb, with a precision of 1.2 ppb [16]). This method is slightly less accurate, but more direct as it requires a measurement of the laser frequency as the only auxiliary measurement.

Under the proposed CGPM-2011 definition, our Compton clock provides an absolute measurement of the cesium atom's mass to an accuracy of 4.0 ppb. While the accuracy is not advanced, the Compton clock offers a transparent connection between the second and a microscopic mass as it is based on simple physical principles and does not requiring auxiliary measurements.

Measuring macroscopic masses under the CGPM-2011 definition poses a different challenge, as the experimental methods that apply to the microscopic world cannot be applied. One successful approach is the Watt balance, which reaches a precision of 33 ppb [47]. The unknown macroscopic mass M is lifted upwards at velocity $\vec{v}$ against the local gravitational acceleration $\vec{g}$. The power $P = M(\vec{g} \cdot \vec{v})$ is measured electrically in terms of the Josephson and the von Klitzing constant. This relates the power, and thereby the mass, to frequency and the defined values of the Planck constant and the speed of light. This method requires several auxiliary measurements, e.g., of velocity $\vec{v}$ and local gravity $\vec{g}$, and involves moving parts whose surface flatness has to be precisely controlled.

The link from the Compton frequency to macroscopic masses is made by crystals of accurately measured volume and lattice constant, and hence particle number, called Avogadro

spheres. In theory, the number of atoms contained in such a crystal is $N_{\mathrm{At}} = 8V/a^3$, where 8 is the number of atoms in the unit cell, V is the crystal's volume, and a is the lattice constant. Since binding energies are negligible at the present accuracy, the Compton frequency of the sphere is $m_{\mathrm{Si}}/m_{\mathrm{Cs}} N_{\mathrm{At}} \omega_0$, given by the measured Compton frequency ω_0. The ratio $m_{\mathrm{Si}}/m_{\mathrm{Cs}}$ is between the effective molar mass of the sphere's material (silicon) and ^{133}Cs. Present data yields the mass of two spheres with an overall accuracy of 30 ppb [48]. This approach yields comparable accuracy of macroscopic masses compared with the Watt balance measurement and offers a different set of systematic effects.

While our clock is based on coherent atomic matter waves, alternative approaches may exist. For example, the rapidly developing field of optomechanics [49] might find means to measure the recoil energy of a nanomechanical mirror scattering photons. This could result in a clock referenced to the mass of a mesoscopic object or a mesoscopic mass standard referenced to the second. The accuracy of such mass standards would then depend upon the precision of the measurement of their Compton frequency, not upon the purity of their constituents. Given that Bragg diffraction of electrons has already been demonstrated [50], a clock using electrons or positrons may be within reach, and would be the first clock based on an elementary particle. A positron or antihydrogen clock would be based entirely on antimatter, and useful for testing CPT symmetry or, e.g., the Einstein equivalence principle for antimatter.

While the accuracy of the Compton clock is modest, the resolution and accuracy of atom interferometry is advancing rapidly [51]. Use of higher laser frequencies (possible without changing the reference particle), lighter particles, and/or longer interrogation times can possibly lead to a Compton clock that can compete with a primary time standard. In the future, it will be useful that one fundamental unit could be defined by a specific particle, and the units of mass, time, and length would be derived from it.

Bibliography

[1] F. Bloch, *Phys. Rev.* **70**, 460 (1946).

[2] A. Peters, K. Y. Chung, and S. Chu, *Metrologia.* **38**, 25 (2001).

[3] M. A. Hohensee *et al.*, *Phys. Rev. Lett.* **106**, 151102 (2011).

[4] G. Lamporesi *et al.*, *Phys. Rev. Lett.* **100**, 050801 (2008).

[5] M. A. Hohensee *et al.*, *Phys. Rev. Lett.* **108**, 230404 (2012).

[6] A. Arvanitaki *et al.*, *Phys. Rev. Lett.* **100**, 120407 (2008).

[7] P. W. Graham *et al.*, *Phys. Rev. Lett.* **110**, 171102 (2013).

[8] B. Canuel *et al.*, *Phys. Rev. Lett.* **97**, 010402 (2006).

[9] A. Wicht *et al.*, *Phys. Scripta* **102**, 82 (2002).

[10] B. Dubetsky and M. A. Kasevichl, *Phys. Rev. A* **74**, 023615 (2006).

[11] S. Gupta *et al.*, *Phys. Rev. Lett.* **89**, 140401 (2002).

[12] R. Charrière *et al.*, *Phys. Rev. A* **85**, 013639 (2012).

[13] P. J. Mohr, B. N. Taylor, and D. B. Newell, *Rev. Mod. Phys.* **84**, 1527 (2012).

[14] D. Hanneke, S. Fogwell, and G. Gabrielse, *Phys. Rev. Lett.* **100**, 120801 (2008).

[15] T. Aoyama *et al.*, *Phys. Rev. Lett.* **109**, 111807 (2012).

[16] R. Bouchendira *et al.*, *Phys. Rev. Lett.* **106**, 080801 (2011).

[17] A.-M. Jeffery *et al.*, *IEEE Trans. Instrum. Meas.* **46**, 264 (1997).

[18] E. R. Williams *et al.*, *IEEE Trans. Instrum. Meas.* **38**, 233 (1989).

[19] F. G. Mariam *et al.*, *Phys. Rev. Lett.* **49**, 993 (1982).

[20] G. Audi, A.H. Wapstra, and C. Thibault, *Nucl. Phys.* A**729**, 337 (2003).

[21] S.-Y. Lan *et al.*, *Science* **339**, 554 (2013).

[22] T. E. Parker, Metrologia, *Metrologia* **1**, 1 (2010).

[23] A. D. Ludlow *et al.*, *Science* **319**, 1805 (2008).

[24] T. Rosenband *et al.*, *Science* **319**, 1808 (2008).

[25] C. W. Chou *et al.*, *Phys. Rev. Lett.* **104**, 070802 (2010).

[26] E. Peik and Chr. Tamm, *Europhys. Lett* **61**, 183 (2003).

[27] C. J. Campbell *et al.*, *Phys. Rev. Lett.* **108**, 120802 (2012).

[28] N. F. Ramsey, *Phys. Rev.* **78**, 695 (1950).

[29] Ch. J. Bordé *et al.*, *Phys. Rev. A* **30**, 1836 (1984).

[30] D. S. Weiss, B. C. Young, and S. Chu, *Appl. Phys.B* **59**, 217 (1994).

[31] P. Storey and C. Cohen-Tannoudji, *J. Phys. II France* **4**, 1999 (1994).

[32] A. Fitzgibbon, M. Pilu, and R. B. Fisher, *IEEE Trans. Pattern Anal. Mach. Intell.* **21**, 476 (1999).

[33] W. Gander, G. H. Golub, and R. Strebel, *BIT Numer. Math.* **34**, 558 (1994).

[34] J. K. Stockton, X. Wu, and M. A. Kasevich, *Phys. Rev. A* **76**, 033613 (2007).

[35] H. Müller, S.-W. Chiow, and S. Chu, *Phys. Rev. A* **77**, 023609 (2008).

[36] S.-Y. Lan *et al.*, *Phys. Rev. Lett.* **108**, 090402 (2012).

[37] K. E. Gibble, S. Kasapi, and S. Chu, *Opt. Lett.* **17**, 526 (1992).

[38] H. J. Metcalf and P. van der Straten, *Laser Cooling and Trapping* (Graduate Texts in Contemporary Physics, New York, 2001).

[39] P. Treutlein, K. Y. Chung, and S. Chu, *Phys. Rev. A.* **63**, 051401 (2001).

[40] G. Camy, Ch. J. Bordé, and M. Ducloy, *Opt. Commun.* **41**, 325 (1982).

[41] J. H. Shirley, *Opt. Lett.* **7**, 537 (1982).

[42] M. J. Snadden *et al.*, *Phys. Rev. Lett.* **81**, 971 (1998).

[43] M. Andia *et al.*, *Phys. Rev. A* **88**, 031605(R) (2013).

[44] S. M. Dickerson *et al.*, *Phys. Rev. Lett.* **111**, 083001 (2013).

[45] M. P. Bradley *et al.*, *Phys. Rev. Lett.* **83**, 4510 (1999).

[46] M. P. Bradley *et al.*, *Phys. Rev. A* **82**, 042513 (2010).

[47] I. A. Robinson and B. P. Kibble, *Metrologica* **44**, 427 (2007).

[48] B. Andreas *et al.*, *Phys. Rev. Lett.* **106**, 030801 (2011).

[49] T. J. Kippenberg and K. J. Vahala, *Science* **321**, 1172 (2008).

[50] D. L. Freimund and H. Batelaan, *Phys. Rev. Lett.* **89** , 283602 (2002).

[51] S. Dimopoulos *et al.*, *Phys. Rev. Lett.* **98**, 111102 (2007).